

**Czech Technical University in Prague
Faculty of Nuclear Sciences and Physical
Engineering**

**Department of Physics
Experimental Nuclear and Particle Physics**



**Study of Properties of the Dipole
Scattering Amplitude Using
Balitsky-Kovchegov Evolution
Equation**

DIPLOMA THESIS

Author: Marek Matas
Supervisor: Ing. Jan Čepila, Ph.D.
Year: 2016

Prohlášení

Prohlašuji, že jsem svou diplomovou práci vypracoval samostatně a použil jsem pouze podklady (literaturu, projekty, SW atd...) uvedené v příloženém seznamu.

Nemám závažný důvod proti použití tohoto školního díla ve smyslu § 60 Zákona č. 121/2000 Sb. o právu autorském, o právech souvisejících s právem autorským a o změně některých zákonů (autorský zákon).

V Praze dne

.....
podpis

Acknowledgement

I would like to thank Ing. Jan Čepila, Ph.D. for his extended help with supervising my thesis and for his skill and patience with helping a newcomer to grasp the complex ideas of QCD and physics in general. I would also like to thank Jesús Guillermo Contreras Nuño for helping me with difficult topics of this thesis and for filling my spirit with enthusiasm and curiosity for particle physics and science in general.

Marek Matas

Author: Marek Matas
Type of work: Diploma thesis
Supervisor: Ing. Jan Čepila, Ph.D.
FJFI, CTU

Title:

Study of Properties of the Dipole Scattering Amplitude Using Balitsky-Kovchegov Evolution Equation

Author: Marek Matas

Abstract: It has been known for a long time that hadron structure functions show a large increase in the number of gluons in the region of small Bjorken- x . The steep rise of the number of gluons in the hadron at a fix scale is described by the BFKL evolution equation. However, experimental data suggest less gluons in a hadron than there should be according to the solution of the leading-log BFKL equation. This can be taken as the evidence of a phenomenon called parton saturation. Accordingly, the number of gluons in a hadron is given by the dynamical balance between radiation and recombination processes, which can lead to the suppression of the number of gluons. These recombination effects in the hadron are described by the Balitsky-Kovchegov equation(BK), a 2D integro-differential equation with divergent kernel. The solution of the BK equation provides the dipole scattering amplitude that incorporates the effects mentioned above and that can be used to predict the cross-sections for a wide range of processes. Since there is no analytic method to solve the equation, one has to do it numerically and so the study of the properties of the numerical solution is of great importance.

Key words: Deep Inelastic Scattering, Balitsky-Kovchegov equation, HERA

Název práce:

Studium saturačních efektů v hadronech s použitím Balitski-Kovchegovy evoluční rovnice

Autor: Marek Matas

Abstrakt: Je známo, že hadronové strukturní funkce vykazují prudký nárůst počtu gluonů v oblasti malých Bjorkenových x . Prudký nárůst počtu gluonů je důsledkem BFKL evoluční rovnice. Ovšem experimentální data ukazují menší počet gluonů, než předpovídá BFKL evoluční rovnice. Toto může být bráno jako důkaz přítomnosti jevu saturace partonů. Zde je počet gluonů v hadronu dán dynamickou rovnováhou mezi radiačními a rekombinačními procesy, které vedou ke snížení počtu gluonů. Tyto rekombinační procesy v hadronech jsou popsány Balitsky-Kovchegovou evoluční rovnicí (BK), což je dvoudimenzionální integro-diferenciální rovnice s divergentním jádrem. Řešení této rovnice poskytuje dipólovou rozptylovou amplitudu, která zahrnuje jevy popsané výše a může být použita k předpovězení účinného průřezu pro širokou škálu procesů. Protože neexistuje analytické řešení této rovnice, musí se řešit numericky a studium vlastností tohoto numerického řešení je velmi důležité.

Klíčová slova: Hluboce nepružný rozptyl, Balitsky-Kovchegovova rovnice, HERA

Contents

Introduction	7
1 High energy collision phenomenology	10
1.1 Deep Inelastic Scattering	10
1.1.1 Lorentz-invariant variables	11
1.1.2 DIS in Bjorken limit	11
1.1.3 Color dipole approach to DIS	13
1.2 Evolution equations of parton densities	15
1.2.1 The DGLAP equations	17
1.2.2 The BFKL evolution equation	17
1.3 Color Glass Condensate and saturation	18
1.3.1 The JIMWLK equations	20
1.3.2 Balitsky-Kovchegov evolution equation	21
2 Numerical methods	25
2.1 Runge-Kutta method	25
2.1.1 First order - Euler Method	26
2.1.2 Second order - Ralston method	27
2.1.3 Fourth order	27
2.2 Simpson method	29
2.3 Lagrange interpolation	30
3 Solving the rcBK equation	31
3.1 Impact parameter independent rcBK equation	31
3.2 Geometric Scaling	32
3.3 Impact parameter dependent rcBK equation	36

4	Results	41
4.1	The Optimal Setup	41
4.2	rcBK solutions without impact parameter dependence	42
4.3	Geometric scaled solutions	46
4.4	Impact parameter dependent rcBK solutions	55
	Conclusion	64
A	Runge-Kutta method for the impact parameter dependent rcBK equation derivation	67
B	Simplified Runge Kutta method for the BK equation	69

Introduction

Great attention in the previous decade was given to studying the properties of particles at the high-energy limit of QCD. Deep Inelastic Scattering (DIS) studied at the HERA collider was a good tool for measuring such properties. Evolution equations such as BFKL [1–5], BK [6–10], JMWLK [11–15] and DGLAP [16–18] are used to describe the properties of particles that take part in high energy collisions. The BFKL evolution equation predicts the emergence of new partons as the energy of the collision increases. In this approach, at leading logarithmic (LL) accuracy the gluon density is not bound by unitarity restrictions.

In the experiments at large accelerators such as HERA or LHC, it was shown that the number of partons does not completely satisfy this equation and that there are less partons than predicted. Measured cross sections predicted by these evolution equations grow above the experimentally obtained values at high energies, where the largest contribution to the cross section is due to newly created gluons. The fact that predictions from LL-BFKL equation overshoot experimental data may be due to recombination processes inside the hadrons and it is included in the BK evolution equation. Recombination processes take place when it is not anymore energetically favorable for a new parton to emerge in the hadron and its entire phase space is already populated.

The BK evolution equation is an integro-differential equation and there are several ways to solve it numerically [19–22]. The BK evolution equation considered in this work includes running coupling kernel that takes into account the two loop processes and assumes both impact parameter dependent and independent solutions.

Using numerical methods such as the Runge-Kutta method of fourth order and Simpson's rule, one can obtain predictions for the structure functions and reduced cross sections of DIS that include recombination processes within the hadron. Numerical methods used to compute these values need to be studied and an optimal setup regarding the precision and speed of computation has to be tested [23].

The solution of the BK equation depends on the considered initial condition. Currently used initial conditions require several parameters that need to be fitted from data in order to obtain valid predictions for observable quantities. It is desirable to come up with an initial condition that would require less parameters and would correspond to the physical nature of this equation. Geometric scaling [24–27] is a phenomenon that might be used for acquiring such an initial condition. This approach generalizes the evolution of the solution towards higher rapidities and allows us to reverse this evolution back to the starting rapidities and corresponding Bjorken-

x. The properties of this acquired initial condition require only a single parameter that needs to be fitted from data and is obtained solely from the properties of the integro-differential equation itself. However in this approach, the measured structure functions cannot be described in as straightforward way as it was with the original initial condition. The change of the evolution behavior when this initial condition is introduced needs to be studied in order to answer the question of validity of this approach and to determine the new set of computation parameters such as σ_0 .

The b-dependent BK equation requires a more sophisticated approach in both implementing the numerical methods to solve it as well as interpreting the obtained results [28–30]. Introducing the impact parameter to the computation increases the dimension of the computation matrix by two (absolute value of the impact parameter and the angle between this vector and dipole distance vector), which increases the computation time from minutes in the non b-dependent case up to weeks for a full computation for all impact parameter vector possibilities. The properties of the solution itself differs significantly from the one obtained without the impact parameter dependence. In this approach, dipoles with large dipole distance exhibit a significant decrease in the scattering amplitude in contrary to the b-independent solution. This effect takes into account that dipoles much larger than the hadron they are interacting with have smaller probability to do so. The solutions of this equation have been studied and compared to the b-independent results.

Results obtained by solving this equation can be used in describing and understanding processes that occur in heavy-ion physics, especially on experiments such as LHC or RHIC.

In this work, we first manage to reproduce the results obtained by other theoretical groups both for the impact parameter independent equation [21] as well as for the solutions that include the impact parameter dependence [29,30]. Since these numerical computations are typically CPU-time demanding, we then focused on the optimization of the numerical method. We managed to reduce the running time by more than one order of magnitude after implementing the optimized computation [23]. Then we established an analysis to find and test a new initial condition that would be given by the intrinsic properties of the rcBK equation. The properties of this scaled initial condition proved to be of a different nature than those of the originally considered MV initial condition. We tested those properties and then established the optimal way of obtaining such initial condition. The scaled initial condition was then used to predict values of the structure function in regions where it differs from the MV initial condition. We then focused on the impact parameter dependent rcBK equation for which the finding of a scaled initial condition is strongly restricted by its CPU-time demands. We managed to develop a new numerical solving method for this equation that enables us to reduce the computation time down to a few hours of running time. These methods enable us to improve and test new initial conditions and other properties of such evolution equation which can lead to reducing the number of free parameters in this approach and better describing the physical processes of deep inelastic scattering.

My personal contribution to the results presented in this thesis is the following:

1. Implementation of the Runge-Kutta method of order one, two and four to solve the rcBK evolution equation.
 - (a) The method of order two has already been used in [21], and I have used those results to cross check my implementation.
 - (b) The method of order four has been introduced in [22], and I have used those results to cross check my implementation
2. I have searched for the best parameters of the numerical setup to balance the speed of execution with the accuracy of the numerical results. These results are new; they are presented in Section 4.1 and have been reported in [23].
3. I have explored the use of initial conditions obtained from solutions of the rcBK equations at large rapidities using geometric scaling. These results are new. They are discussed in Section 4.3 and are intended for publication in the near future.
4. I have used the same methods to solve the impact parameter dependent BK equation. This equation has been solved before using a different numerical method [24, 29], and I have used those results to cross check my implementation. These results are presented in Section 4.4.

Chapter 1

High energy collision phenomenology

1.1 Deep Inelastic Scattering

Deep Inelastic Scattering (DIS) is one of the important tools that allow us to verify physical theories. It is a highly energetic scattering of a lepton off a hadron, where many new particles are created upon the collision and the original hadron falls apart. Such collision can be simplified as shown in Fig. 1.1.

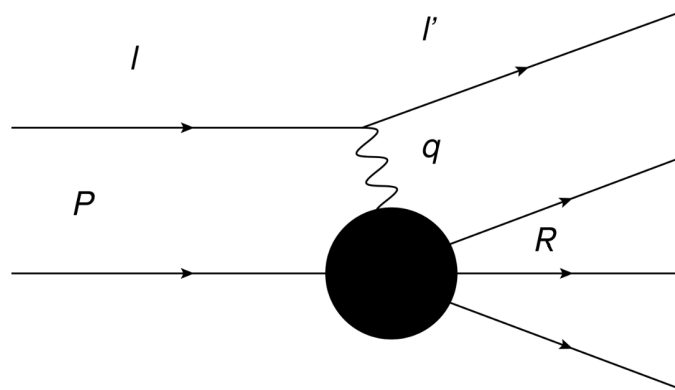


Figure 1.1: Deep inelastic scattering [31].

Relation 1.1. describes such scattering where L is an incoming lepton with four-momentum l , N is a hadron with four-momentum P , L' is the outgoing lepton with four-momentum l' and X represents particles created by the interaction with four-momentum fraction R .

$$L(l) + N(P) \rightarrow L'(l') + X(R) \quad (1.1)$$

1.1.1 Lorentz-invariant variables

To describe this process we need to define Lorentz-invariant variables as shown in Eq. 1.2, 1.3, 1.4 and 1.5. In Eq. 1.2, s is the total energy of the collision in the center-of-mass (CMS) frame, Q^2 is the so called scale of the virtual photon, q^2 is squared four-momentum passed from the lepton to the hadron, ν is the total energy that is passed from the lepton to the target in the target's rest frame and x is the so called Bjorken x that (in the infinite momentum frame) gives us the ratio of the momentum carried by the scattered gluon or quark to the total momentum carried by the target.

$$s = (P + l)^2 \quad (1.2)$$

$$q^2 = -Q^2 = (l - l')^2 \quad (1.3)$$

$$\nu = \frac{P \cdot q}{m_p} = \frac{W^2 - Q^2 - m_p^2}{2m_p} \quad (1.4)$$

$$x = \frac{Q^2}{2P \cdot q} = \frac{Q^2}{Q^2 + W^2 - m_p^2} \quad (1.5)$$

Here m_p is the mass of the proton. We shall also define the variable W^2 , which gives us the total energy that is given to the hadron in the CMS frame as shown in Eq. 1.6

$$W^2 = (P + q)^2 \quad (1.6)$$

$$y = \frac{P \cdot q}{P \cdot l} = \frac{Q^2}{x(s - m_p^2)} \quad (1.7)$$

and equation 1.7 represents the transferred energy fraction from the lepton onto the hadron. The scale Q^2 defines the resolution of the scattering process, since the incoming particle can interact with objects with size proportional to $1/Q^2$. By increasing the energy, we are able to see softer gluons (with smaller fraction of momenta) that are emitted by more energetic gluons.

1.1.2 DIS in Bjorken limit

The emission of a photon from a lepton is an understood process and is well described by Quantum Field Theory. A point-like lepton serves as a source of the virtual photon that will then interact with the hadron. Scattering of the virtual photon off the hadron results in breaking the hadron and creating other particles. In this model, we are working in the infinite momentum frame which supposes very high momentum of the scattered proton.

If we consider the high energy limit and keep Q^2 fixed, the Bjorken x decreases since $s \sim Q^2/x$. Therefore, the observed objects carry lower and lower fraction of

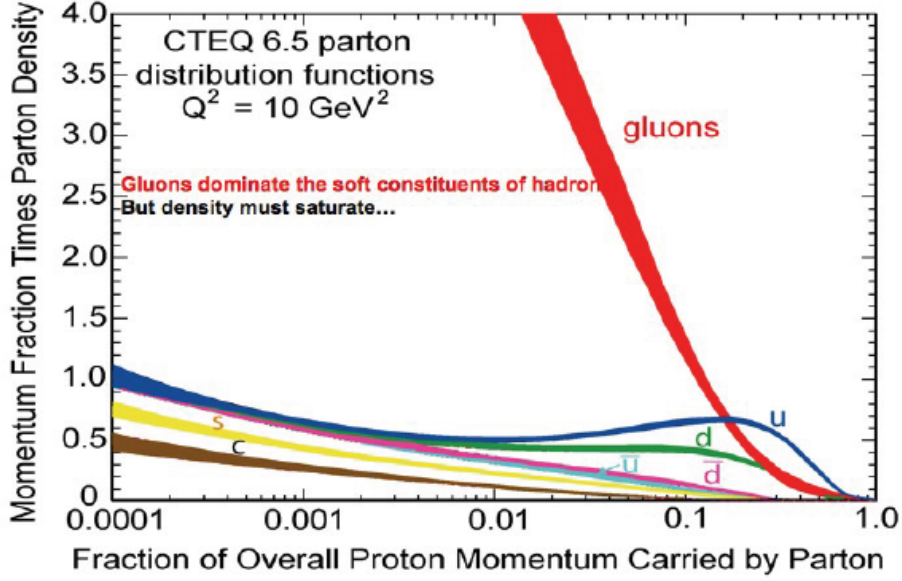


Figure 1.2: Distribution of parton density for different constituents of a proton [32].

the total momentum. In the high energy region, the proton is mostly populated by gluons (which is explained more further in the thesis) [1–3] and therefore we will neglect the effects of quarks as shown in Fig. 1.2. In this figure we can see how the parton density distribution evolves for different partons with respect to Bjorken x . We can see that below $x \sim 10^{-1}$ the gluon density is larger than the density of other partons and their density keeps on growing above all boundaries. The growth of the gluon density can be tamed by the introduction of saturation.

The differential cross section depends on the energy and scale of the process. Equation 1.8 shows such dependence, where $F_1(x, Q^2)$ and $F_2(x, Q^2)$ are the structure functions of proton, α represents the electromagnetic coupling, y is the inelasticity, x is the Bjorken x and Q^2 is the scale of the virtual photon.

$$\begin{aligned} \frac{d^2\sigma}{dx dQ^2} &= \frac{4\pi\alpha^2}{xQ^4} ((1-y)F_2 + y^2 x F_1) \\ &= \frac{4\pi\alpha^2}{xQ^4} \left(\left(1 - y + \frac{y^2}{2}\right) F_2 - \frac{y^2}{2} F_L \right) \end{aligned} \quad (1.8)$$

because Callan-Gross relation holds

$$F_L = F_2 - 2xF_1 \quad (1.9)$$

where F_L is called the longitudinal structure function.

For the structure functions $F_L(x, Q^2)$ and $F_2(x, Q^2)$ stands [33]

$$F_2 = \frac{Q^2(1-x)}{4\pi^2\alpha} \frac{Q^2}{Q^2 + 4m_p^2 x^2} \sigma_{tot}^{\gamma^*p} \quad (1.10)$$

$$F_L = \frac{Q^2(1-x)}{4\pi^2\alpha}\sigma_L \quad (1.11)$$

which with the approximation of $x \rightarrow 0$ changes into [34]

$$F_2 = \frac{Q^2(1-x)}{4\pi^2\alpha}(\sigma_T + \sigma_L) \quad (1.12)$$

$$F_L = \frac{Q^2}{4\pi^2\alpha}\sigma_L \quad (1.13)$$

since for $\sigma_{tot}^{\gamma^*p}$ stands

$$\sigma_{tot}^{\gamma^*p} = \sigma_T + \sigma_L \quad (1.14)$$

where σ_T and σ_L are the cross sections for absorption of longitudinally and transversally polarized photons and m_p is the mass of a proton.

The structure function $F_2(x, Q^2)$ can be also expressed using the naive parton model as

$$F_2(x, Q^2) = x \sum_i e_{q_i}^2 (q_i(x, Q^2) + \bar{q}_i(x, Q^2)) \quad (1.15)$$

where q_i is the quark density, \bar{q}_i the antiquark density, e_{q_i} is the charge of the quark divided by the unit charge and the sum runs over all quark flavors. At the next order in perturbation, the structure function depends also on the gluon density.

1.1.3 Color dipole approach to DIS

So far we have shown how the inner composition of proton changes with respect to energy and scale of the incoming photon.

If we consider the target rest frame, the lepton - hadron collision is as follows. First, the incoming lepton emits a virtual photon. This photon then spontaneously fluctuates into a quark - antiquark color dipole (analog to the dipole in electrodynamics). This dipole then interacts strongly with the target proton and its further fluctuation back into a photon is disrupted. This approach is called the Color dipole model [35–40]. The fluctuation of a photon into the color dipole is necessary because of new particles that emerge from the collision, which is only possible when strong interaction is present and could not be described by mere electromagnetic interaction.

At small x , it can be shown that the lifetime of such quark - antiquark fluctuation is greater than the average time of the whole interaction [31], which is important because then the dipole has enough time to react with the target hadron before it annihilates. The cross section of the total photon-proton scattering is shown in 1.16,

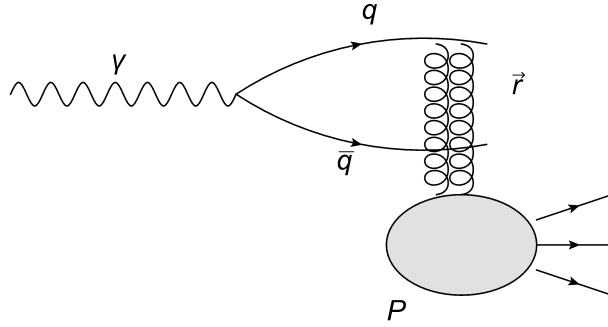


Figure 1.3: Color dipole fluctuating from the virtual photon [41].

where $|\Psi_{T,L}^i|^2$ is the wave function of the photon that fluctuates to create a color dipole. Indexes T and L correspond to transverse and longitudinal polarizations of the incident photon and e_{q_i} , m_{q_i} and z correspond to fractional electric charge of quark q_i , its mass and fraction of the longitudinal momentum of photon it carries.

$$\sigma_{T,L}^{\gamma^* \rightarrow h}(x, Q^2) = \sum_i \int d\vec{r} dz |\Psi_{T,L}^i(z, \vec{r})|^2 \sigma^{q\bar{q}}(\vec{r}, x) \quad (1.16)$$

The final cross section is then computed by integrating the photon-color dipole wavefunction and the cross section of the quark-antiquark dipole scattering of the proton target over all transverse dipole sizes \vec{r} and over all possible values of photon's fractional momentum z [21].

Using the dipole cross-section $\sigma^{q\bar{q}}(r, x)$ we can compute the structure function F_2 as shown in Eq. 1.17 and this can then be measured experimentally.

$$F_2(x, Q^2) = \frac{Q^2}{4\pi^2\alpha_{em}} \int \sum_i d\vec{r} dz |\Psi_{T,L}^i(z, \vec{r})|^2 \sigma^{q\bar{q}}(\vec{r}, \tilde{x}), \quad (1.17)$$

[22] where $|\Psi_{T,L}^i(z, \vec{r})|^2$ is a sum of squared longitudinal and transversal photon wave functions as shown in Eq. 1.19 and \tilde{x} is introduced due to photoproduction limit as shown in Eq. 1.18 [42].

$$\tilde{x} = x \left(1 + \frac{4m_{q_i}^2}{Q^2} \right), \quad (1.18)$$

where the mass of the incident quark is set to the value of 140 MeV^2 for u,d and s quarks. For charm quark, the mass is set to 1.27 GeV^2 and 4.2 GeV^2 for the beauty quark [43].

$$|\Psi_{T,L}^i(z, \vec{r})|^2 = |\Psi_T^i(z, \vec{r})|^2 + |\Psi_L^i(z, \vec{r})|^2 \quad (1.19)$$

and the longitudinal and transversal photon wave functions are given by

$$|\Psi_T^i(z, \vec{r}, Q^2)|^2 = \frac{3\alpha_{em}}{2\pi^2} e_{q_i}^2 ((z^2 + (1-z)^2)\epsilon^2 K_1^2(\epsilon r) + m_{q_i}^2 K_0^2(\epsilon r)) \quad (1.20)$$

$$|\Psi_L^i(z, \vec{r}, Q^2)|^2 = \frac{3\alpha_{em}}{2\pi^2} e_{q_i}^2 (4Q^2 z^2 (1-z)^2 K_0^2(\epsilon r)) \quad (1.21)$$

where z is the fraction of the total momentum carried by the quark, K_0 and K_1 are the MacDonald functions and

$$\epsilon^2 = z(1-z)Q^2 + m_{q_i}^2, \quad (1.22)$$

where m_{q_i} is the mass of the considered quark.

The reduced cross-section is obtained from relation [21]

$$\sigma_r(x, y, Q^2) = F_2(x, Q^2) - \frac{y^2}{1 + (1-y)^2} F_L(x, Q^2), \quad (1.23)$$

where inelasticity y is obtained from $y = Q^2/sx$ and \sqrt{s} is the CMS collision energy.

The actual dipole scattering cross section is then computed by integrating the dipole-proton scattering amplitude over the impact parameter as shown in Eq. 1.24.

$$\sigma^{q\bar{q}}(r, x) = 2 \int d\vec{b} N(x, r, \vec{b}) \quad (1.24)$$

This dipole cross section then covers all the QCD effects and can be also obtained from the BK evolution equation. If we neglect the dependence of the scattering amplitude N on the impact parameter, the integral over it can be simplified into expression 1.25. [44],

$$\sigma^{q\bar{q}}(r, x) = \sigma_0 N(x, r) \quad (1.25)$$

where σ_0 is a parameter that we fit from data.

The assumption of independence of the scattering amplitude N on the impact parameter corresponds to approximating the target with finitely big homogeneous hadron where the size of this hadron is fitted to experimentally measured data. The scattering amplitude reaches values between 1 and 0. For a fixed r , as the Bjorken x decreases (energy increases) the number of gluons grows and the scattering amplitude approaches 1 since it is very probable for the dipole to interact with this dense hadron. Its value also increases towards one with the increase of dipole distance r . With the limit $r \rightarrow 0$, we get $N \rightarrow 0$ due to the color transparency.

1.2 Evolution equations of parton densities

During the interaction, color dipole exchanges a particle with the target hadron. To maintain the color conservation, the exchanged particle must be colorless and in the

first approximation we consider it to be a pair of gluons. The actual complex particle that is exchanged is called Pomeron. A linear approach to the interaction such as the one used in BFKL evolution equation suggests only one particle exchange between the color dipole and target hadron whereas non-linear evolution equations such as the BK equations suggest multiple pomeron exchanges as shown in Fig. 1.4.

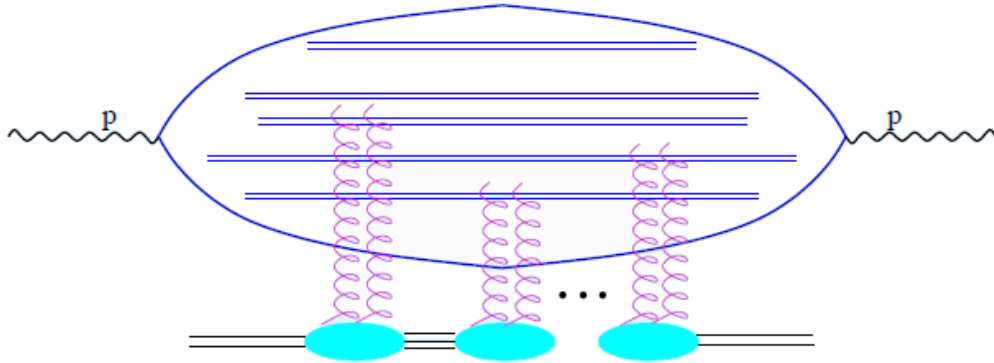


Figure 1.4: Multiple pomeron exchange between the color dipole and the target hadron [45].

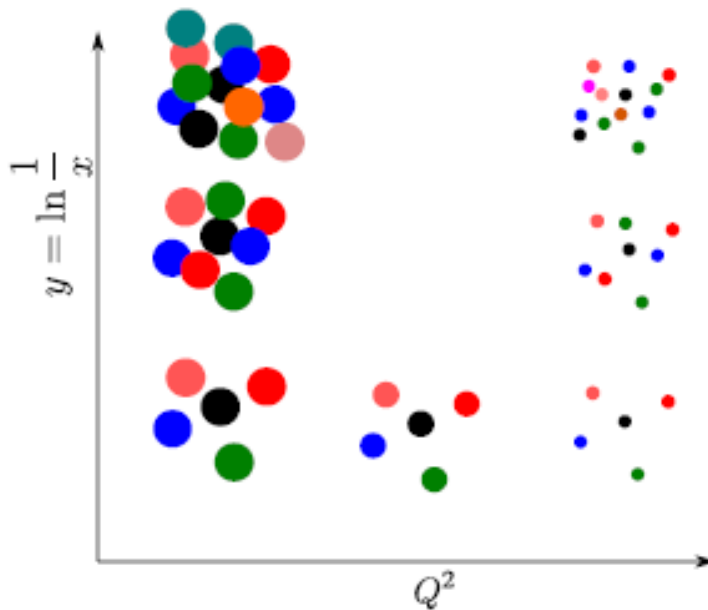


Figure 1.5: Gluon number and size with respect to rapidity and scale [31].

If we fix the scale of the virtual photon and increase the energy of the collision, we observe that some gluons start to overlap due to fixed dimensions of the proton itself. In this case we have to take into account the recombination processes that take place among gluons as they become more influential. The scale when gluons start to overlap is called saturation scale and occurs when most of the phase space in the proton

is already occupied by other gluons. Further decreasing of Bjorken x will then not result into further gluon number rise since the whole system is already saturated and the new gluons are compensated with the recombination processes and a dynamical balance is established. This situation varies for different scales as with higher Q^2 , we decrease the dimensions of the gluons themselves. We can determine a so called saturation scale Q_s at which this effect takes place with respect to the total energy. These non-linear recombination processes are described by the Balitsky-Kovchegov evolution equation (BK).

1.2.1 The DGLAP equations

The DGLAP (Dokshitzer-Gribov-Lipatov-Altarelli-Parisi) equations are used in interactions, where Q^2 is large and x is not too small [33]. They describe the change of the parton size when higher scales are introduced. The equations themselves, at leading-log, stand as

$$\frac{dg(x, Q^2)}{d\ln Q^2} = \frac{\alpha_s}{2\pi} \int_x^1 \frac{dz}{z} \left(\sum_i q_i(z, Q^2) P_{gq} \left(\frac{x}{z} \right) + g(x, Q^2) P_{gg} \left(\frac{x}{z} \right) \right) \quad (1.26)$$

and

$$\frac{dq_i(x, Q^2)}{d\ln Q^2} = \frac{\alpha_s}{2\pi} \int_x^1 \frac{dz}{z} \left(q_i(z, Q^2) P_{qq} \left(\frac{x}{z} \right) + g(x, Q^2) P_{qg} \left(\frac{x}{z} \right) \right) \quad (1.27)$$

where q_i is the quark density for the flavor i and g is the gluon density. $P_{ij}(a)$ are the Altarelli-Parisi splitting functions given by terms

$$\begin{aligned} P_{qq}(a) &= \frac{4}{3} \frac{1+a^2}{1-a} = P_{gq}(1-a) \\ P_{gq}(a) &= \frac{4}{3} \frac{1+(1-a)^2}{a} = P_{qq}(1-a) \\ P_{qg}(a) &= \frac{1}{2} (a^2 + (1-a)^2) = P_{gg}(1-a) \\ P_{gg}(a) &= 6 \left(\frac{a}{1-a} + \frac{1-a}{a} + a(1-a) \right) = P_{gg}(1-a) \end{aligned} \quad (1.28)$$

x is the Bjorken x , α_s is the strong coupling constant and Q^2 is the scale of the virtual photon. These equations tell us how the structure functions change when a different scale is introduced.

1.2.2 The BFKL evolution equation

The BFKL (Balitsky-Fadin-Kuraev-Lipatov) evolution equation is valid in the region where Q^2 is finite and x is low [33, 46–48], namely [33]

$$\alpha_s(Q^2) \ln \frac{Q^2}{Q_0^2} \ll \alpha_s(Q^2) \ln \frac{1}{x} < 1 \quad (1.29)$$

In the BFKL equation, the unintegrated gluon density $f(x, k_T^2)$ is used and from that we can obtain the actual gluon density by using the formula

$$xg(x, Q^2) = \int_0^{Q^2} \frac{d\vec{k}_T}{k_T^2} f(x, k_T^2). \quad (1.30)$$

Note that \vec{k}_T is the transverse momentum of the emitted gluon. The BFKL equation then stands as [33]

$$\frac{\partial f(x, k_T^2)}{\partial \ln(1/x)} = \frac{3\alpha_s}{\pi} k_T^2 \int_0^\infty \frac{dk_T'^2}{k_T'^2} \left(\frac{f(x, k_T'^2) - f(x, k_T^2)}{|k_T'^2 - k_T^2|} + \frac{f(x, k_T'^2)}{\sqrt{4k_T'^4 + k_T^4}} \right). \quad (1.31)$$

As the color dipole is accelerated, one of the quarks in the quark-antiquark dipole can also emit gluons as shown in Fig. 1.6. These gluons can then emit other gluons and some of these may then fluctuate into other quark-antiquark dipoles within the original dipole created by the virtual photon. These dipoles do not interact with each other and many are created within the original dipole, creating a complicated structure.

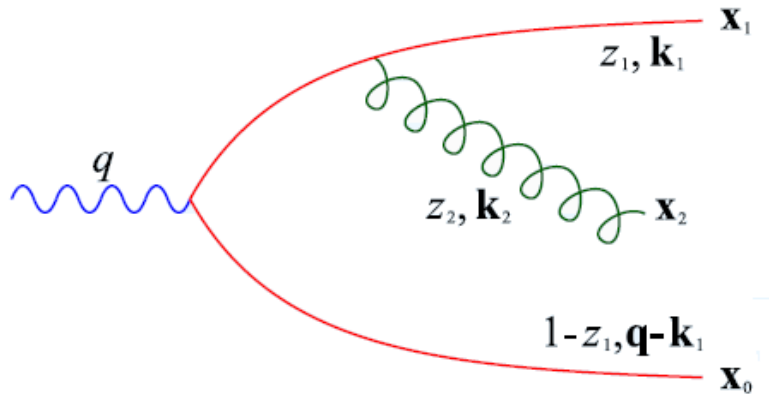


Figure 1.6: Color dipole that emits another gluon [45].

1.3 Color Glass Condensate and saturation

Color Glass Condensate (CGC) [49–52] describes a high energy limit state of nuclei. It is a very densely packed state filled with interacting gluons. This state is the starting state in nucleus collisions that are schematically shown in Fig. 1.7.

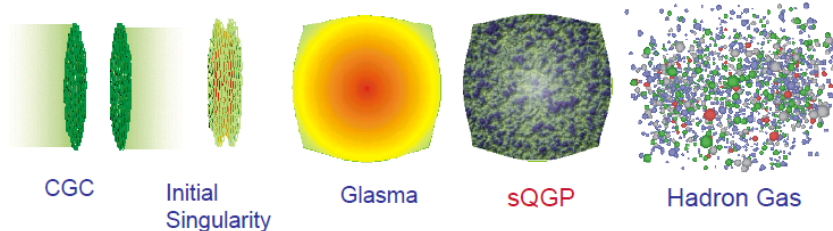


Figure 1.7: Different phases in nuclei collision [32].

In this picture we see on the left side two nuclei in their CGC state just before the collision. At the exact time of collision, initial singularity is formed from which all the following states will emerge (this state differs from an actual geometric singularity). First, Glasma is formed, which is a short-living precursor the Quark Gluon Plasma (QGP). Its name is derived from the very hot and dense amorphous packing of gluons somewhat similar to the structure of metallic glasses and other amorphous structures. After a short period of time, Quark Gluon Plasma is formed that later evolves into the free hadron gas.

In the low energetic limit, collisions and new particle creation is dominated by the quarks, quark antiquark pairs and a few gluons. As $x \rightarrow 0$, gluons dominate the collision and they are responsible for the creation of most of the new particles.

Since at low Bjorken x there is high density of small gluons, strong self interactions occur. Due to the very dense packing and asymptotic freedom of QCD, the interaction between gluons will be weak for the individual gluons but can prove to be strong in general due to its coherent properties. The whole proton will be filled with gluons when the gluon density will be in order of $\frac{1}{\alpha_s}$ that is when it will not be anymore energetically favorable for new gluons to be added to the system. If we try to add new gluons, first the soft gluons with low energy and big dimensions will fill the entire phase space of the proton so that it is not favorable for new gluons to emerge. Then only more energetic gluons that have a smaller dimensions can be added to the system. Note that we are considering only dimensions connected with the transverse momentum plane and therefore corresponding with the transverse momentum distribution.

It means that with a fixed energy of a proton, its volume is filled with gluons of dimensions that correspond to energy and if we wanted to add more gluons to the system, we would have to increase the energy since only gluons with higher p_T are energetically favorable to be added to the system. For every Bjorken x of the hadron, there is a certain saturation transverse momentum and below that momentum the whole phase space is saturated. This is schematically shown in Fig. 1.8.

That is why this structure is called a Color Glass Condensate. Color, because it is composed of particles with a color charge, Glass because it evolves slowly compared to its environment and Condensate because all the phase space of such CGC is filled with gluons until the saturation scale is reached. The whole hadron is Lorentz contracted due to its high momentum and the distribution of the color fields within

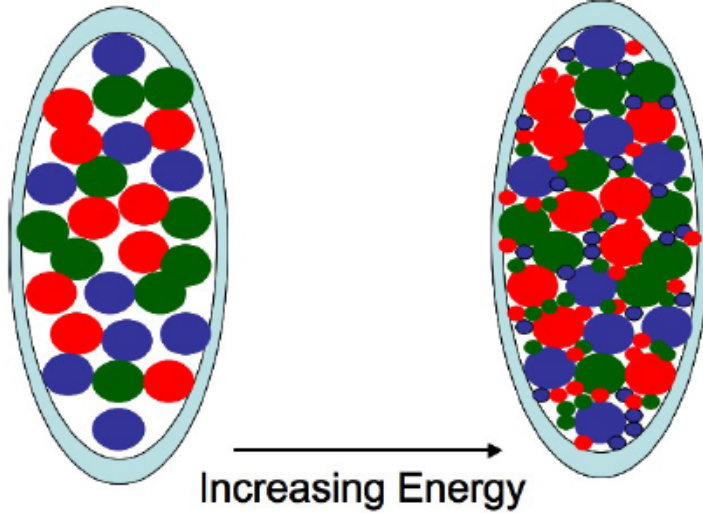


Figure 1.8: Saturation of proton by new high energetic (small) gluons [32].

it is randomly polarized with random color. The gluon fields inside CGC correspond to low x (high energy) and its sources correspond to high Bjorken x [32].

The CGC model is proven to describe well high energetic hadrons with x corresponding to 10^{-2} . Without the introduction of saturation to the QCD models, the cross section of gluon interaction diverges as x decreases at a rate of $\frac{1}{p_T^4}$.

1.3.1 The JIMWLK equations

The set of JIMWLK evolution equations [53–59] is a more general expression that with approximation of large N_c limit reduces to the BK evolution equation. However, when the computation is made and compared with the approximated BK evolution equation, we get only about 0.01 difference between the two results, which is much less than the values expected [60]. The JIMWLK equations are not integro-differential equations such as BK but a set of functional differential equations given by following expressions.

$$\frac{\partial W_Y[\alpha]}{\partial Y} = HW_Y[\alpha] \quad (1.32)$$

$W_Y[\alpha]$ is the functional probability distribution. This distribution describes the behavior of color sources with changing rapidity and H is the Hamiltonian of the JIMWLK equation given by

$$H = -\frac{1}{16\pi^3} \int_{uvw} M_{uvw} (1 + V_u^\dagger V_v - V_u^\dagger V_z - V_z^\dagger V_v)^{ab} \frac{\delta}{\delta \alpha_u^a} \frac{\delta}{\delta \alpha_v^b}, \quad (1.33)$$

here α_u^a is a gauge invariant functional. The notation for the integral follows $\int_{u..} = \int du^2$ and M is the kernel given by expression

$$M^{uvz} = \frac{(u-v)^2}{(u-z)^2(z-v)^2}. \quad (1.34)$$

V_x^\dagger and V_x are Wilson lines given by

$$V_x^\dagger = P \exp\left\{ig \int_{-\infty}^{\infty} dz^- \alpha_a(z^-, x)\right\} \quad (1.35)$$

where P denotes that the z^- is path-ordered [61].

1.3.2 Balitsky-Kovchegov evolution equation

Balitsky-Kovchegov evolution equation (BK) is one of the equations that describe the evolution of the scattering amplitude N . It was derived from the JIMWLK evolution equations in the limit of large number of colors N_c by Kovchegov [10, 62, 63]. It is a modification of the BKFL evolution equation and unlike BFKL, does account for the nonlinear effects of gluon recombination. The BK evolution equation is shown in Eq. 1.36 [64, 65]

$$\frac{\partial N(r, Y)}{\partial Y} = \int d\vec{r}_1 K^{run}(r, r_1, r_2) (N(r_1, Y) + N(r_2, Y) - N(r, Y) - N(r_1, Y)N(r_2, Y)), \quad (1.36)$$

where $K^{run}(r, r_1, r_2)$ can be expressed as in Eq. 1.37 [66]

$$K^{run}(r, r_1, r_2) = \frac{N_c \alpha_s(r^2)}{2\pi^2} \left(\frac{r^2}{r_1^2 r_2^2} + \frac{1}{r_1^2} \left(\frac{\alpha_s(r_1^2)}{\alpha_s(r_2^2)} - 1 \right) + \frac{1}{r_2^2} \left(\frac{\alpha_s(r_2^2)}{\alpha_s(r_1^2)} - 1 \right) \right) \quad (1.37)$$

and $\vec{r}_2 = \vec{r} - \vec{r}_1$. If we disregard the last term in the BK equation, we obtain a linear equation that can be shown to be equivalent to the BFKL evolution equation [45]. As the rapidity increases, this linearized version rises the scattering amplitude above any boundaries. The comparison to the BK equation is shown in Fig. 1.9.

QCD perturbative theory is only applicable for scales $Q^2 > \Lambda_{QCD}^2$, where the coupling constant is significantly low. In the low energy region, a non-perturbative approach is necessary. This would correspond to a low x strip along the y -axis in Fig. 1.10. Below the saturation scale, BFKL and other linear equations are valid and above this line we get dense and energetic systems described by the BK equation. This area of validity is shown in Fig. 1.10.

The coupling that is used in the kernel of the integro-differential equation depends on the number of considered quark flavors according to equation 1.38.

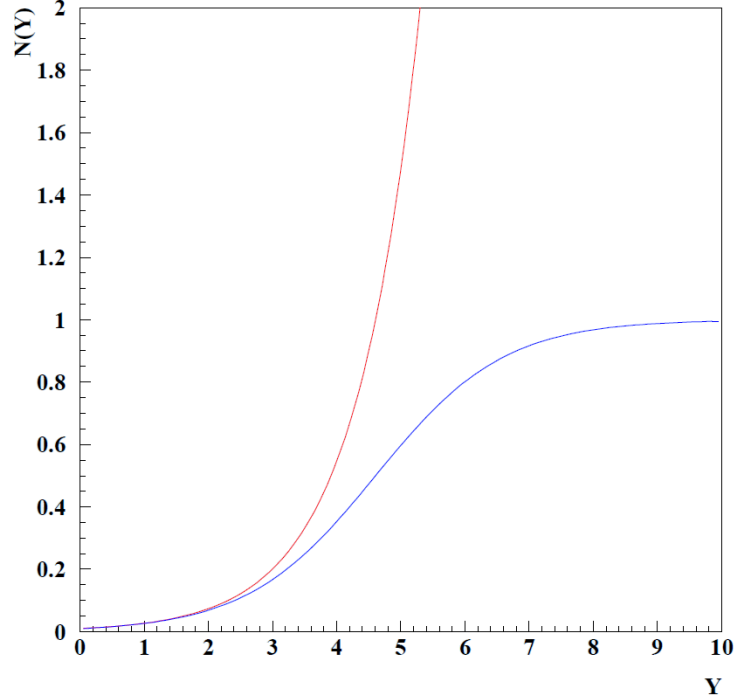


Figure 1.9: Comparison of the BK equation solutions (blue line) to the BFKL equation solutions (red line) [45].

$$\alpha_{s,n_f}(r^2) = \frac{4\pi}{\beta_{0,n_f} \ln \left(\frac{4C^2}{r^2 \Lambda_{n_f}^2} \right)}, \quad (1.38)$$

where

$$\beta_{0,n_f} = 11 - \frac{2}{3}n_f. \quad (1.39)$$

The constant C^2 is the uncertainty coming from the Fourier transformation that was used to derive this result and is usually fit to data [44]. The constant n_f corresponds to the number of flavors that are active, and is usually set to a value of 3 in the light flavor quarks approximation.

$\Lambda_{n_f}^2$ is called the QCD scale parameter and its value depends on the value of n_f in the variable n_f scheme. When heavier quark flavors are active (charm and beauty quark) 1.3.2, its value needs to be calculated from the relation [21]

$$\Lambda_{n_f-1} = (m_f)^{1 - \frac{\beta_{0,n_f}}{\beta_{0,n_f-1}}} (\Lambda_{n_f})^{\frac{\beta_{0,n_f}}{\beta_{0,n_f-1}}}. \quad (1.40)$$

To determine the value of Λ_5 , the experimentally measured value of $\alpha_s(M_Z) = 0.1196 \pm 0.0017$ at the Z^0 mass $M_Z = 91.18 \text{ GeV}$ [67] and the Eq.1.38 can be used.

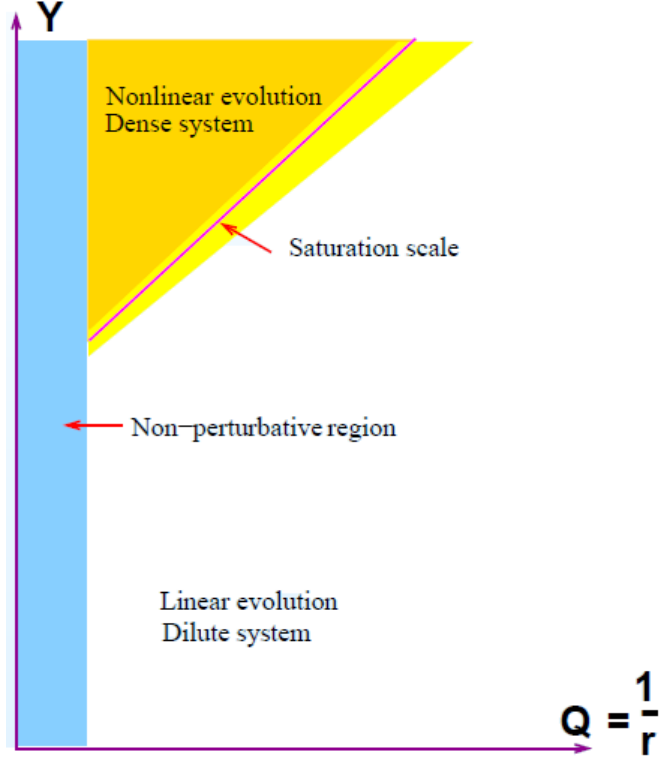


Figure 1.10: A schematic area distribution of validity for different evolution equations [45].

Value of n_f are set for values of r^2 for which the momentum scale is heavier than the heaviest quark considered. This condition can be expressed as

$$r^2 < \frac{4C^2}{m_f^2}. \quad (1.41)$$

Since all dipole sizes are accounted for in the BK evolution equation, there is a need to reduce the coupling after a certain value is reached, so that the maximal value of coupling constant would not exceed a set limit [21, 44]. The modified running coupling takes into account the next to leading two loop expressions [33].

In order to compute the Balitsky Kovchegov evolution equation and get the cross section of the whole interaction or a structure function of a hadron, one must start with certain initial conditions. One of the frequently used initial conditions is the GBW initial condition Eq. 1.42 [44].

$$N^{GBW}(r, x = x_0) = 1 - \exp\left(-\frac{(r^2 Q_0^2)^\gamma}{4}\right) \quad (1.42)$$

Another typical initial condition for the BK equation is a MV initial condition 1.43 [68]

fit	Q_0^2	C	$\Lambda_{n_f}^2$	γ	σ_0
GBW	0.241	2.46	0.241	0.971	32.357
MV	0.165	$\sqrt{6.5}$	0.241	1.13	32.895

Table 1.1: A possible values of the initial condition parameters [21].

$$N^{MV}(r, x = x_0) = 1 - \exp\left(-\frac{(r^2 Q_0^2)^\gamma}{4} \ln\left(\frac{1}{r\Lambda} + e\right)\right) \quad (1.43)$$

Where Λ represents the infrared cutoff of the dipole cross section and does not have to be equal to $\Lambda_{n_f}^2$ introduced earlier [44], Q_0^2 is the scale for the biggest Bjorken x that is considered in the computation and γ is a parameter that controls the slope of the fall of the dipole amplitude when r is decreased. However the BK evolution equation does not incorporate the quantum fluctuations of the gluon field and therefore its saturation scale is not entirely accurate. The fluctuations are not accounted for in the fixed coupling approach. The running coupling approach shown in Eq. 1.38 evens its effects out [45]. Table 1.3.2 shows possible values for the initial parameters.

Chapter 2

Numerical methods

2.1 Runge-Kutta method

The Runge-Kutta method is a commonly used method of solving linear differential equations such as 2.1. Let us consider following notation, $y(x)$ is the desired function,

$$y'(x) = f(x, y) \quad (2.1)$$

and the initial condition is

$$y(a) = \varphi \quad (2.2)$$

The next step of this method is calculated as follows [69]

$$K(x, y, h) = w_1k_1 + w_2k_2 + w_3k_3 + \dots + w_s k_s \quad (2.3)$$

where

$$k_i = f \left(x + \alpha_i h, y + h \sum_{j=1}^{i-1} \beta_{i,j} k_j \right), i = 2, \dots, s. \quad (2.4)$$

where α_i and $\beta_{i,j}$ are constants that we match to the Taylor's expansion as accurately as possible. Solving an equation according to the Runge-Kutta method, one must compute the right side of equation 2.1 in multiple points but does not need to make any additional derivatives. The constants $w_1k_1, w_2k_2, w_3k_3, \dots, w_s k_s$ fulfill a condition

$$w_1k_1 + w_2k_2 + w_3k_3 \dots + w_s k_s = 1 \quad (2.5)$$

but they vary for different orders of the Runge-Kutta method. The way a new step in the RK method is computed is shown in Eq. 2.6.

$$y_{n+1}(x_{n+1}) = y_n + hK_n(x, y, h) \quad (2.6)$$

2.1.1 First order - Euler Method

The Euler method is a way to compute a linear first order differential equation. Strictly speaking, the Euler method is a first order Runge-Kutta method. The simplicity of this method comes from the fact that for the computation of the next step y_{n+1} one needs to know only the function behavior on a neighborhood of the coordinate x_n . The Euler method reads:

$$y_{n+1} = y_n + f(x_n, y_n), n = 0, 1, 2, \dots, x_n \in [a, b] \quad (2.7)$$

This method is discrete. That means that its solution will be found only in certain selected coordinates x_n where $n = 0, 1, 2, 3, \dots, N$. Equidistant selection of x_n simplifies the solution. In this approach we can introduce the integration step of the Euler method h as in Eq. 2.8.

$$x_n = a + nh, n = 0, 1, 2, \dots \quad (2.8)$$

an analogous approach to the problem of solving this kind of differential equation would be Picard's method which integrates the whole equation 2.1 and then solves it as in Eq. 2.9 [69].

$$y(x) = \varphi + \int_a^x f(t, y(t))dt \quad (2.9)$$

If the right side of equation 2.1 fulfills the conditions of being defined and continuous for $a \leq x \leq b$ and $-\infty \leq y \leq \infty$ and if there exists a constant L for which it holds that

$$| f(x, y) - f(x, z) | \leq L | y - z | \quad (2.10)$$

for every $x \in [a, b]$ and for arbitrary y and z , the solution of such equation exists on the whole interval $[a, b]$ [69].

The graphical interpretation of the Euler method is simple. The method takes the slope of the desired function at its initial point and linearly interpolates this function to get the next point after the length of integration step h . This process is repeated until the approximated function is obtained.

The total error of the Euler method is not easy to compute and confine because it accumulates as the method continues and depends only on one parameter of this method and that is the integration step h . It is easier to state the local discrete error which states the error of this method after one step assuming that all the previously used values are correct, see Eq. 2.11 [69].

$$L(y(x), h) = y(x + h) - y(x) - hf(x, y(x)) \quad (2.11)$$

The total error is then given by the multiple local errors piling up with the fact that the starting values of next steps are already shifted from the original function. If this accumulation does not reach too high values, the method is said to be stable.

2.1.2 Second order - Ralston method

As an example of the Runge-Kutta method of second order we can take the Ralston method [69]. This method is more accurate than just the simple Euler method because it takes into account the behavior of the function not only on the neighborhood of the x_n but as well on the neighborhood of $x_n + \frac{2}{3}h$. The next step and its coefficients k_1 and k_2 are calculated as follows.

$$\begin{aligned} y_{n+1} &= y_n + h \left(\frac{1}{4}k_1 + \frac{3}{4}k_2 \right) \\ k_1 &= f(x_n, y_n) \\ k_2 &= f \left(x_n + \frac{2}{3}h, y_n + \frac{2}{3}hk_1 \right) \end{aligned} \quad (2.12)$$

2.1.3 Fourth order

One of the very often used types of Runge-Kutta methods is the Runge-Kutta method of fourth order for which the setup is as shown in Eq. 2.13

$$\begin{aligned} y_{n+1} &= y_n + \frac{1}{6}h(k_1 + 2k_2 + 2k_3 + k_4) \\ k_1 &= f(x_n, y_n) \\ k_2 &= f \left(x_n + \frac{1}{2}h, y_n + \frac{1}{2}hk_1 \right) \\ k_3 &= f \left(x_n + \frac{1}{2}h, y_n + \frac{1}{2}hk_2 \right) \\ k_4 &= f(x_n + h, y_n + hk_3) \end{aligned} \quad (2.13)$$

This method is by far the most common of the Runge-Kutta methods, so often when referred to RK method without further specification, this particular setup is considered. Similar to the Euler method, to get the total error of the Runge-Kutta method, we need to know the local discrete error for a single step with correct initial parameters.

If in a neighborhood of point (x_n, y_n) holds

$$|f(x, y)| < M, \quad \left| \frac{\partial_{i+j} f}{\partial x^i \partial y^j} \right| < \frac{L^{i+j}}{M^{j-1}}, \quad i + j \leq p \quad (2.14)$$

then the error of the method of fourth order is [69]

$$\begin{aligned}
|L(y(x_n), h)| &< (16|b_1| + 4|b_2| + |b_2 + 3b_3| + |2b_2 + 3b_3| + \\
&|b_2 + b_3| + |b_3| + 8|b_4| + |b_5| + |2b_5 + b_7| + |b_5 + b_6 + b_7| \\
&+ |b_6| + |2b_6 + b_7| + |b_7| + |2b_8|)h^5ML^4
\end{aligned} \tag{2.15}$$

where the constants b_i , $i = 1, 2, 3, 4, 5, 6, 7$ are as follows:

$$\begin{aligned}
b_1 &= \frac{1}{120} - \frac{1}{2}(\alpha_2^4 w_2 + \alpha_3^4 w_3 + w_4), \\
b_2 &= \frac{1}{20} - \frac{1}{2}(\alpha_2 \alpha_3^2 \beta_{32} w_3 + (\alpha_2 \beta_{42} + \alpha_3 \beta_{43}) w_4), \\
b_3 &= \frac{1}{120} - \frac{1}{6}(\alpha_2^3 \beta_{32} w_3 + (\alpha_2^3 \beta_{42} + \alpha_3^3 \beta_{43}) w_4), \\
b_4 &= \frac{1}{30} - \frac{1}{2}(\alpha_2^2 \alpha_3 \beta_{32} w_3 + (\alpha_2^2 \beta_{42} + \alpha_3^2 \beta_{43}) w_4), \\
b_5 &= \frac{1}{120} - \frac{1}{2} \alpha_2^2 \beta_{32} \beta_{43} w_4, \\
b_6 &= \frac{1}{40} - \frac{1}{2}(\alpha_2^2 \beta_{32} w_3 + (\alpha_2 \beta_{42} + \alpha_3^2 \beta_{43})^2 w_4), \\
b_7 &= \frac{7}{120} - \alpha_2(1 + \alpha_3) \beta_{32} \beta_{43} w_4, \\
b_8 &= \frac{1}{120}.
\end{aligned} \tag{2.16}$$

For the often used version of Runge-Kutta method of fourth order given by Eq.2.13, the expression for an error after a single step is

$$|L(y(x_n), h)| < \frac{73}{720} h^5 ML^4 \tag{2.17}$$

where L is a constant. Since this local error is strongly step dependent, it is in principle possible to consider Runge-Kutta methods with variable integration step length, that is chosen in every point on the grid so that the local error is constant everywhere. This can be achieved by the equation 2.18, where computing the local error simultaneously with the main computation in every other step slows the whole program down approximately by 50% [69].

$$\phi(x_n, y(x_n))h^{p+1} = \frac{1}{2^{p+1} - 1}(y_{n+1} - y_{n+1}^*) \tag{2.18}$$

where y_{n+1} is a solution with the integration step h at x_{n+1} , y_{n+1}^* is a solution with integration step $2h$ at $x = x_{n+1}$ and p is the order of the local discrete error. It is the largest integer for which holds that

$$L(y(x); h) = O(h^{p+1}). \tag{2.19}$$

2.2 Simpson method

Simpson method is a numerical way of computing an integral of a function if the values of the integrated function are known over the interval we want to integrate it over. This method is a method composed [69], which means that another method is used for its construction, in this case it is the Newton-Cotes integration formula.

These formulas approximate the integral

$$I(f) = \int_b^a f(x)dx \quad (2.20)$$

by adding values of the integrated function in certain points on the x-axis multiplied by a factor H_i as shown in Eq. 2.21 [69].

$$I_{n+1}(f) = \sum_{i=0}^n H_i f(a_i), \quad (2.21)$$

where a_i are distributed in the interval $[a, b]$. The Newton-Cotes integration formula is a method that uses equidistant spacing of these a_i points and values of H_i are chosen so that the order of this method (maximal order of a polynomial that is integrated without error) is maximal.

Simpson method divides the interval $[a, b]$ into $m/2$ subintervals $[a_{2i}, a_{2i+2}]$ where $i = 0, 1, 2, \dots, m/2 - 1$, and uses the closed Newton-Cotes formula on each one of them separately. The approximate integral is then given by the Eq. 2.22 [69].

$$\int_b^a f(x)dx = \frac{h}{3}(f(a_0) + 4f(a_1) + 2f(a_2) + 4f(a_3) + \dots + 4f(a_{m-3}) + 2f(a_{m-2}) + 4f(a_{m-1}) + f(a_m)) + E(f), \quad (2.22)$$

where h is the integration step given by $h = \frac{(b-a)}{m}$, m is an even integer and $E(f)$ is the error of the method given by [69]

$$E(f) = \int_b^a f(x)dx - \sum_{i=0}^n H_i f(a_i). \quad (2.23)$$

The error of Simpson method can be determined using expression 2.24 [69]

$$E(f) = -\frac{(b-a)}{180} h^4 f^{(4)}(\zeta), \quad (2.24)$$

where $f^{(4)}$ is the fourth derivative of the f function and ζ is a number from the interval $[a, b]$.

2.3 Lagrange interpolation

Lagrange formula is a way to compute a polynomial interpolation of any order for a fixed set of points. The interpolation is given by formula 2.25 [69]

$$L_n(x) = \sum_{i=0}^n f(a_i)l_i(x) \quad (2.25)$$

where the factor $l_i(x)$ is given by expression

$$l_i(x) = \frac{(x - a_0)\dots(x - a_{i-1})(x - a_{i+1})\dots(x - a_n)}{(a_i - a_0)\dots(a_i - a_{i-1})(a_i - a_{i+1})\dots(a_i - a_n)}. \quad (2.26)$$

The error of Lagrange interpolation formula can be computed by equation 2.27 [69]

$$E(x) = \frac{(x - a_0)(x - a_1)\dots(x - a_n)}{(n + 1)!} f^{(n+1)}(\zeta). \quad (2.27)$$

Lagrange interpolation coefficients $l_i(x)$ for a polynomial of third order that will be used later on will then be

$$\begin{aligned} l_0(x) &= \frac{(x - a_1)(x - a_2)(x - a_3)}{(a_0 - a_1)(a_0 - a_2)(a_0 - a_3)} \\ l_1(x) &= \frac{(x - a_0)(x - a_2)(x - a_3)}{(a_1 - a_0)(a_1 - a_2)(a_1 - a_3)} \\ l_2(x) &= \frac{(x - a_0)(x - a_1)(x - a_3)}{(a_2 - a_0)(a_2 - a_1)(a_2 - a_3)} \\ l_3(x) &= \frac{(x - a_0)(x - a_1)(x - a_2)}{(a_3 - a_0)(a_3 - a_1)(a_3 - a_2)}. \end{aligned} \quad (2.28)$$

The simple linear interpolation is a Lagrange interpolation of first order and the coefficients then are

$$\begin{aligned} l_0(x) &= \frac{(x - a_1)}{(a_0 - a_1)} \\ l_1(x) &= \frac{(x - a_0)}{(a_1 - a_0)} \end{aligned} \quad (2.29)$$

Chapter 3

Solving the rcBK equation

3.1 Impact parameter independent rcBK equation

The Balitsky-Kovchegov equation unfortunately does not have an analytic solution, so it has to be solved numerically such as in [19–21]. A usual way of solving this equation involves the Simpson method for integration, a linear interpolation for acquiring values of $N(r)$ for intermediate positions and the Runge-Kutta method for solving the differential equation.

Since both the Simpson method and the Runge-Kutta method use points in grid and not continuous functions, the initial condition is computed on an equidistant grid with step h . We choose to set a logarithmic grid over the dipole distance vector \vec{r} (and later also for the impact parameter \vec{b}) To obtain the next step in rapidity evolution, one must use the RK method and therefore compute the integral

$$\int d\vec{r}_1 K^{run}(r, r_1, r_2)(N(r_1, x) + N(r_2, x) - N(r, x) - N(r_1, x)N(r_2, x)). \quad (3.1)$$

This integral depends on the value of r , so it is necessary to compute it for every value of r on the whole considered interval separately. To compute this integral, Simpson method was used. That means that for every value of r , a cycle has been run for the whole interval integrating the function over \vec{r}_1 , where the value of r_2 was computed according to

$$r_2 = \sqrt{r^2 + r_1^2 - 2rr_1 \cos(\theta_{rr_1})} \quad (3.2)$$

where θ_{rr_1} is the angle between \vec{r} and \vec{r}_1 . If the point r_2 does not match exactly one of the grid points on which the values of the initial condition has been computed, it is necessary to interpolate. Lagrange interpolation of first or third order is considered since even values of interpolations order tend to inaccurately interpolate linear regions.

For every point r_1 inside the integral 3.1, integral over θ_{rr_1} has been computed. This variable goes from 0 to 2π but since cosine is an even function, we can simplify this by integrating over $[0, \pi]$ instead and multiplying the result by a factor of two. Once the function is integrated over θ_{rr_1} in every point r_1 , it is possible to integrate these integrated functions and determine the final integral. This integral can be split in three separate terms:

$$\begin{aligned}
Kernel &= \int d^2\vec{r}_1 K^{run}(r_1, r_2, r) \\
Split &= \int d^2\vec{r}_1 K^{run}(r_1, r_2, r)(N(Y, r_1) + N(Y, r_2)) \\
Recomb &= \int d^2\vec{r}_1 K^{run}(r_1, r_2, r)(N(Y, r_1)N(Y, r_2)),
\end{aligned} \tag{3.3}$$

which allows us to speed up the Runge-Kutta method as described in the Appendix A. These three terms are then used to compute the next step in the rapidity evolution and this step is then added to the initial condition in every point of r . The obtained function be used as an input to this process until the desired rapidity is reached.

To speed up this process, it is useful to create a three-dimensional array in the very beginning of the computation that will hold the values of $K^{run}(r, r_1, r_2)$ for every combination of r, r_1 and r_2 so that they don't have to be computed over and over. Same principle was used to hold the values of $r_2(r, r_1, \theta_{rr_1})$.

To determine the values of $\alpha_{run}(r^2)$, equation 1.38 is used on a region, where $r > r_{run}$ holds. The value of r_{run} is chosen so that the total value of $\alpha_{run}(r^2)$ would never exceed the value of 0.7 [21].

For some choices of r, r_1 and θ_{rr_1} the value of $K^{run}(r, r_1, r_2)$ diverges. It is then necessary to exclude these points from the whole integral, because whereas in continuous integration a diverging singularity does not necessarily mean divergence of the entire integral, in the discrete approximation an infinite value added to the integration sum changes the result irreversibly.

3.2 Geometric Scaling

The solution of the BK evolution equation exhibits a phenomenon called Geometric scaling [24]. After a few units of rapidity, the initial condition is "forgotten" by the evolution and the solution propagates independently. Moreover, as rapidity increases, its geometric properties do not change, the solution only shift towards lower values of r . This then allows us to either predict future values of the evolution, or "rewind" back the evolution and hope to obtain a new initial condition to this integro-differential equation, that would require less parameters and that would be obtained solely from the intrinsic properties of the BK equation. The evolution of the solution to the BK equation is shown in Fig. 3.1 where we can see the effect of geometric scaling.

The evolution equation itself forgets the shape of the initial condition in the evolution

in few units of rapidity. Even if we choose to start with dramatically different initial conditions, by the rapidity $Y = 8$ the solution yields its usual shape.

Figure 3.2 shows the evolution for a simple linear initial condition that has a value of 0 for all dipole sizes below 1, linearly grows to one in the (1,10) interval and has a value of 1 elsewhere. Even more extreme initial condition was considered in Figure 3.3, that shows the evolution for an initial condition that exceeds the value of 1 for $N(r, Y)$. It has a value of 0 for r smaller than 1, linearly grows up to the value of 1.5 at the dipole size of twenty, and is set to 1 for larger dipole sizes. Final initial condition that was tested is shown in Fig. 3.4. It does not reach the value of one for $N(r, Y)$ anywhere on the interval and is set to 0 for the dipole sizes smaller than one, grows linearly to the value of 0.5 at $r = 5$ and stays at that value for the remaining part of the interval. Note that the dipole size axis is in the logarithmic scale.

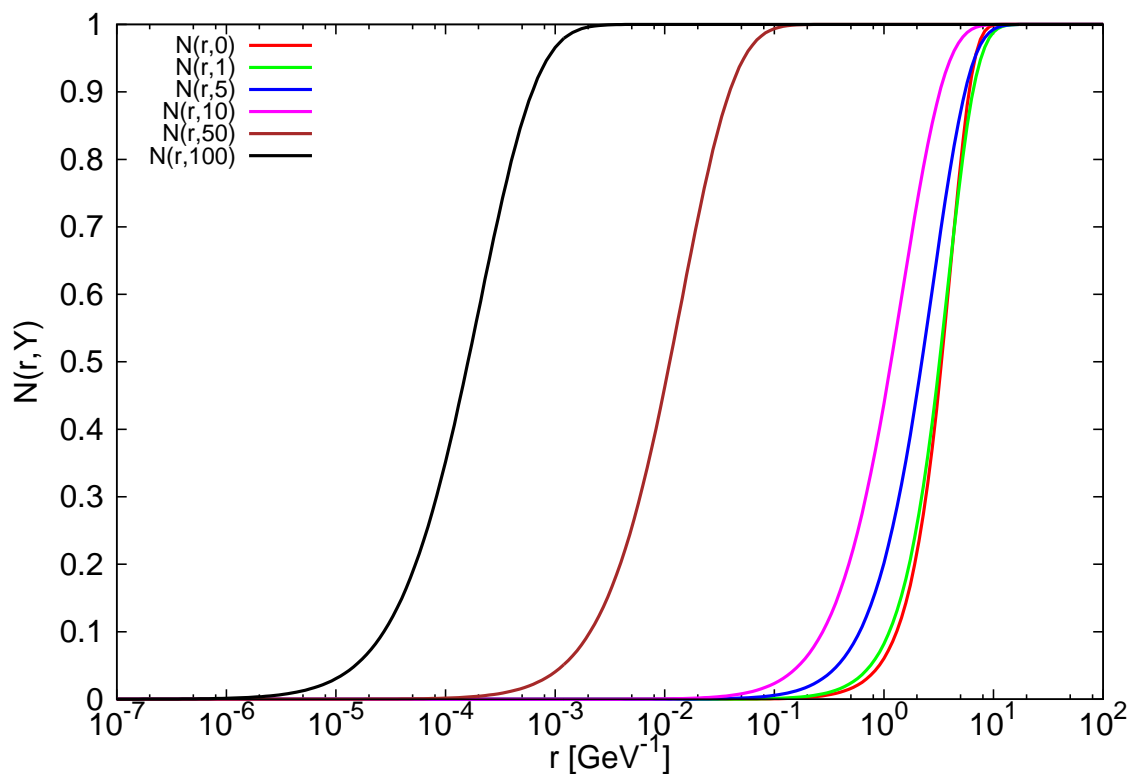


Figure 3.1: The shape of the solution to the BK equation shows geometric scaling properties.

We can see that these extreme initial conditions seem not to affect the later evolution and that the evolution equation itself shapes the curve into a predetermined shape. In all of these cases we can see that by rapidity of about 10, the shape of the initial condition is suppressed and that the evolution then continues similarly for all initial conditions.

For obtaining the geometrically scaled solution, we ran the MV initial condition to high rapidity ($Y = 100$) where the integro-differential equation "forgot" the shape of the initial condition and then re-scaled it to the starting value.

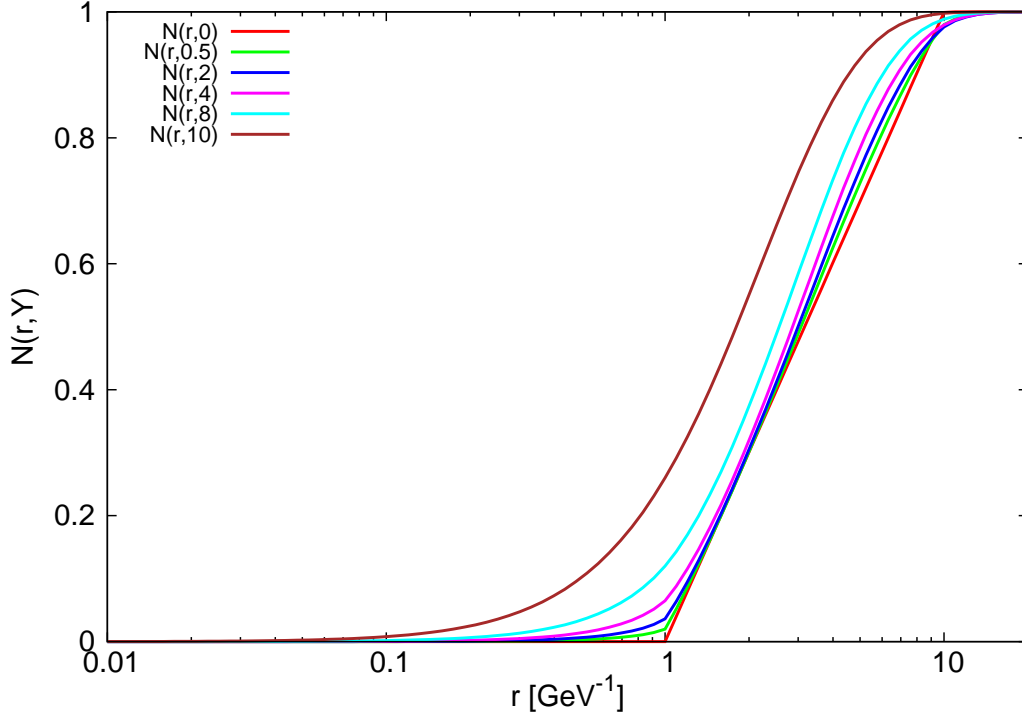


Figure 3.2: Evolution of $N(r, Y)$ when a simple linear initial condition is used.

First, we found r_s^{100} according to the condition.

$$N(r_s^{100}, Y = 100) = 0.5, \quad (3.4)$$

and then we computed the value of r_s^0 from the saturation scale as

$$Q_{s0} = 1/r_s^0. \quad (3.5)$$

The saturation scale Q_{s0}^2 is a free parameter that needs to be fitted from the data. Since for such obtained value of r_s^0 stands

$$N(r_s^0, Y = 0) = 0.5, \quad (3.6)$$

we then calculated the shift in the r -axis in logarithmic scale according to

$$\Delta r = \ln(r_s^{100}) - \ln(r_s^0) \quad (3.7)$$

and then re-scaled the solution to the rcBK equation as

$$N(\ln(r), Y = 0) = N(\ln(r) - \Delta r, Y = 100). \quad (3.8)$$

We linearly interpolated when the values of $\ln(r) - \Delta r$ got of the precomputed grid.

The initially considered value for the saturation scale was set as $Q_{s0}^2 = 0.07 \text{ GeV}^2$. The values of $\frac{F_2^{data}}{F_2^{rcBK}}$ were evaluated and fitted with a constant to determine the new value of σ_0 since the original value obtained with MV initial conditions can differ. A second propagation to $Y = 100$ and re-scaling of the initial condition was carried out to determine the validity of the assumption that by $Y = 100$, the rcBK equation "forgot" its initial condition.

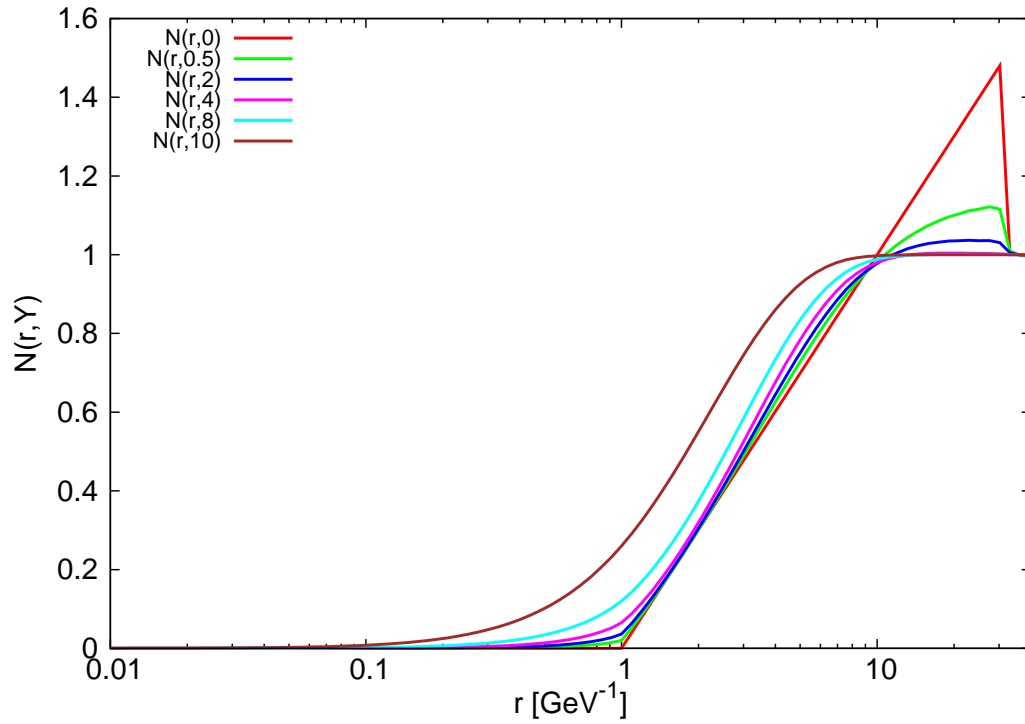


Figure 3.3: Evolution of $N(r, Y)$ when an atypical initial condition is used, that exceeds the value of one.

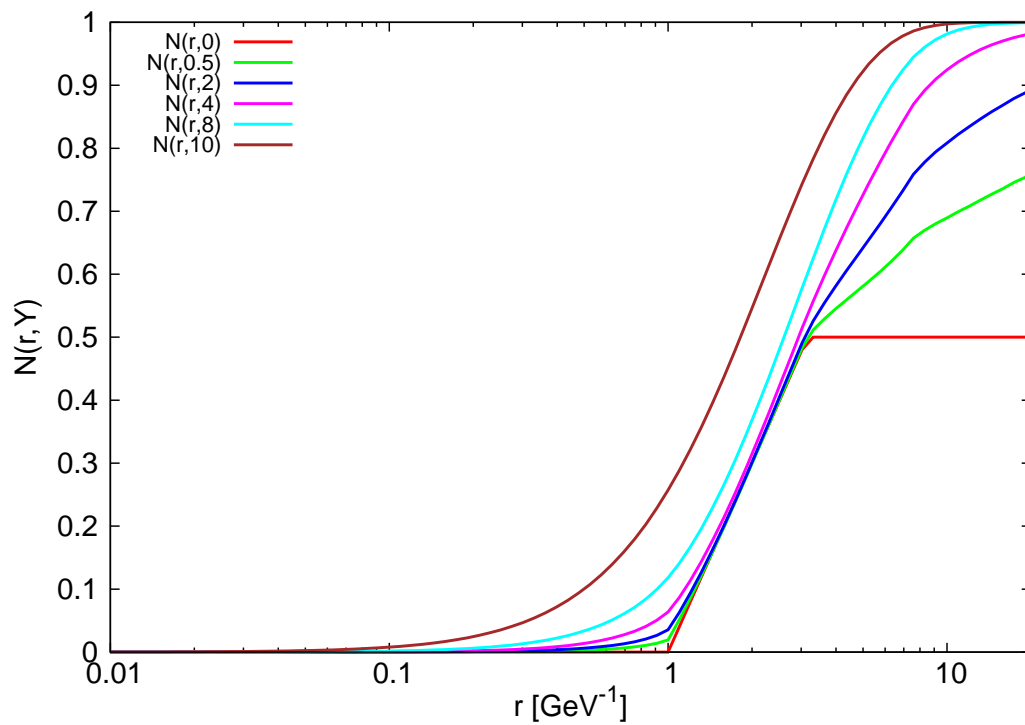


Figure 3.4: Evolution of $N(r, Y)$ when an atypical initial condition is used, that does not reach one.

3.3 Impact parameter dependent rcBK equation

A frequent approach to solve the BK evolution equation is to suppose the independence of the solution on the impact parameter as done in Section 3.1. That is to assume homogeneous distribution of partons inside the hadron. The computation then simplifies and CPU time is dramatically reduced. However knowing the scattering amplitude behavior when the impact parameter dependence is not neglected proves to be a viable source of information on the saturation effects. Heterogeneously distributed partons within the hadron can contribute to saturation effects differently and the dynamics of various processes can be altered.

In this approach, the original approximation

$$\int N(x, r, \vec{b}) d\vec{b} = \sigma_0 N(x, r) \quad (3.9)$$

has to be discarded and the dipole cross section has to be calculated as

$$\sigma(r, x) = 2 \int d\vec{b} N(x, r, \vec{b}), \quad (3.10)$$

where for $N(x, r, \vec{b})$, we have assumed a nontrivial b-dependence. This approach makes the computation much more demanding. While maintaining same precision as in the last case, one run would take 60 hours instead of few minutes. In the b-dependent BK equation computation, it is also necessary to include the integration over the full interval $[0, 2\pi]$ of θ_{rr_1} rather than restricting ourselves to $[0, \pi]$ and multiplying the result by a factor of two since this angle is used to compute the absolute values of the impact parameters that are necessary for the computation. During the computation and for a single step in rapidity for a chosen value of r , the values of b , θ_{rb} and of course r are constants. θ_{rr_1} is a parameter of the computation that we run an integration over so its value is also known. The scheme of this geometry is shown in Fig.3.5. The value of r_2 is computed according to

$$r_2 = \sqrt{r^2 + r_1^2 - 2rr_1 \cos(\theta_{rr_1})}. \quad (3.11)$$

Then we can compute the value of the angle θ_{rr_2} as shown in Eq. 3.12, this parameter stands for the angle between \vec{r} and \vec{r}_2 .

$$\theta_{rr_2} = \arccos \left(\frac{r_2^2 + r^2 - r_1^2}{2rr_2} \right) \quad (3.12)$$

With these relations, we are able to compute the two missing pieces necessary for the computation of the integral of the right hand side of the BK equation. The values of b_1 and b_2 can then be obtained from

$$b_1 = \left| \vec{b} + \frac{\vec{r}_2}{2} \right| = \sqrt{b^2 + \frac{r_2^2}{4} + br_2 \cos(\theta_{br_2})} \quad (3.13)$$

and

$$b_2 = \left| \vec{b} - \frac{\vec{r}_1}{2} \right| = \sqrt{b^2 + \frac{r_1^2}{4} - br_1 \cos(\theta_{br_1})}, \quad (3.14)$$

where the angles θ_{br_1} and θ_{br_2} are obtained from the fact that

$$\theta_{br_1} = \theta_{br} + \theta_{rr_1} \quad (3.15)$$

and

$$\theta_{br_2} = \theta_{br} + \theta_{rr_2}. \quad (3.16)$$

Of course, the values of the impact parameters computed this way do not always fall on the precomputed grid of values. Therefore it is necessary to add another linear interpolation to the one in the dipole size dimension. Every time the value of b_2 gets off the grid, we need to carry out two linear interpolations in the r axis for obtaining the values of the scattering amplitude in two points in the b axis and then we can finally interpolate to obtain the desired value of $N(r_2, b_2, Y)$. These relations give us all the parameters we need to carry out the integration and compute the next step of the Runge-Kutta method to obtain the scattering amplitude at higher values of Y .

One of the possible initial conditions for this computation is

$$N(r, b, 0) = 1 - \exp[-cr^2 \exp(-db^2)], \quad (3.17)$$

where the usual testing setup of parameters is $c = 10$ and $d = 1/2$ [29]. The Balitsky-Kovchegov evolution equation in this approach reads

$$\begin{aligned} \frac{\partial N_{x_0 x_1}}{\partial Y} = & \int \frac{d^2 x_2}{2\pi} K(x_{01}, x_{12}, x_{02}) \theta\left(\frac{1}{m^2} - x_{12}^2\right) \theta\left(\frac{1}{m^2} - x_{02}^2\right) \cdot \\ & \cdot (N_{x_{02}} + N_{x_{21}} - N_{x_{01}} - N_{x_{02}} N_{x_{21}}), \end{aligned} \quad (3.18)$$

where $N_{x_{ij}}$ equals $N(r_{ij} = x_i - x_j, \vec{b}_{ij} = \frac{x_i + x_j}{2}, Y)$ and m is a cutoff parameter that takes into account the confinement of strong interaction, its value was set to $m = 0.35 \text{ GeV}$ [29]. It restricts the dipoles to emit dipoles with dipole distance greater than $r_{max} = \frac{1}{m}$. The kernel of this BK equation then reads

$$\begin{aligned} K(x_{01}, x_{12}, x_{02}) = & \frac{N_c \alpha_s(x_{01}^2)}{\pi^2} \cdot \\ & \left(\frac{1}{x_{02}^2} \left(\frac{\alpha_s(x_{02}^2)}{\alpha_s(x_{12}^2)} - 1 \right) + \frac{1}{x_{12}^2} \left(\frac{\alpha_s(x_{12}^2)}{\alpha_s(x_{02}^2)} - 1 \right) + \frac{x_{01}^2}{x_{12}^2 x_{02}^2} \right). \end{aligned} \quad (3.19)$$

The variables x_{ij} determine vectors between the quarks in the color dipoles as shown in Fig. 3.5.

In order to carry out the computation, it is convenient to transform the equation into the form similar to 1.36. The corresponding transformation reads

$$\begin{aligned} \vec{r} &= \vec{x}_2 - \vec{x}_0 \\ \vec{r}_1 &= \vec{x}_1 - \vec{x}_0 \\ \vec{r}_2 &= \vec{x}_1 - \vec{x}_2 \end{aligned} \quad (3.20)$$

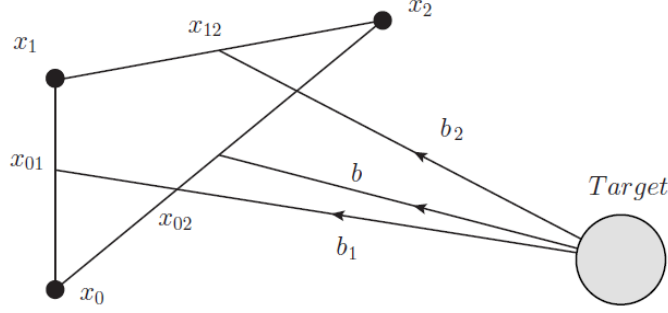


Figure 3.5: The color dipole triangle shows variables that are used in the BK equation [29].

and

$$\begin{aligned}
 \vec{b} &= \frac{\vec{x}_2 + \vec{x}_0}{2} \\
 \vec{b}_1 &= \frac{\vec{x}_1 + \vec{x}_0}{2} \\
 \vec{b}_2 &= \frac{\vec{x}_1 + \vec{x}_2}{2}
 \end{aligned} \tag{3.21}$$

therefore, if we transform the vector \vec{x}_2 , we get

$$\vec{x}_2 = \vec{b}_1 + \frac{\vec{r}_1}{2} = \vec{b} - \frac{\vec{r}_2}{2} + \frac{\vec{r}_1}{2} = \vec{b} - \frac{-\vec{r} + \vec{r}_1}{2} + \frac{\vec{r}_1}{2} = \vec{b} - \frac{\vec{r}}{2} + \vec{r}_1 \tag{3.22}$$

and since \vec{b} and $\frac{\vec{r}}{2}$ are treated as constants in the single step for a given position in $|\vec{r}|$, we can transform this equation into a more convenient form

$$\begin{aligned}
 \frac{\partial N(r, \vec{b}, Y)}{\partial Y} &= \int d\vec{r}_1 K^{run}(r, r_1, r_2) \theta\left(\frac{1}{m^2} - r_1^2\right) \theta\left(\frac{1}{m^2} - r_2^2\right) \cdot \\
 &\cdot (N(r_1, \vec{b}_1, Y) + N(r_2, \vec{b}_2, Y) - N(r, \vec{b}, Y) - N(r_1, \vec{b}_1, Y)N(r_2, \vec{b}_2, Y))
 \end{aligned} \tag{3.23}$$

Running coupling is then calculated in a similar manner as in the case with neglected b-dependence. The shape of the solution differs significantly from the solution obtained without the impact parameter dependence and is shown in Fig. 3.8 for the values of $b = 0.2 \text{ GeV}^{-1}$ and $b = 5 \text{ GeV}^{-1}$. If we add the impact parameter dependence, the evolution starts decreasing the value of the initial condition for large dipole sizes. This can be due to the fact that large dipoles do not interact with the hadron as easily, which is shown in Fig. 3.6. This figure depicts the two configurations that exhibit small scattering amplitude with a small value of impact parameter (Fig. 3.8 left). In the small dipole distance limit, the dipole can be treated as a white object which does not interact with the hadron and in the large dipole distance limit, the quarks are too far to interact at all.



Figure 3.6: The two dipole configurations for which the cross section of the interaction is small. [29].

The introduction of the impact parameter to our computation introduces two additional parameters that need to be taken into account in the numerical solution. In previous computation, we considered only the dipole size and rapidity as the computation parameters. Now we also add the absolute value of the impact parameter and the angle between the dipole and the impact parameter vector as shown in Fig. 3.7. This then prolongs the computation significantly since we consider the same grid size and step for the impact parameter as we did for the dipole size.

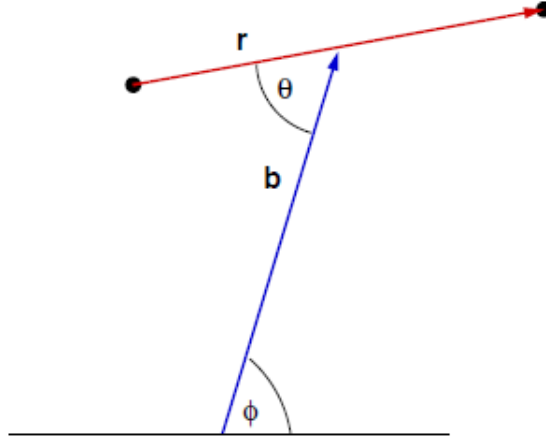


Figure 3.7: Schematic view of the angle between the impact parameter and the dipole distance vector [28].

In order to compute the structure function, we need to add the large dipole contribution that was taken out from the previous computation. This is then parametrized as

$$F_2^{soft} = \frac{Q^2}{2\pi\alpha_{em}} \sigma_0 \int_{\frac{z}{m}} \int_0^1 dz (|\Psi_L|^2 + |\Psi_T|^2), \quad (3.24)$$

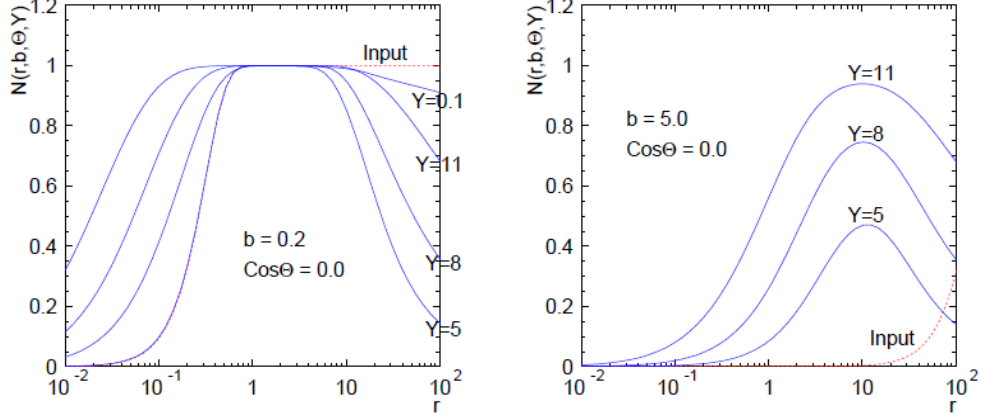


Figure 3.8: Solution to the rcBK equation with the b -dependence [28].

so the total structure function then is

$$F_2^{tot} = F_2^{BK} + F_2^{soft}. \quad (3.25)$$

The F_2^{BK} is the structure function obtained by the BK equation computation with cutoff parameter m .

A more physical initial condition that can be also used for the computation reads [29]

$$N_{GM}(r, b, Y) = 1 - \exp\left(-\frac{\pi^2}{2N_c} r^2 xg(x, \eta^2) T(b)\right) \quad (3.26)$$

where

$$T(b) = \frac{1}{8\pi} \exp\left(\frac{-b^2}{2B_G}\right). \quad (3.27)$$

The value of B_G is then chosen to be 4 GeV^{-2} , $\eta^2 = \frac{C}{r^2} + \eta_0^2$ where $C = 4$ and $\eta_0^2 = 1.16 \text{ GeV}^2$ [29]. The function $xg(x, \eta^2)$ is the integrated gluon density distribution.

These initial conditions simplify the full nature of this problem by ignoring the dependence on the angle between the impact parameter and the dipole. This dependence later emerges from the computation itself.

Chapter 4

Results

4.1 The Optimal Setup

To find the optimal setup of parameters that are used throughout the computation, their influence on the result has been analyzed [23]. For each parameter, it was necessary to find a reasonable ratio between precision and running time of the computation. Therefore each parameter has been varied and the amount of change to the resulting function was studied.

As a default computation setup, the MV initial condition with the value of parameters shown in Tab. 4.1 were used in the Runge-Kutta method of fourth order, 25 steps over each order of magnitude in r , 10 steps in the interval of $[0, \pi]$, 10000 steps in the integration over the interval $[0,1]$ of z in the photon wave function computation, linear interpolation method and a step of 0.01 over Y in the Runge-Kutta method.

The variations of the type of method where the Runge-Kutta method of fourth order, the Ralston method and the Euler method have been compared. We showed that the difference between results obtained by the Euler and RK2 methods is about twice as high as the difference between the RK2 and RK4 methods and is of the order of one percent of the total value. However the difference between the running times for the Euler method and the RK4 method is not as significant and therefore we will restrict ourselves to the RK4 in the following computations.

A variation for the integration step over the parameter θ_{rr_1} has been done. Steps of 5, 10, 20 and 40 have been compared at various rapidities to determine the optimal speed/precision ratio. The variation of the scattering amplitude when five steps over the interval of $[0, \pi]$ are considered instead of 10 reaches up to 25% for the rapidity of $Y = 10$ and decreases slowly with rising dipole size r . The change of the resulting

Fit	Q_0^2	C	$\Lambda_{n_f}^2$	γ	σ_0
MV	0.165	2.52	0.241	1.135	32.895

Table 4.1: Parameters for the default MV initial condition [21].

function when 20 steps are introduced instead of 10 over $[0, \pi]$ starts with a value of about 1% for the rapidity of 10 but decreases rapidly with increasing r . As we will see further in the thesis, the small values of r are not as important for the comparison to the experimental data because of the behavior of the wave function term. Increasing the steps further results in an even smaller variation of the scattering amplitude.

A variation over the integration step r has been done. The values of 10, 25, 50 and 100 per order of magnitude were compared. We have shown that the difference between the result obtained by the method using 10 steps per order of magnitude and 25 steps exceeds the value of 2% on the central part of the interval for the rapidity of 10. This region is particularly important for the precision of the obtained result as shown in the following section. When we use 50 steps per order of magnitude, the difference between the results obtained with 25 is less than 1% for most of the interval with the exception of values of r smaller than 10^{-6} . The scattering amplitude variation when 100 steps per order of magnitude are introduced has also less than 1% difference when compared to the previous 50 steps method.

Various methods of interpolation have been tested. As it turns out, the cubic interpolation is not good for this computation since it does not describe well the regions where the slope changes rapidly and an error is introduced into the evolution. For the evolution with the use of cubic interpolation, we have shown that in some regions, the value of $N(r, y)$ exceeds the value of one, which is violating the fact that its value have to fall within the $[0,1]$ interval.

The step of the Runge-Kutta method has also been varied. The obtained scattering amplitude can differ by 4% at rapidity $Y = 10$ when steps of 0.05 and 0.01 are compared, for further interval splitting (from 0.01 to 0.005) the scattering amplitude variation does not exceed the value of 0.6% at the rapidity of 10.

Therefore we conclude that for our case, we will restrict ourselves to use the set of computation parameters for the impact parameter independent rcBK as follows. Runge-Kutta method of fourth order, linear interpolation, a step in rapidity of 0.01, 25 steps over the order of magnitude in r and 10 steps over the interval $[0, \pi]$ in the integration over θ_{r_1} . We will assume that the b-dependent rcBK equation would exhibit a similar behavior since the methods and numerical complexity of the computation does not change.

4.2 rcBK solutions without impact parameter dependence

The Balitsky Kovchegov evolution equation was used to obtain the following results combined with Simpson's rule for integration and the Runge-Kutta method of fourth order for solving the differential equation. The optimized implementation of Runge-Kutta method for the special case of the BK evolution equation is described in the Appendix B.

The properties of the photon wave function $|\psi_{T,L}|^2$ weighted with several factors

that are needed to compute the proton structure function and reduced cross section are shown in the following figures as well as the evolution of $N(r, Y)$ with respect to rapidity and r . Fig. 4.2 shows the dependence of $|\psi_{T,L}|^2$ on r for different values of Q^2 .

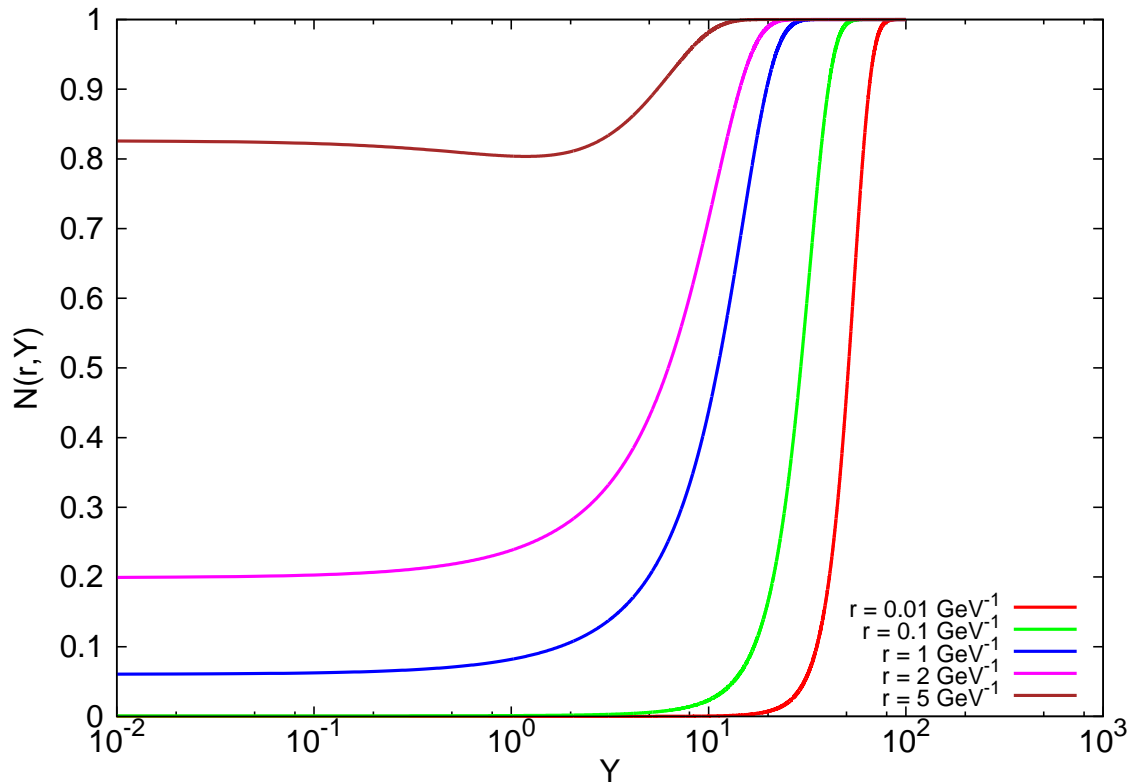


Figure 4.1: The dependence of $N(r, Y)$ on Y for various values of r .

To obtain the structure function $F_2(x, Q^2)$ for the b-independent case, it is only needed to integrate the function shown in Fig. 4.3 and multiply it by a constant factor. This function reaches a value of 10^{-8} at $r = 0.01 \text{ GeV}^{-1}$, which is below its maximum value by a factor of 10^{-4} . Similar situation occurs at $r = 40 \text{ GeV}^{-1}$. So the region of the main interest and desired precision for obtaining an accurate value of $F_2(x, Q^2)$ is $r \sim (0.1, 30) \text{ GeV}^{-1}$.

Figures 4.4 and 4.5 show the predicted values of the structure function and the reduced cross section for the b-independent case compared with the data from HERA.

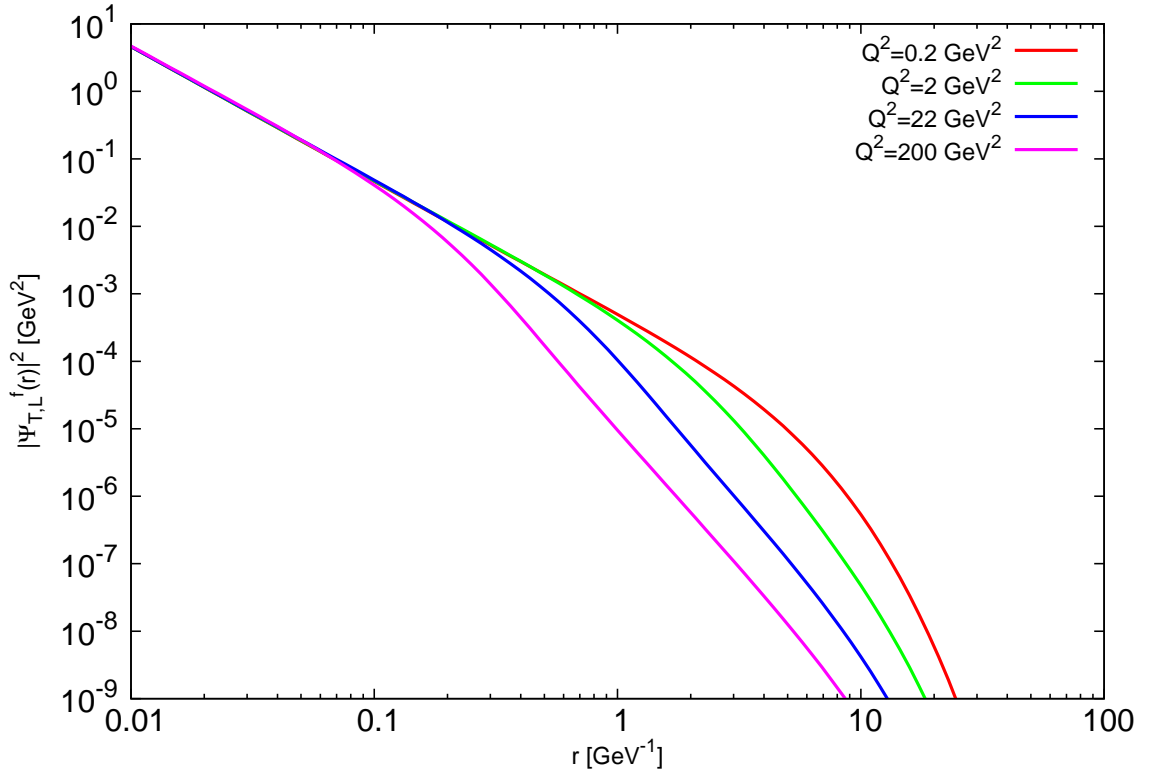


Figure 4.2: The photon wave function $|\psi_{T,L}|^2$ integrated over z .

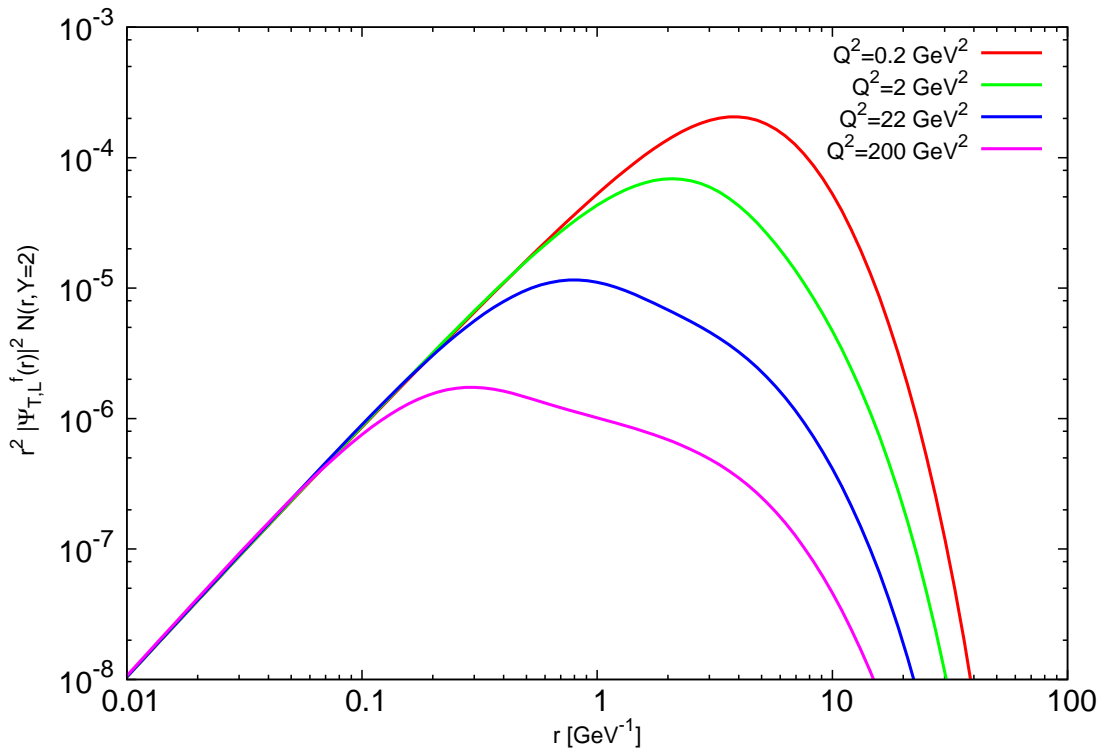


Figure 4.3: The photon wave function $|\psi_{T,L}|^2$ multiplied by the scattering amplitude $N(r, Y)$ and r^2 for various values of Q^2 .

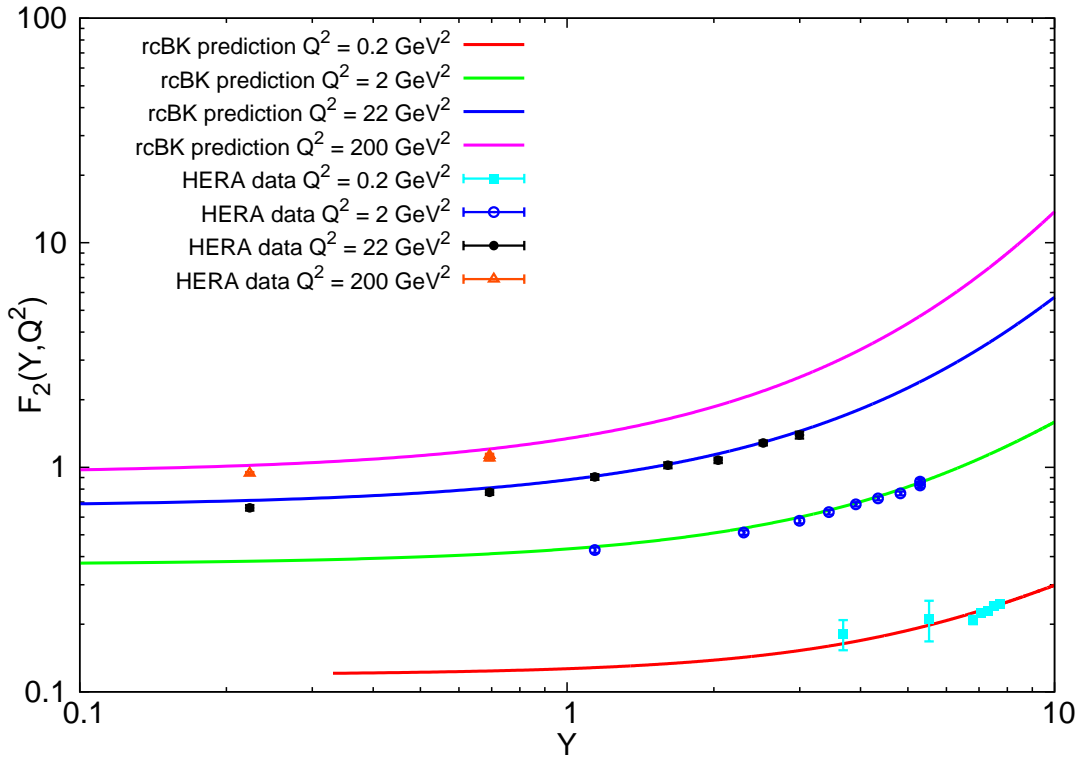


Figure 4.4: The dependence of the proton structure function $F_2(Y, Q^2)$ on Y and compared with data from HERA [70].

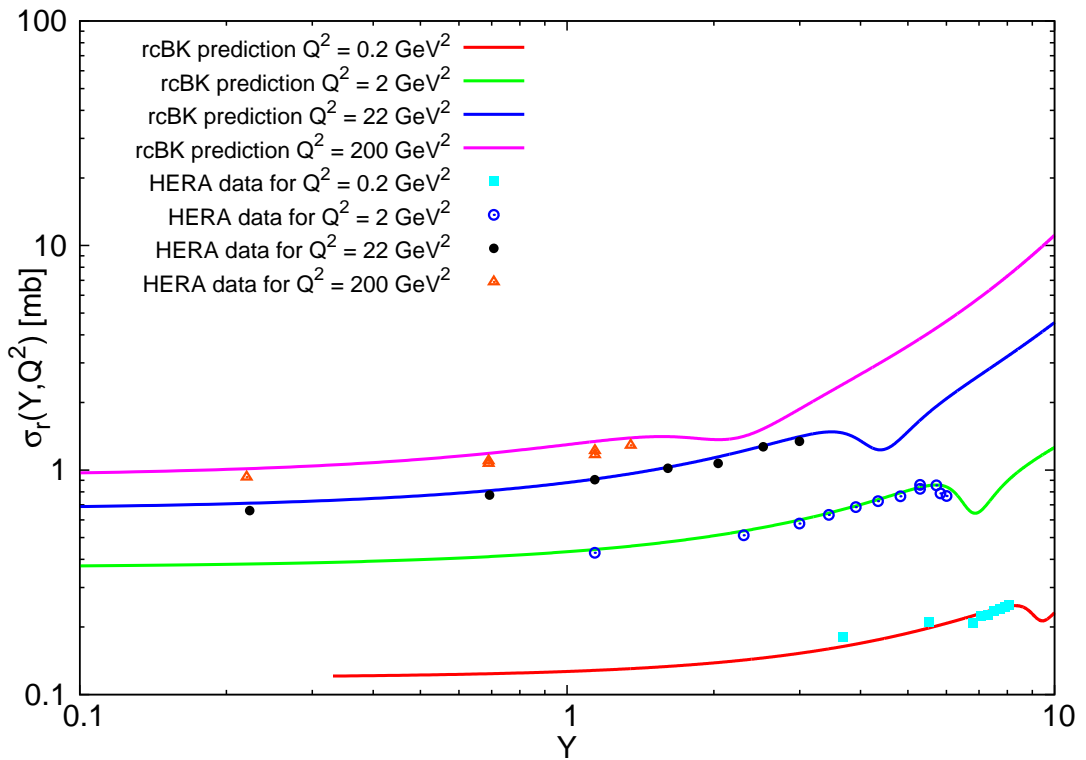


Figure 4.5: The dependence of the reduced cross section $\sigma_r(Y, Q^2)$ on Y compared with data [70].

4.3 Geometric scaled solutions

In this section, I will discuss the process of finding a geometrically scaled initial condition. First, we took the MV initial condition with parameters described in previous sections and ran the evolution to $Y = 100$. For larger values of rapidity, the solution does not change its shape with further evolution, but just shifts along the r -axis. By the rapidity of $Y = 100$, we assumed that the evolution already forgot the MV initial condition since as was shown in the previous section, even dramatically different initial conditions converge to the usual shape by the rapidity of 8. This scaled solution was then taken and re-scaled to higher values of r to obtain a new initial condition that would be more physical and require less parameters that need to be fitted from data.

In the re-scaling process, we had to come up with a parameter, that would characterize the amount of shift in the values of r . This parameter is called Q_{s0}^2 and it determines the amount of shift according to the equation by the relations

$$Q_{s0} = 1/r_0 \quad (4.1)$$

and

$$N(r_0) = 0.5. \quad (4.2)$$

The initially considered value was $Q_{s0}^2 = 0.07 \text{ GeV}^2$ which was later varied. For this re-scaled initial condition, we ran the evolution again to $Y = 10$ to get the observable values that can be compared to the data measured at HERA.

Figure 4.6 compares the geometrical scaled initial condition to the MV initial condition. We can see that the geometric scaled initial condition is different to the MV initial condition that was obtained by fitting the data in the range that is of the most importance.

Since we now used a different initial condition, the previously used value of σ_0 which parametrizes the integral over b in the approximation of a trivial black disc b -dependence might have a completely different value and needs to be fitted from data again. To obtain this fit, we computed the values of F_2^{Data}/F_2^{Theory} for values of Q^2 varying from 0.2 to 150 GeV^2 (see Fig. 4.7). For each value of Q^2 , we fitted the ratio of structure functions with a constant to determine the correction factor for the previously used value of σ_0 .

This ratio then showed a nontrivial Q^2 dependence. Its value obtained from the constant fit was decreasing in a logarithmic-like decrease see Fig. 4.9. We then varied the initial re-scaling parameter Q_{s0}^2 from the values of 0.03 to 0.13 GeV^2 to determine the dependence of this logarithmic decrease on the shift of the initial condition. The results for the values of $Q_{s0}^2 = 0.04, 0.07, 0.10$ and 0.13 GeV^2 are shown in Fig. 4.8, 4.9, 4.10 and 4.11 respectively. As we can see, the slope of the logarithmic decrease remains the same, only a constant shift towards the lower values of the ratio is observed, when we go to higher values of Q_{s0}^2 .

Of course in this approach, we assumed that there is no dependence of the ratio F_2^{Data}/F_2^{Theory} on rapidity. In other words, that the geometrical scaled initial condi-

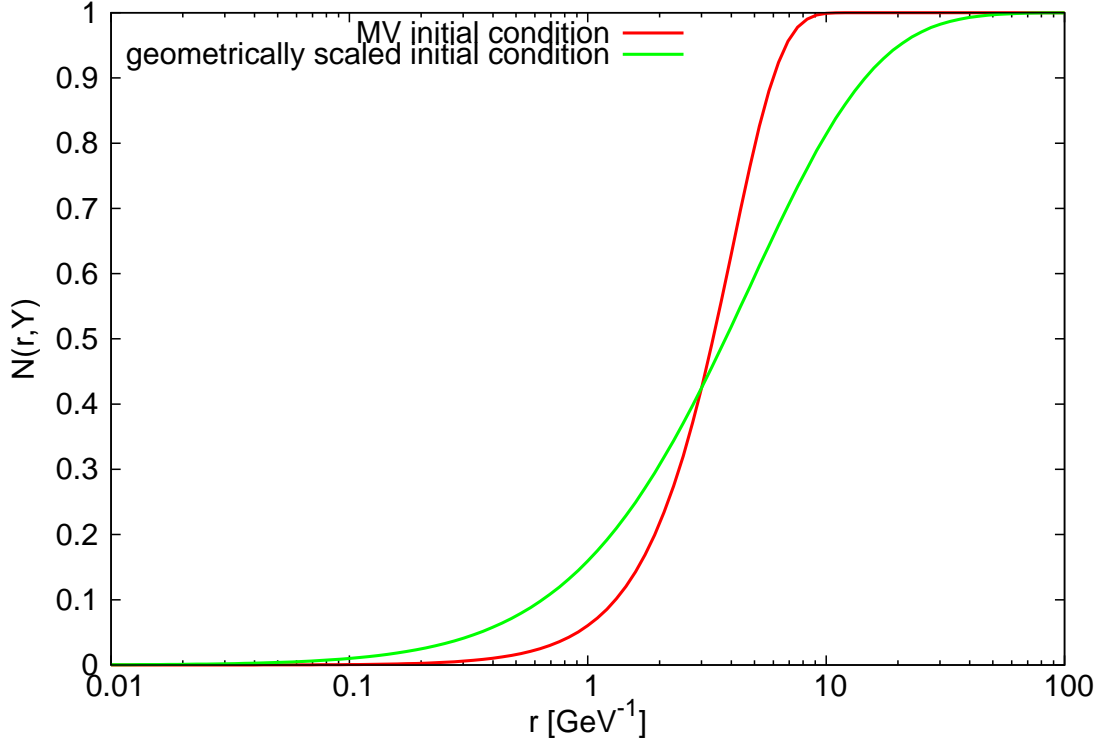


Figure 4.6: MV initial condition and geometrically scaled initial condition with $Q_{s0}^2 = 0.07 \text{ GeV}^2$.

tion predicts the measured values of the structure function correctly and that there are no other effects to be accounted for except for the normalization of the integral over the impact parameter. Therefore next, we focused on determining quantitatively the quality of the fits of F_2^{Data}/F_2^{Theory} . To determine this "validity" of the fit, we used the value of χ^2 which is defined by the following expression

$$\chi^2 = \frac{1}{ndf} \sum_i \frac{(X_i - f(X_i))^2}{\sigma_i^2}, \quad (4.3)$$

where X_i are the measured values and $f(X_i)$ is the value of our fit for the data point X_i . Here σ_i represents the error corresponding to the measured value X_i and ndf stands for the number of degrees of freedom of the fit. The value of χ^2 should be about one for a good fit. If the value is too big, it means that the experimental values are off the describing function and the fit might be incorrect. If the values of χ^2 are too small, it can mean that the errors of the measurement are in fact much smaller than the values used in the computation. The error that we used for our computation was

$$\sigma_i = Er_i\% \frac{F_2^{Data}}{F_2^{Theory}} \cdot 0.01, \quad (4.4)$$

where $Er_i\%$ is the error of the HERA data point i in percent. The values of χ^2 for the values of $Q_{s0}^2 = 0.04, 0.07, 0.10$ and 0.13 GeV^2 are shown in Fig. 4.12, 4.13, 4.14 and 4.15 respectively.

The fits F_2^{Data}/F_2^{Theory} exhibit rather large values of χ^2 for all possible setups of Q_{s0}^2 . If we go towards lower values of Q_{s0}^2 (at about 0.04 GeV^2), the fits get better in the region of high Q^2 - above $Q^2 = 30 \text{ GeV}^2$, but reach higher values of χ^2 for fits with lower values of Q^2 . On the other hand, if we set Q_{s0}^2 to higher values (at about 0.13 GeV^2), the fits get worse in the region of high Q^2 , but better in its lower values see Fig.4.12, 4.13, 4.14 and 4.15. The studied χ^2 values for the re-scaling parameter spanning from $Q_{s0}^2 = 0.03 \text{ GeV}^2$ to 0.13 GeV^2 lead us to the conclusion that the optimal value lies around the value of 0.07 GeV^2 , where the lower values of Q^2 still exhibit reasonable values of χ^2 and the peak forming at higher values does not grow too much to start influencing the values of Q^2 in its proximity.

Even the fits in this region are not perfect constants and the values of F_2^{Data}/F_2^{Theory} show a slight dependence on rapidity. The dependence of the ratios proves to be slightly linearly growing with increasing rapidity, and it may tell us that there are some effects that were not yet accounted for in this approach. This slight growing tendency of the ratios with higher rapidity values is distorting the fits and therefore increasing the resulting value of χ^2 . The fact that a small variation from the constant behavior can produce high values of χ^2 is given by the decreasing trend of the errorbar value of the measured data from HERA at higher values of Q^2 . As was shown, this behavior cannot be easily singled out by another choice of the re-scaling parameter Q_{s0}^2 .

Of course since the evolution is carried out to such high values of rapidity, more error would come from the numerical implementation of the equation (rounding errors, repeated linear interpolation and extrapolation etc.). In order to determine whether the evolution itself can introduce errors that would change the behavior of the scaled initial condition, we took the already scaled initial condition and ran it to $Y = 100$ again. Then we re-scaled it back to the initial position and analyzed its properties in the same manner as was described above for the once-scaled initial condition. The initial condition scaled after running to $Y = 200$ exhibits the same behavior as the initial condition scaled at $Y = 100$. It gives the same logarithmic decrease in the structure function ratio with respect to Q^2 and the χ^2 plots for various values of Q_{s0}^2 are almost identical. The only difference is a slight constant shift of about 0.06 towards lower values of the fit of the structure function ratio which is due to rounding errors and inaccurate interpolations within the computation. It gives us an information on the inaccuracies that are introduced to the solution by computing it up to the rapidity of $Y = 100$.

In order to determine whether this scaled initial condition is of a more physical nature than the initial condition obtained by fitting the data, a prediction of the observables has been made. In Figures 4.16 and 4.17, we can see structure functions computed with both the scaled initial condition and the MV initial condition. The correction factor for σ_0 has been incorporated into the structure function computation for the geometrical scaled case. In these figures we can see the structure function for $Q^2 = 0.25$ and 22 GeV^2 and we can see that they differ in the regions where data has not yet been measured. A future measurement, possibly at the LHC, can determine the validity of this approach to the dipole model and the rcBK evolution equation in particular.

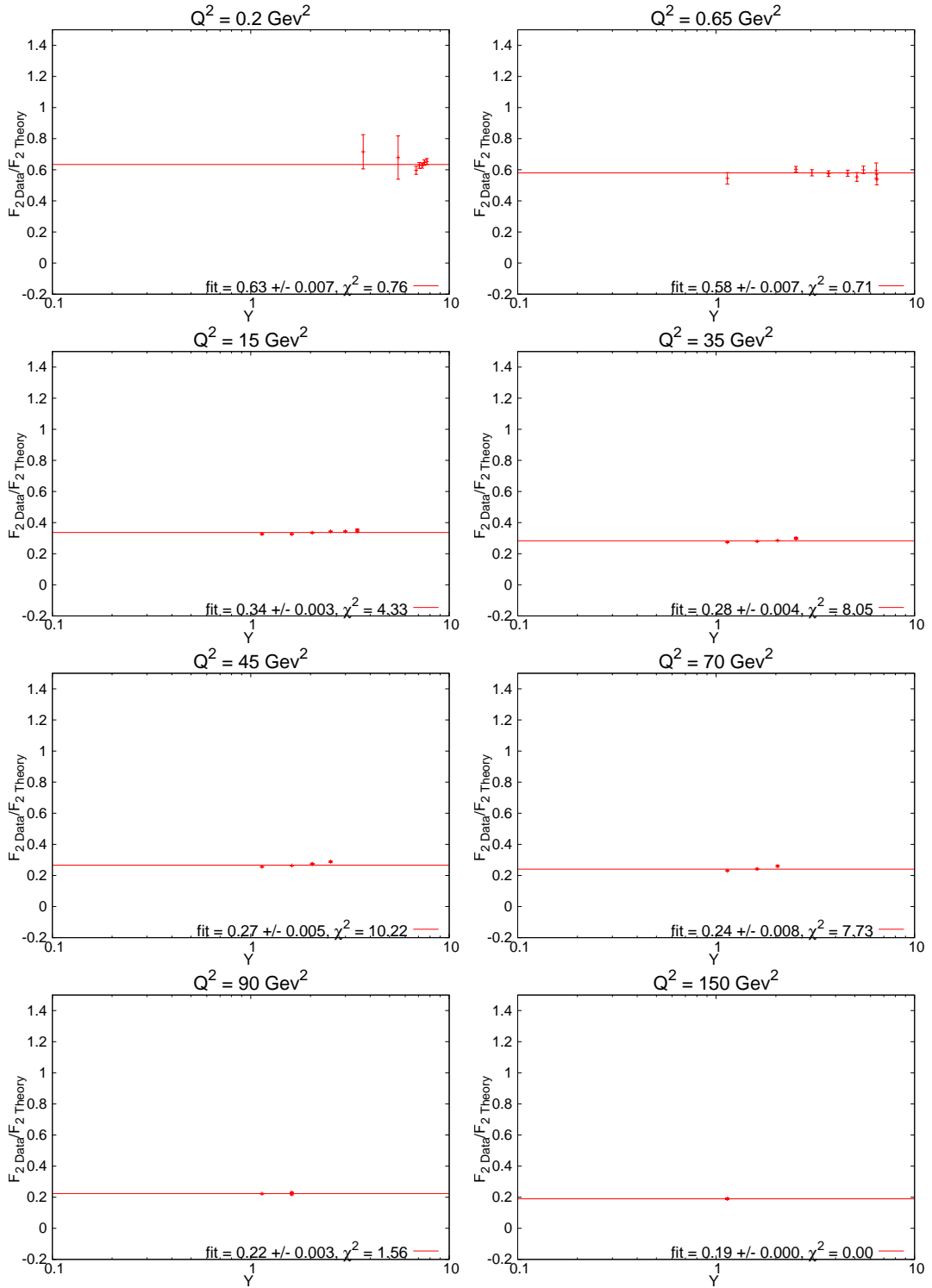


Figure 4.7: The values of F_2^{Data}/F_2^{Theory} for the values of $Q^2 = 0.2, 0.65, 10, 15, 35, 45, 70, 90$ and 150 GeV^2 for $Q_{s0}^2 = 0.07 \text{ GeV}^2$.

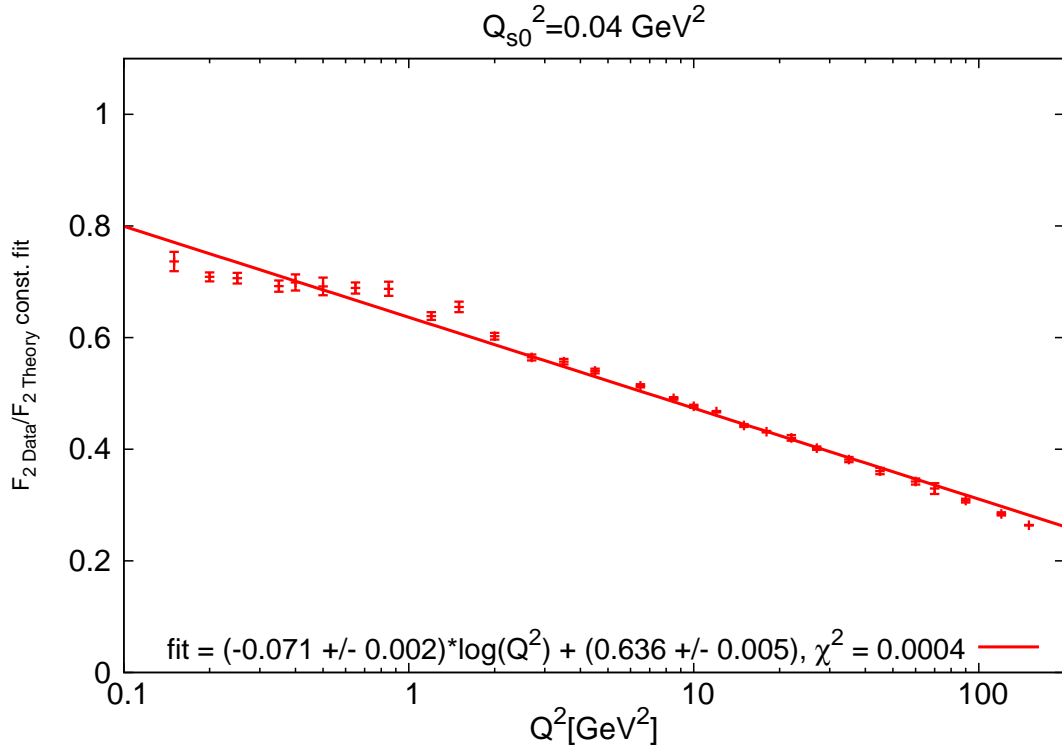


Figure 4.8: The values of fitted F_2^{Data}/F_2^{Theory} with a constant for all Q^2 for $Q_{s0}^2 = 0.04 \text{ GeV}^2$.

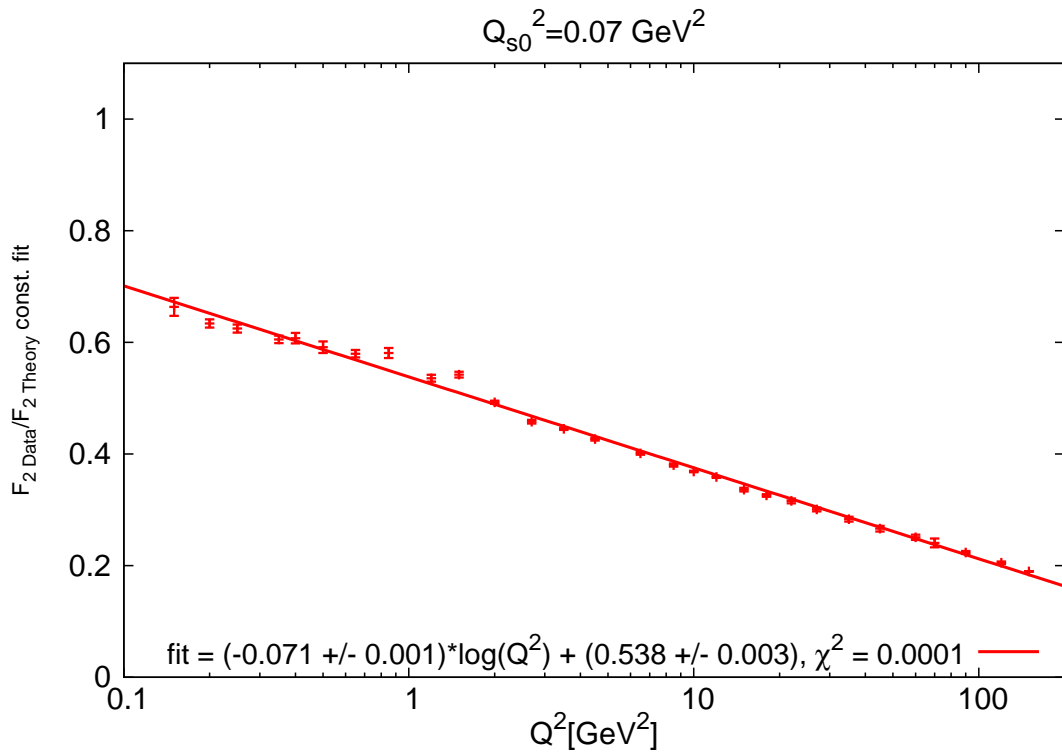


Figure 4.9: The values of fitted F_2^{Data}/F_2^{Theory} with a constant for all Q^2 for $Q_{s0}^2 = 0.07 \text{ GeV}^2$.

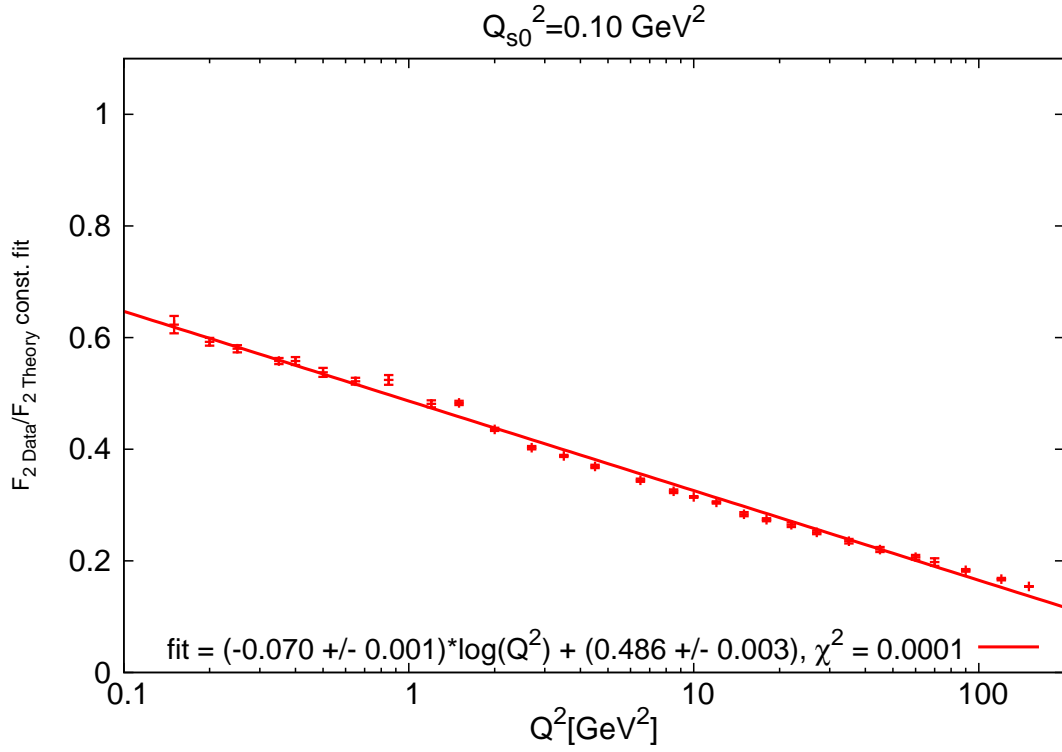


Figure 4.10: The values of fitted F_2^{Data}/F_2^{Theory} with a constant for all Q^2 for $Q_{s0}^2 = 0.10 \text{ GeV}^2$.

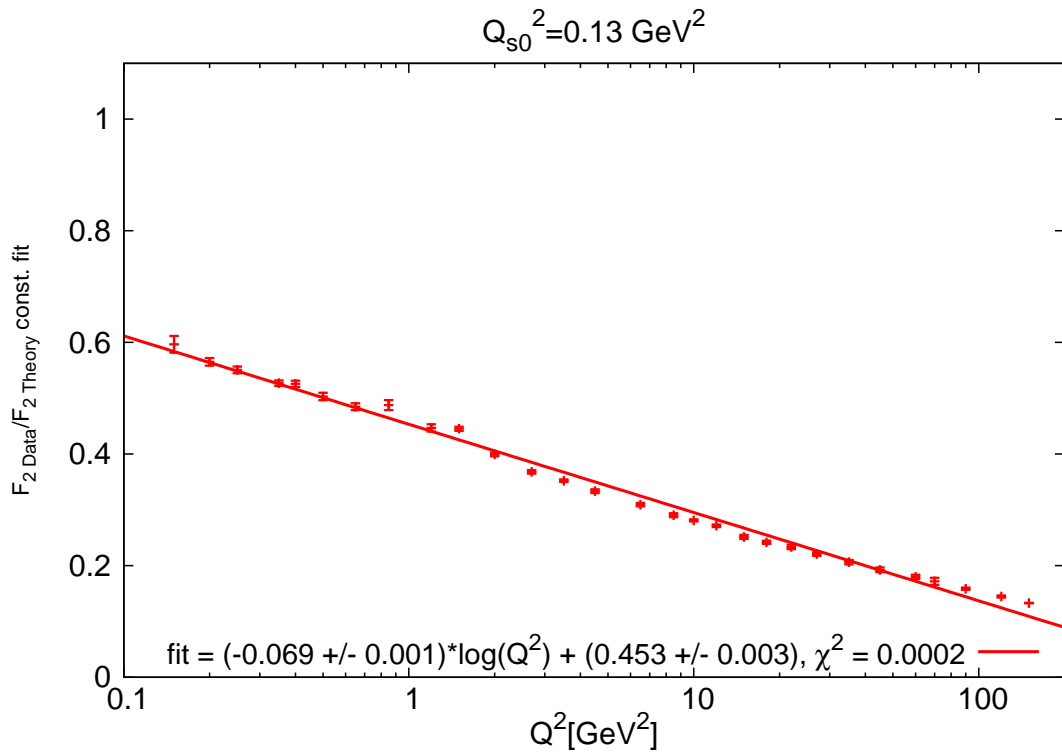


Figure 4.11: The values of fitted F_2^{Data}/F_2^{Theory} with a constant for all Q^2 for $Q_{s0}^2 = 0.13 \text{ GeV}^2$.

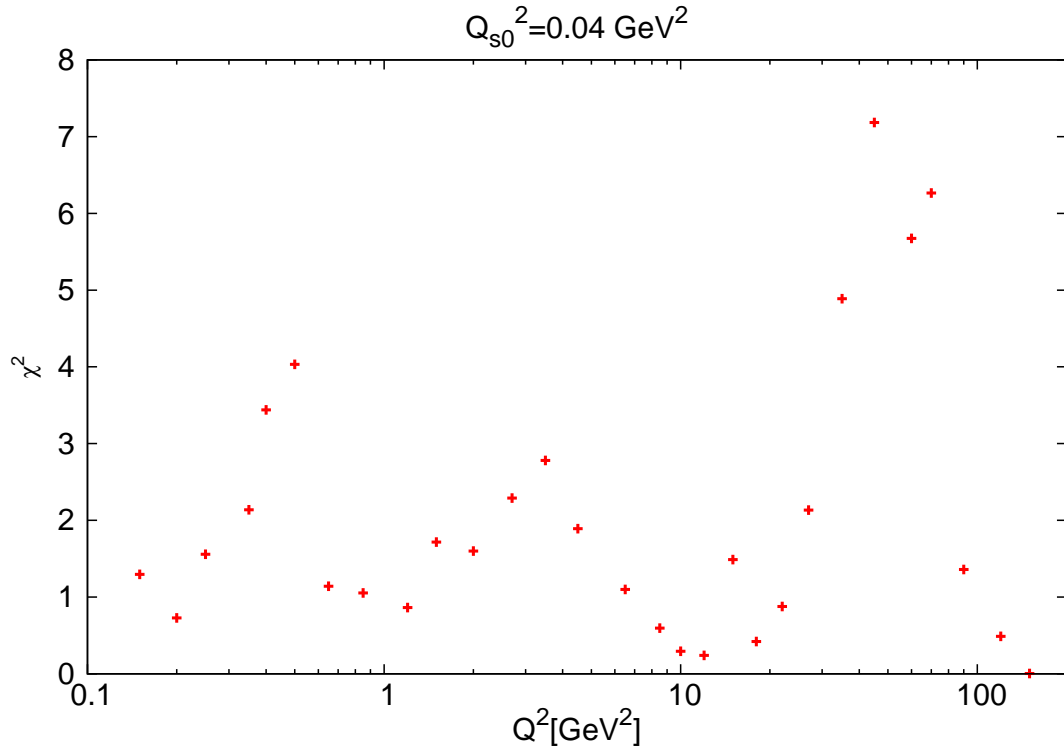


Figure 4.12: The values of χ^2 for all Q^2 for $Q_{s0}^2 = 0.04 \text{ GeV}^2$.

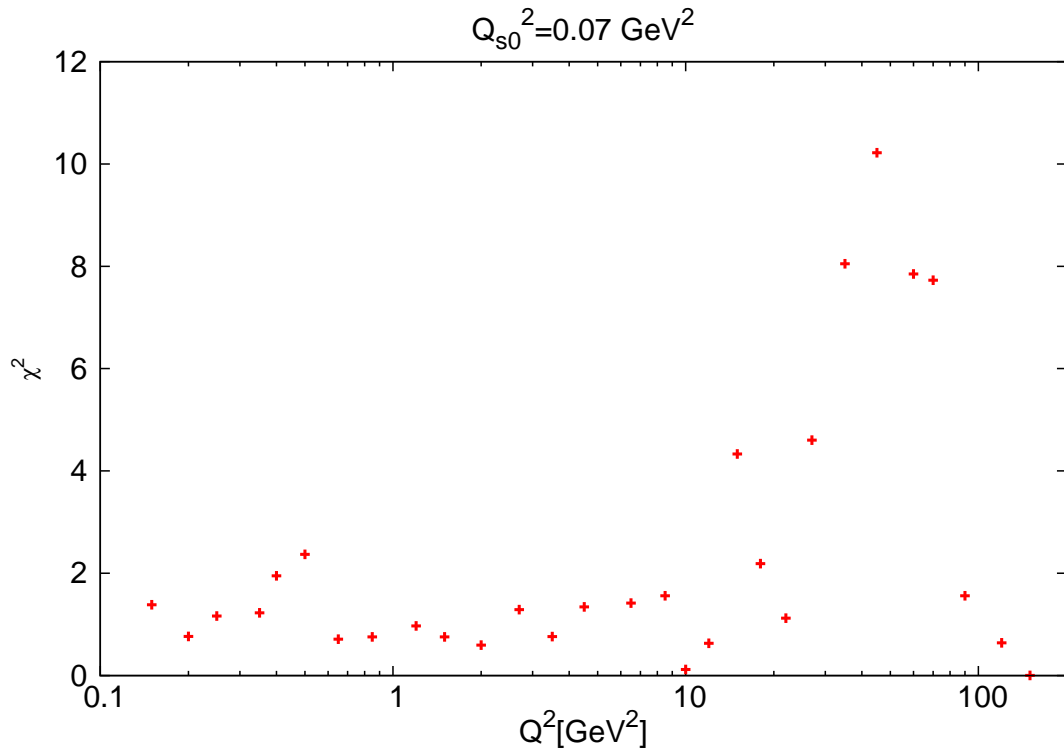


Figure 4.13: The values of χ^2 for all Q^2 for $Q_{s0}^2 = 0.07 \text{ GeV}^2$.

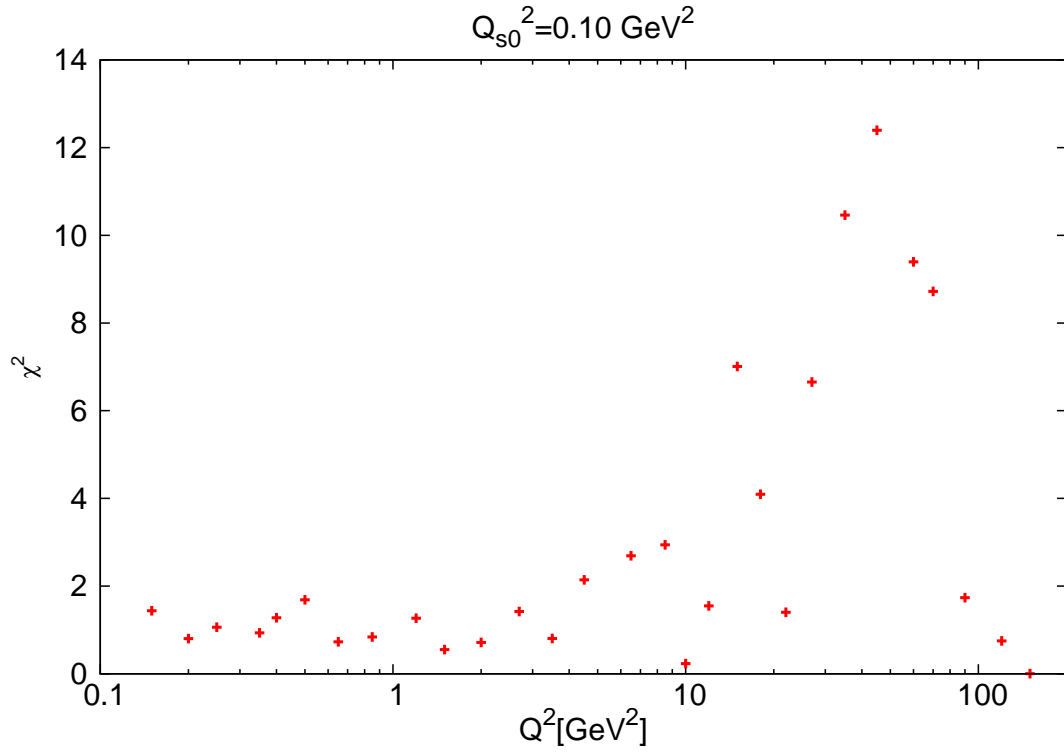


Figure 4.14: The values of χ^2 for all Q^2 for $Q_{s0}^2 = 0.10 \text{ GeV}^2$.

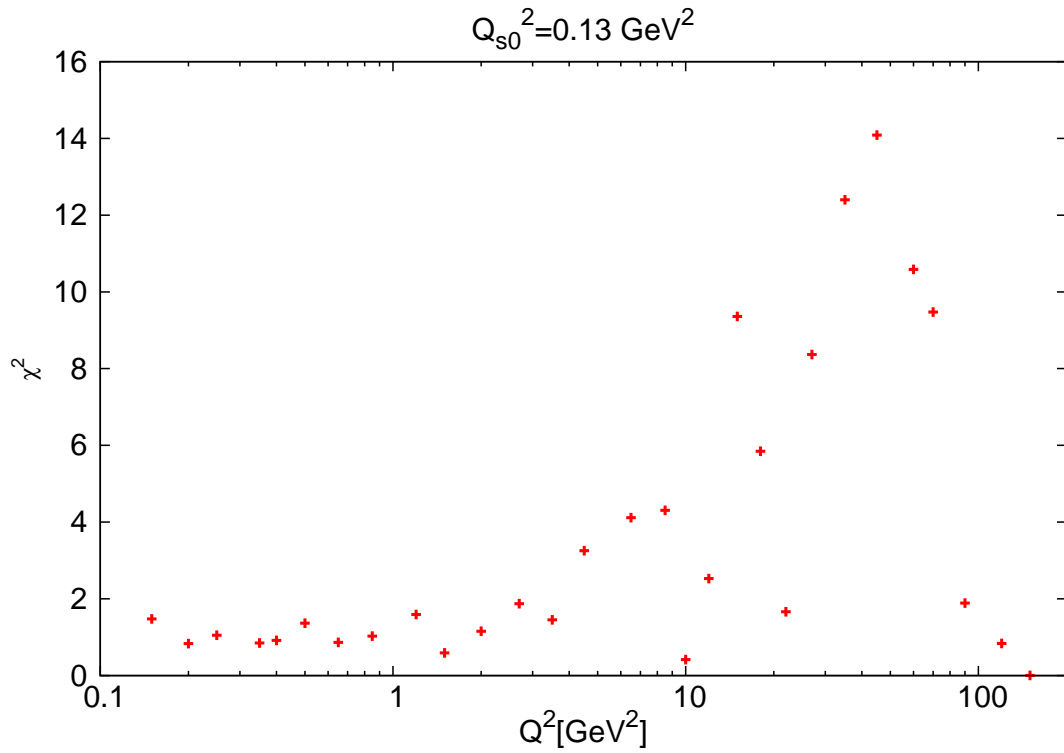


Figure 4.15: The values of χ^2 for all Q^2 for $Q_{s0}^2 = 0.13 \text{ GeV}^2$.

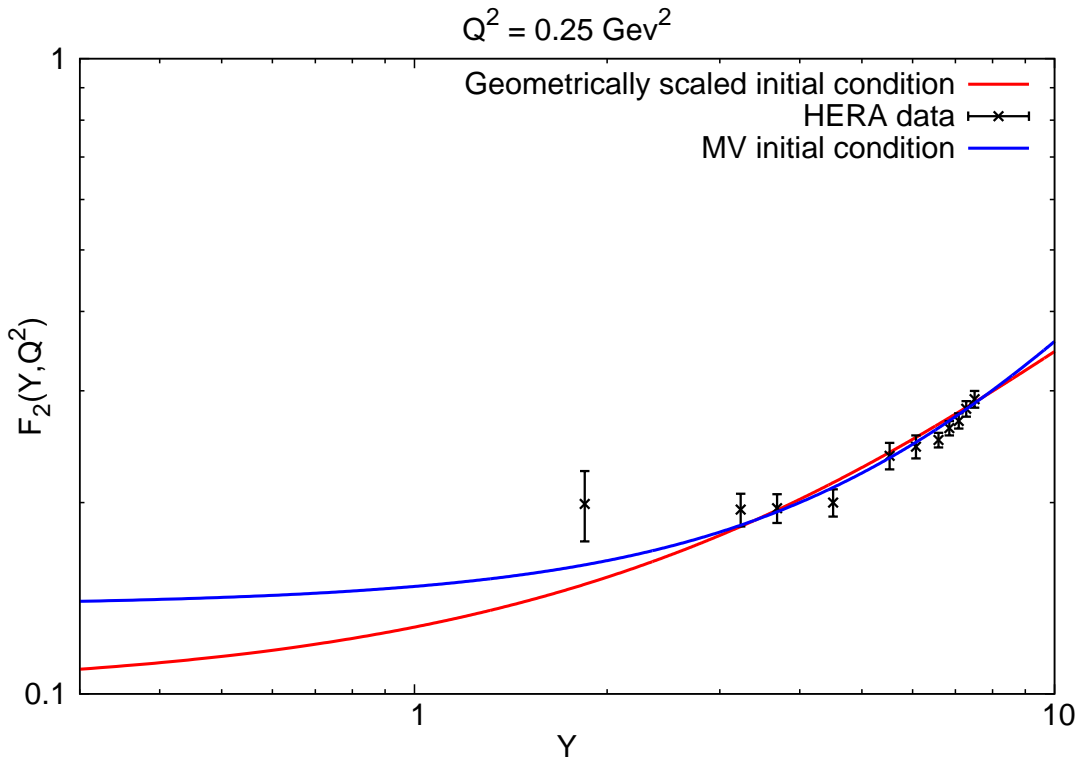


Figure 4.16: The values F_2 for both the MV initial condition [21] and the geometric scaled initial condition obtained with $Q_{s0}^2 = 0.07 \text{ GeV}^2$. $Q^2=0.25 \text{ GeV}^2$.

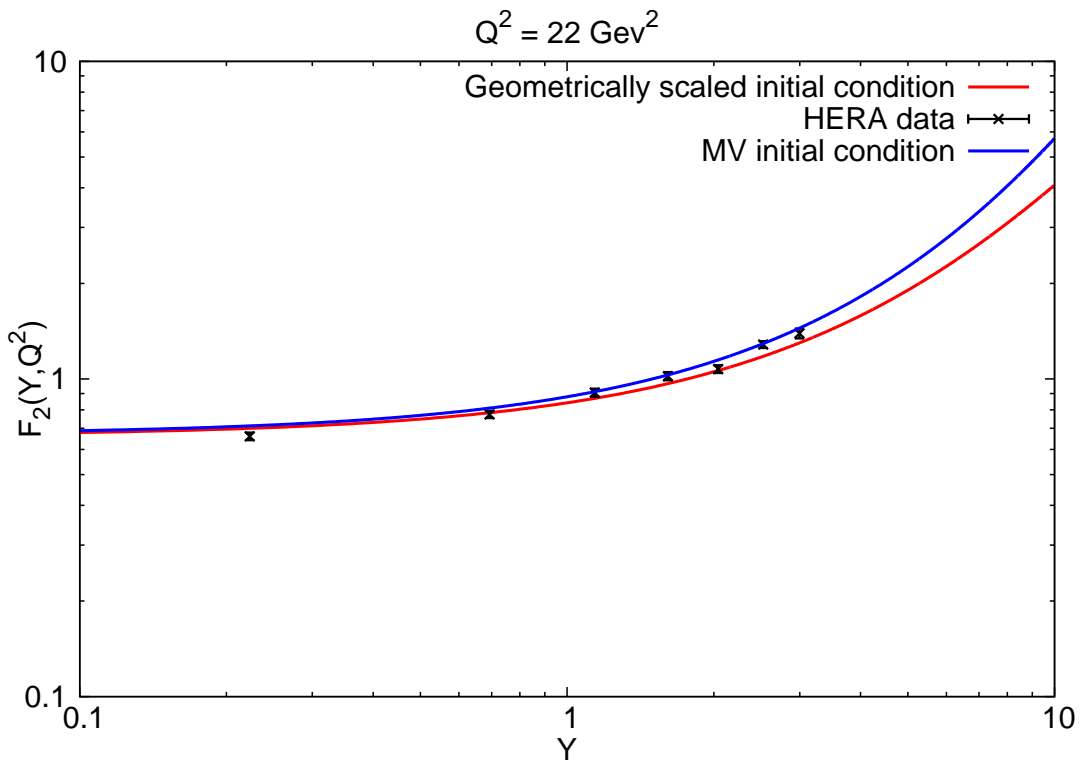


Figure 4.17: The values F_2 for both the MV initial condition [21] and the geometric scaled initial condition obtained with $Q_{s0}^2 = 0.07 \text{ GeV}^2$. $Q^2=22 \text{ GeV}^2$.

4.4 Impact parameter dependent rcBK solutions

The solution to the running coupling Balitsky-Kovchegov evolution equation with the b-dependent approach is shown in the following figures.

For the b-dependent BK equation, a step of 0.1 in rapidity was used, Simpson's method for the integration over r and b was used with 25 steps per order of magnitude in both dipole distance and impact parameter. The grid sizes were chosen to be the same for these two variables, and the considered interval was $[10^{-7}, 10^2] \text{ GeV}^{-1}$. There were 20 steps per interval of $[0, 2\pi]$ in the integration over θ_{rr_1} .

We derived the Runge-Kutta method for the b-dependent rcBK equation in order to determine its validity for this approach as well as to simplify the general Runge-Kutta computation. This derivation is summed up in the Appendix A, Runge-Kutta method for the impact parameter dependent rcBK equation derivation.

We have to introduce a cutoff to the initial condition in a similar manner as we did for the impact parameter dependent rcBK equation in Section 3.3. If we set the cutoff as $\theta(\frac{1}{m} - r)$ just as for the b-dependent version of kernel, the initial condition does not fully cover the area of the evolution. That is because we fix the maximal length of the vectors r_1 and r_2 to $\frac{1}{m}$ but since $\vec{r} = \vec{r}_1 + \vec{r}_2$, the evolution then runs for the values of r lower than $\frac{2}{m}$. In other words, the cutoff imposed by the so called gluon mass m is restricting solely the daughter dipoles r_1 and r_2 . The mother dipole consisting of these dipoles can therefore reach sizes twice as high as the cutoff limit. The solutions for the initial condition fixed with $\theta(\frac{1}{m} - r)$ are shown in Fig. 4.18 and 4.19 for the values of $b = 1$ and $b = 5$ respectively. Fig. 4.20 shows this solution integrated over b for various values of rapidity according to

$$N(r, Y, \cos(\theta_{rb})) = \int N(r, b, Y) b db \quad (4.5)$$

The solutions obtained with the initial condition constrained with $\theta(\frac{2}{m} - r)$, that was set so that it would cover the whole interval on which the evolution is carried out, are shown in Fig. 4.21 and 4.22 for two values of impact parameter. The integrated solution of such initial condition is shown in Fig. 4.23. For these solutions we assumed the value of $\theta_{rb} = \frac{\pi}{2}$, which means that the mother dipole orientation is perpendicular to the impact parameter vector.

The initial condition used for these computations is shown in Eq. 3.17 with parameters $c = 0.0643$ and $d = \frac{1}{8}$.

Figures 4.27 and 4.28 show the scattering amplitude as a function of dipole distance and impact parameter at the same time. Fig. 4.27 shows the initial condition that was used for the computation and Fig. 4.28 shows the scattering amplitude at rapidity of $Y = 10$. We can see that both the initial condition and the scattering amplitude at rapidity of $Y = 10$ steeply fall after reaching certain value of impact parameter (at about 10 GeV^{-1}). For values of impact parameter lower than this, the scattering amplitude is more or less unchanged. If we take a look at the dipole distance axis, we can see that the evolution here raises the front of the scattering amplitude in a similar manner as in the impact parameter independent case. The scattering amplitude however rapidly falls after reaching the cutoff value of $r = \frac{2}{m}$.

We can see that unlike the unintegrated scattering amplitude, the integrated scattering amplitude 4.20 and 4.23, can exceed the value of one on part of the considered interval. In the b -independent approach where the scattering amplitude $N(r, Y)$ never exceeded this value, we multiplied the scattering amplitude by the constant σ_0 which comes from the integration of a b -profile given by the Heavyside function.

$$\int d\vec{b}N(r, Y, \vec{b}). \quad (4.6)$$

The value of the parameter σ_0 was set to the value of 32.895 mb, so the integrated scattering amplitude $N(r, Y)$ also reached values that were higher on most of the considered interval.

The fact that the integrated scattering amplitude shows similar geometric behavior to the unintegrated one at low values of the impact parameter is a result of the unchanging shape of the scattering amplitude for most of the values of b . When the integration is carried out, these parts dominate the integral and its shape is therefore similar. The parts in which the exponential suppression of the scattering amplitude comes into effect (at higher values of impact parameter) do not contribute as much to the resulting function.

The dependence of the scattering amplitude evolution on the angle between the dipole distance vector and the impact parameter vector was also studied. We have shown that the effects of this angular variation on the resulting function are small. In Fig. 4.24 and 4.25, the scattering amplitude was calculated with $\theta_{rb} = 0$, which corresponds to the color dipole being aligned parallel to the impact parameter vector. We can compare these figures to the ones obtained with $\theta_{rb} = \frac{\pi}{2}$ 4.21 and 4.22. The difference between these plots is almost negligible, even though we can see a few minor differences in the curve of the scattering amplitude's peak. The dependence of the angle θ_{rb} on the scattering amplitude was tested for 8 different values and they all exhibit similar behavior. Fig. 4.26 shows the ratio of scattering amplitudes $N(Y, r, \cos(\theta_{rb}) = 0)$ and $N(Y, r, \cos(\theta_{rb}) = 1)$. We can see that their difference is well below one percent for most of the considered interval over r .

The fact that the scattering amplitude is almost unchanged for different θ_{rb} setups enables us in the future to restrict ourselves solely to the computation of the integral over the impact parameter size and approximate the integral over this angle as

$$\int d\vec{b}N(r, Y, \vec{b}) = \int bdbd\theta_{rb}N(r, Y, \vec{b}) = 2\pi \int bdbN(r, Y, b). \quad (4.7)$$

This then speeds up the computation dramatically because we no longer have to calculate the evolution for all the θ_{rb} setups but a single value would suffice. The introduction of the impact parameter dependence to the computation then elongates the running time solely by a factor of 225 instead of a factor of 225×20 (for 20 steps in θ_{rb} over $[0, 2\pi]$ and 225 steps in the impact parameter size).

In our approach, we were able to use several methods to significantly decrease the running time (see Appendix A and B as well as section Optimal Setup) of the computation. The computation of the scattering amplitude up to the rapidity of $Y = 10$ takes about 10 hours on a regular personal computer for a fixed θ_{rb} setup in

this approach with the use of the Runge-Kutta method with the step of $\Delta Y = 0.1$ and 25 steps per order of magnitude in both r and b .

The obtained scattering amplitude then describes the strong interaction process within the collision and it can be recomputed into the measured structure function. The computed structure function $F_2(x, Q^2)$ obtained with the use of 4.7 from the impact parameter dependent solution to the rcBK equation is shown in Fig. 4.29.

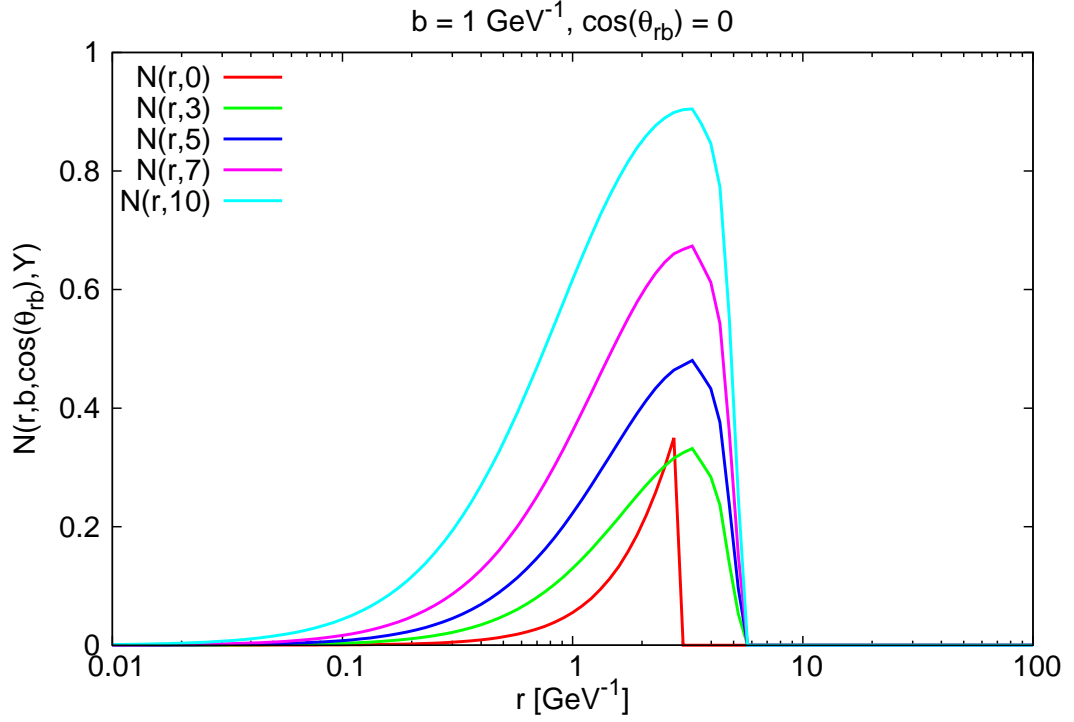


Figure 4.18: The values of $N(Y, r, \vec{b})$ for $b = 1$ and $\theta_{rb} = \frac{\pi}{2}$. The initial condition 3.17 was used and cut in $\frac{1}{m}$. The parameters were set to $c = 0.0643$ and $d = \frac{1}{8}$.

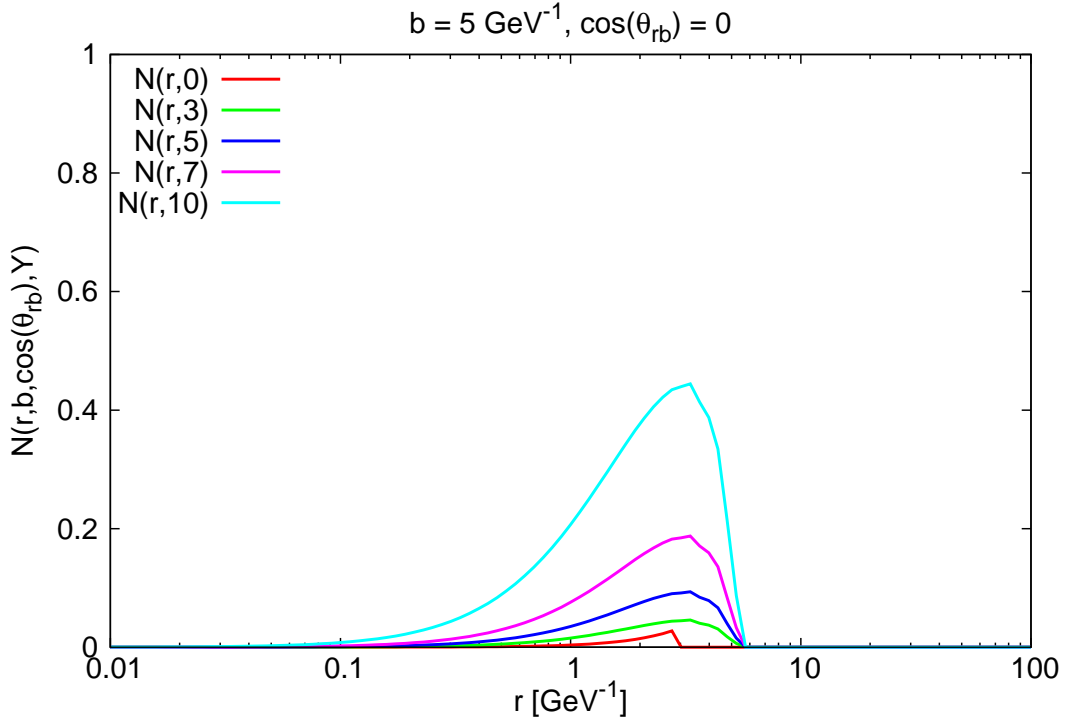


Figure 4.19: The values of $N(Y, r, \vec{b})$ for $b = 5$ and $\theta_{rb} = \frac{\pi}{2}$. The initial condition 3.17 was used and cut in $\frac{1}{m}$. The parameters were set to $c = 0.0643$ and $d = \frac{1}{8}$.

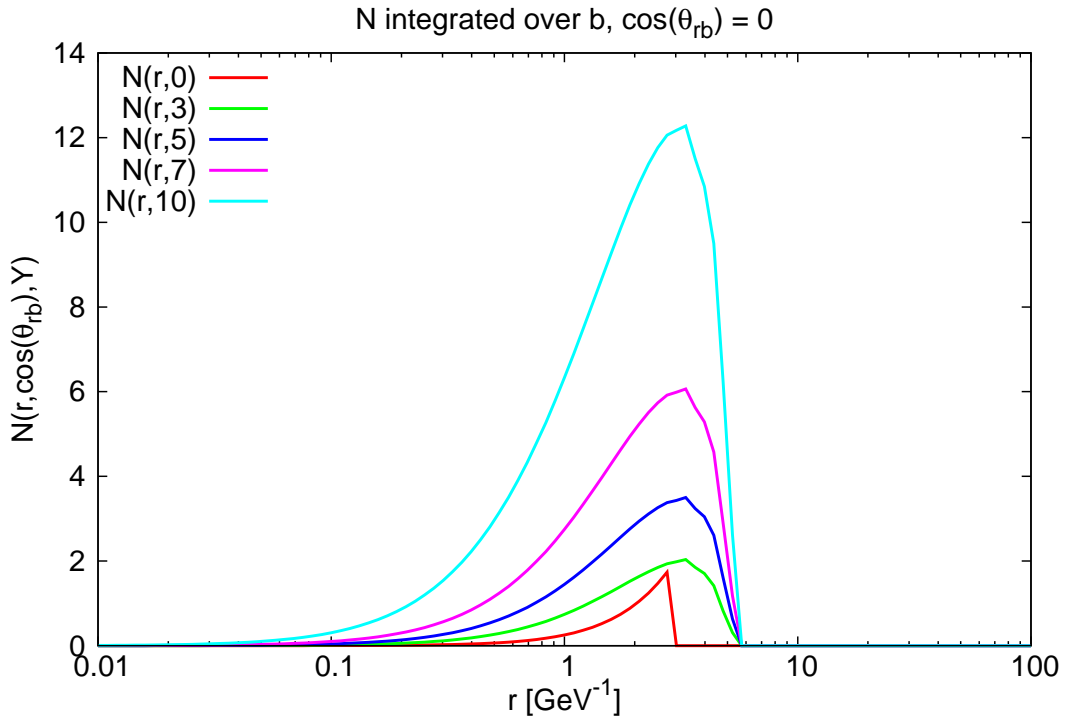


Figure 4.20: The values of $N(Y, r)$ which is $N(Y, r, \vec{b})$ integrated over the impact parameter for $\theta_{rb} = \frac{\pi}{2}$. The initial condition 3.17 was used and cut in $\frac{1}{m}$. The parameters were set to $c = 0.0643$ and $d = \frac{1}{8}$.

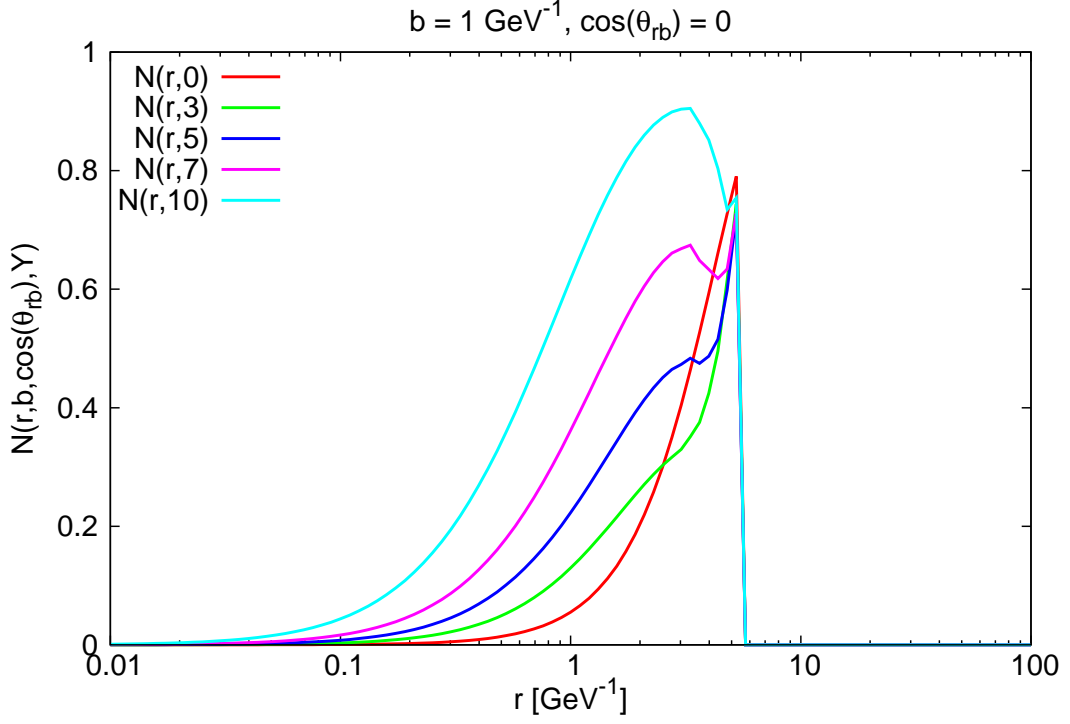


Figure 4.21: The values of $N(Y, r, \vec{b})$ for $b = 1$ and $\theta_{rb} = \frac{\pi}{2}$. The initial condition 3.17 was used and cut in $\frac{2}{m}$. The parameters were set to $c = 0.0643$ and $d = \frac{1}{8}$.

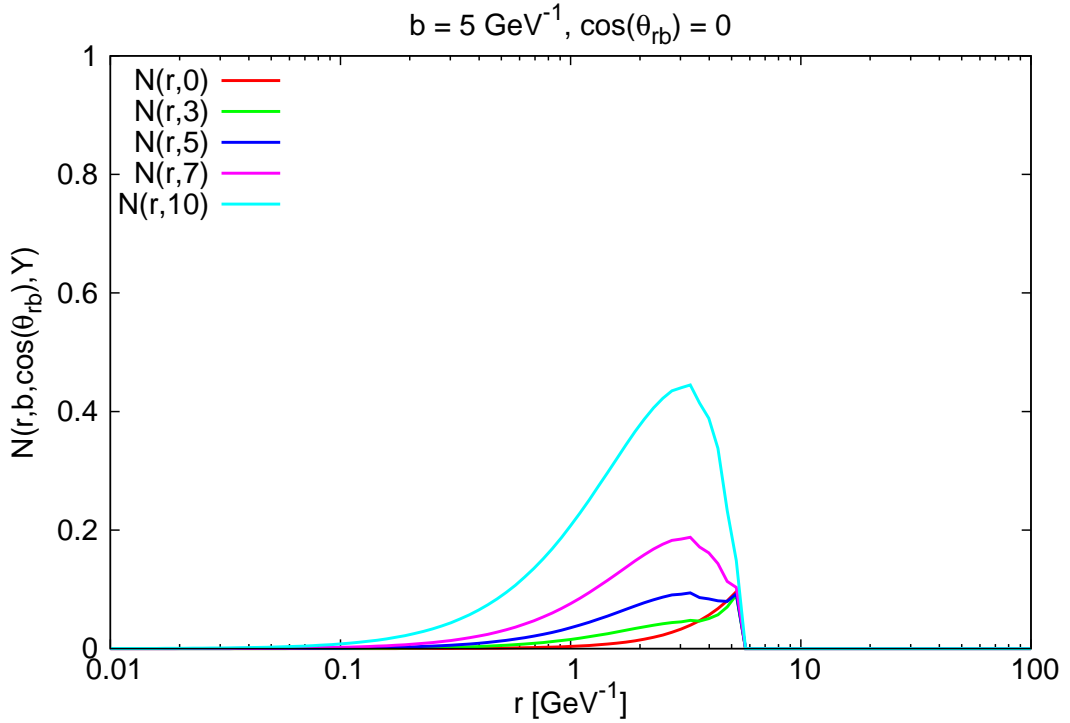


Figure 4.22: The values of $N(Y, r, \vec{b})$ for $b = 5$ and $\theta_{rb} = \frac{\pi}{2}$. The initial condition 3.17 was used and cut in $\frac{2}{m}$. The parameters were set to $c = 0.0643$ and $d = \frac{1}{8}$.

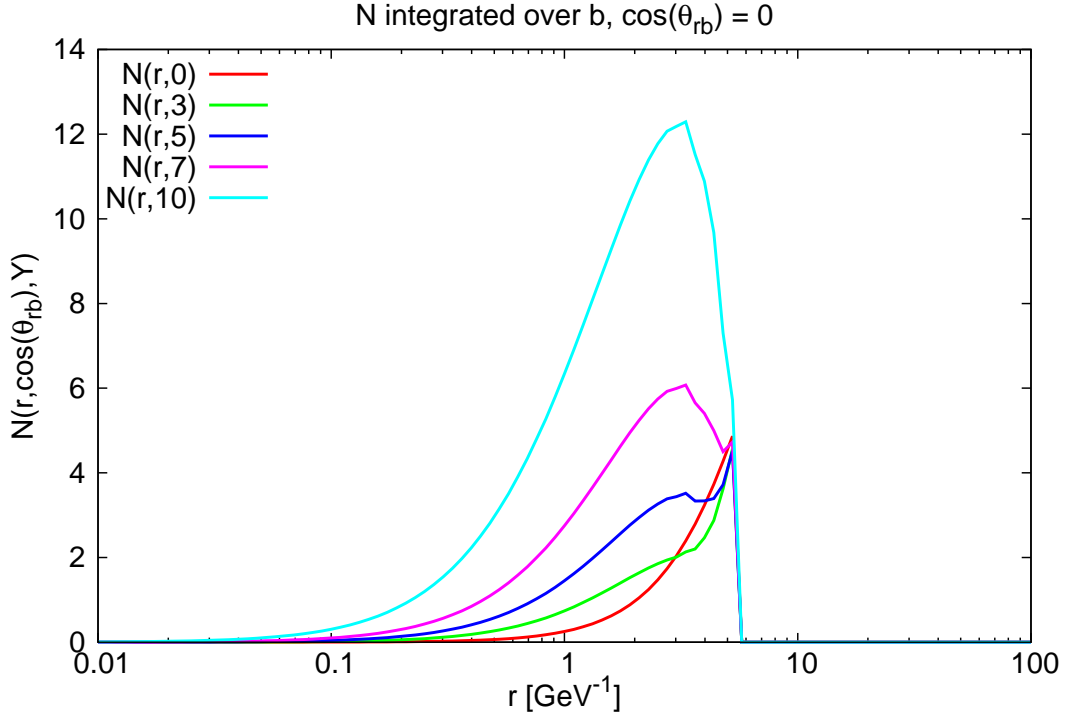


Figure 4.23: The values of $N(Y, r)$ which is $N(Y, r, \vec{b})$ integrated over the impact parameter for $\theta_{rb} = \frac{\pi}{2}$. The initial condition 3.17 was used and cut in $\frac{2}{m}$. The parameters were set to $c = 0.0643$ and $d = \frac{1}{8}$.

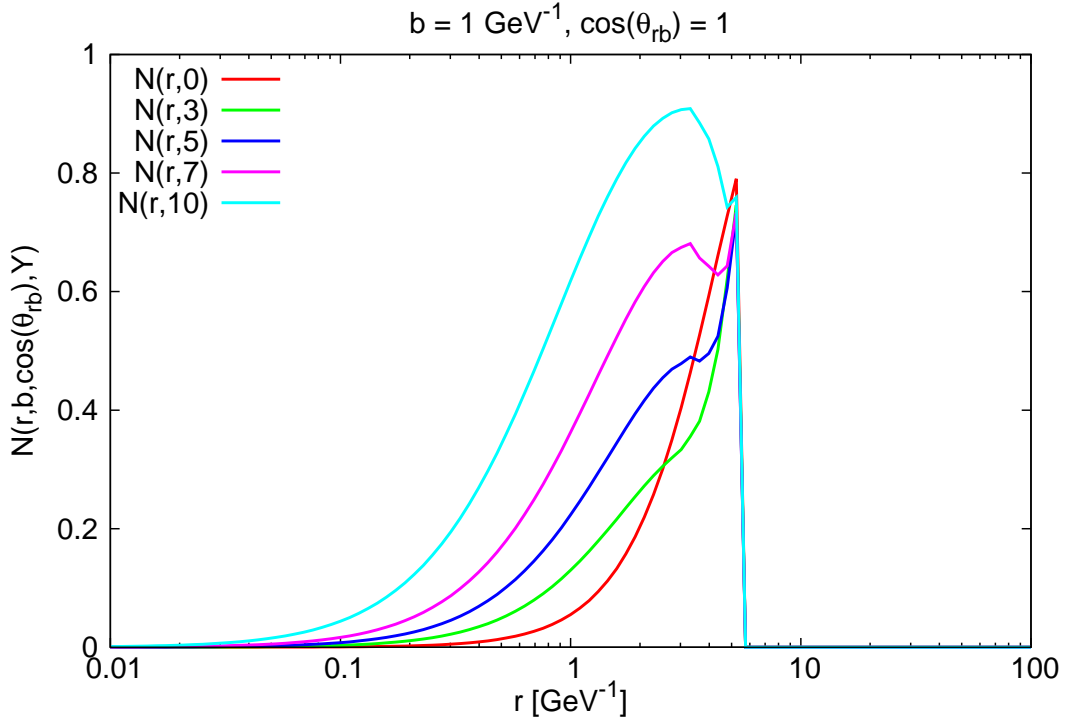


Figure 4.24: The values of $N(Y, r, \vec{b})$ for $b = 1$ and $\theta_{rb} = 0$. The initial condition 3.17 was used and cut in $\frac{2}{m}$. The parameters were set to $c = 0.0643$ and $d = \frac{1}{8}$.

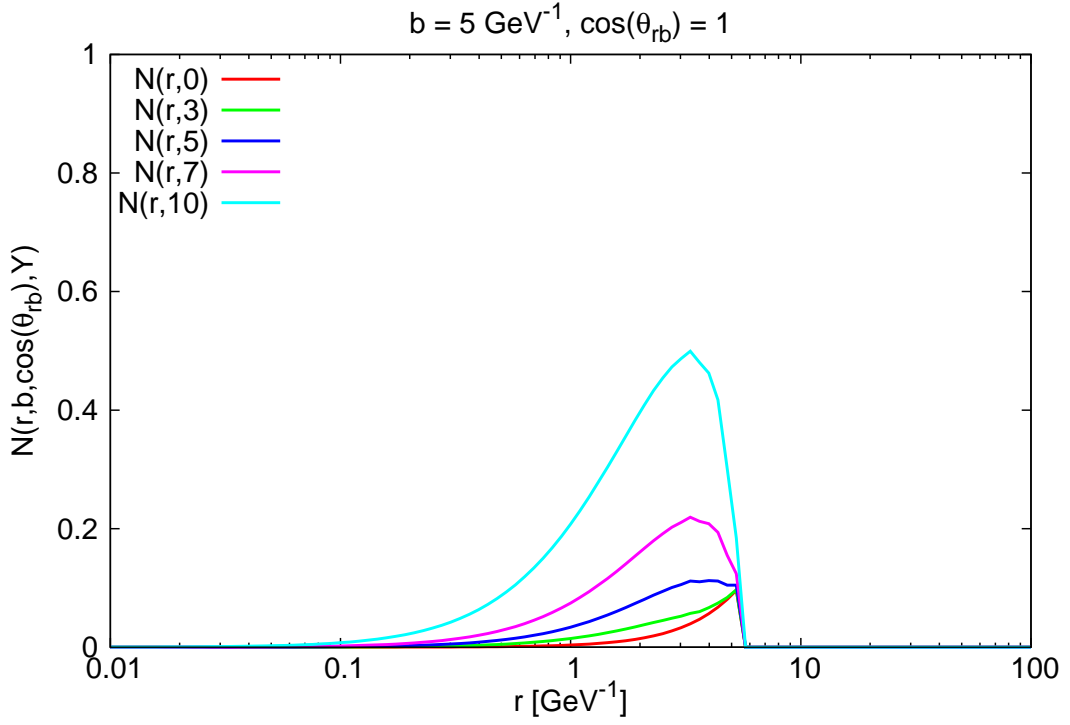


Figure 4.25: The values of $N(Y, r, \vec{b})$ for $b = 5$ and $\theta_{rb} = 0$. The initial condition 3.17 was used and cut in $\frac{2}{m}$. The parameters were set to $c = 0.0643$ and $d = \frac{1}{8}$.

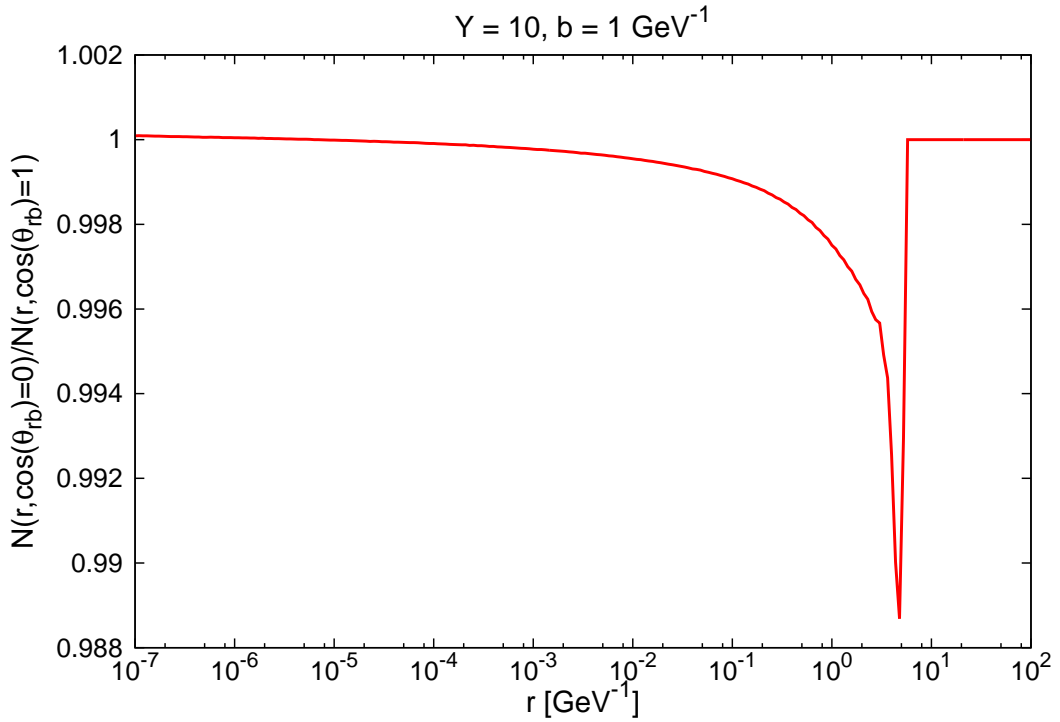


Figure 4.26: The values of $N(Y, r, \cos(\theta_{rb}) = 0)/N(Y, r, \cos(\theta_{rb}) = 1)$ for $b = 1$ and $Y = 10$. The initial condition 3.17 was used and cut in $\frac{2}{m}$. The parameters were set to $c = 0.0643$ and $d = \frac{1}{8}$.

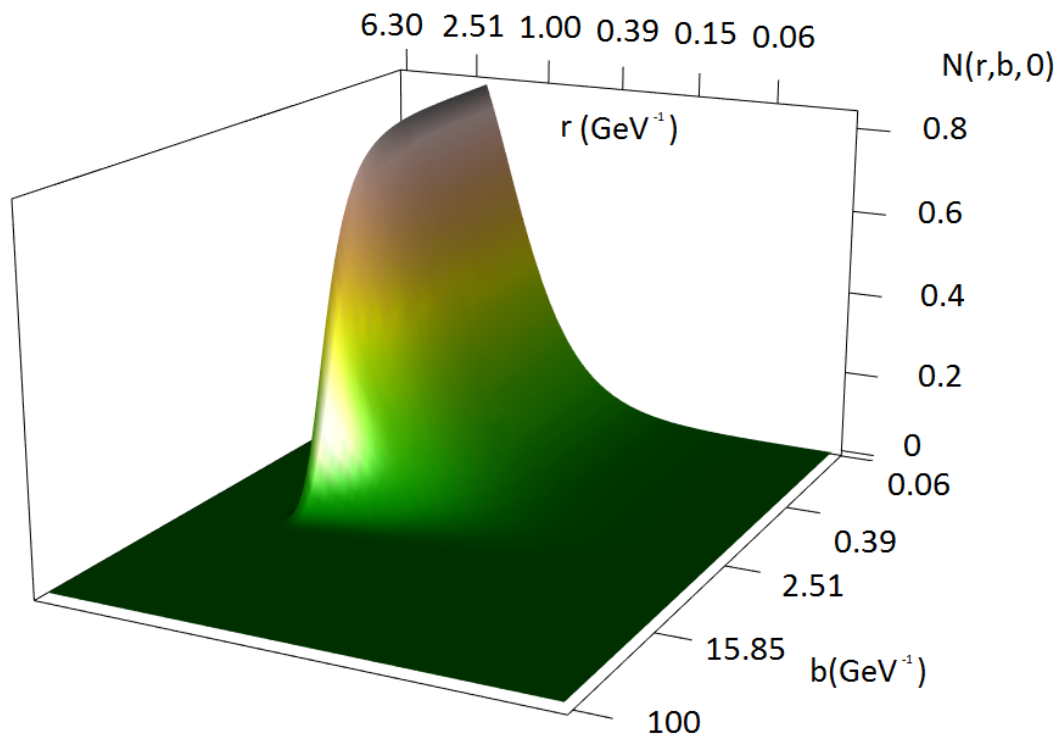


Figure 4.27: 3-D plot of the initial condition of the scattering amplitude with respect to b and r .

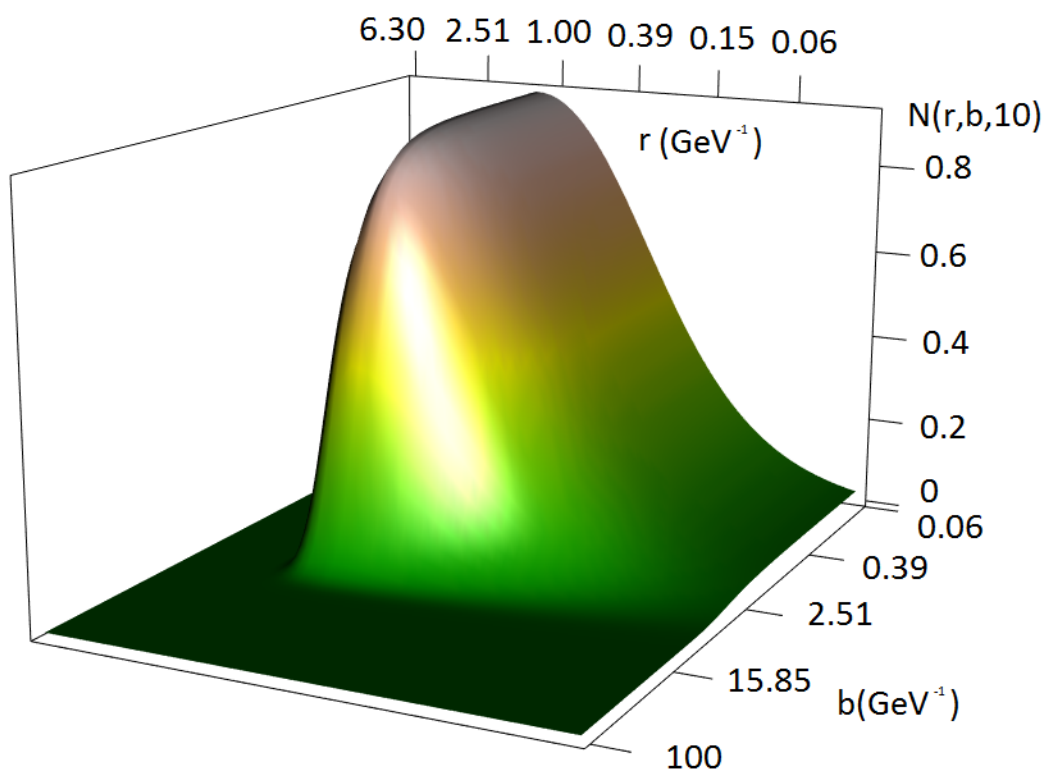


Figure 4.28: 3-D plot of the scattering amplitude with respect to b and r at $Y = 10$.

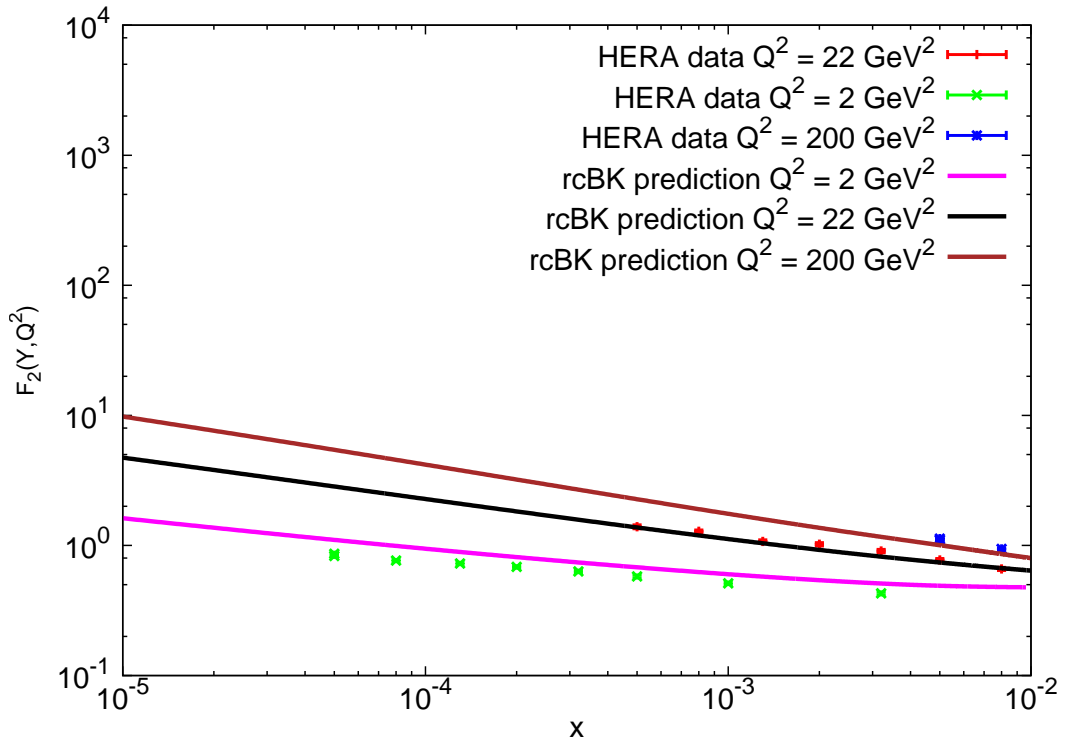


Figure 4.29: The values of $F_2(x, Q^2)$ obtained from the impact parameter dependent solution of rcBK equation. The initial condition 3.17 was used and cut in $\frac{2}{m}$. The parameters were set to $c = 0.0643$ and $d = \frac{1}{8}$.

Conclusion

There are several models that predict the effect of saturation of partons in high energy collisions. The Balitsky Kovchegov evolution equation does that by modifying the BFKL equation with recombination processes that occur in hadrons at high energies. These are expected to be reached in large accelerators such as LHC, HERA or RHIC. The solution to the BK equation including running coupling effects and a b -independent amplitude can predict correctly the values of structure functions of protons or DIS reduced cross section in four orders of Q^2 . It is an integro-differential equation and it typically cannot be solved analytically.

The Balitsky-Kovchegov evolution equation was numerically solved using the Runge-Kutta method of fourth order, Simpson's rule and Lagrange interpolation. Various methods were tested and their initial parameters compared to obtain the best ratio of precision and computing speed since the program for solving the BK evolution equation is time demanding.

The optimal parameters to compute the BK equation for the case without impact parameter dependence prove to be the Runge-Kutta method of fourth order with a step of 0.01 in rapidity, Simpson's rule for the integration with step of 20 over the interval over θ_{rr_1} and 25 steps per order of magnitude of the dipole size r . A simple linear interpolation (in the log-scale) has been determined to give the best results since higher orders are not precise in certain regions and misshape the computed function. For the computation of the photon wave function, 10000 steps per the interval of $[0, 1]$ over the parameter z were chosen. This setup then enables us to compute the structure function up to the rapidity of $Y = 10$ in about 90 seconds on an average personal computer with a mean square error of 1.5 %.

The shape of the photon wave functions was calculated and plotted with various factors that also take part in the final structure function computation. It was shown that the largest numerical contribution to the final value of the cross section and the structure function comes from the dipole size in interval $r \sim (0.1, 30) \text{ GeV}^{-1}$ since the photon wave functions weighted by the solution of the BK evolution equation show negligible values outside this region and thus do not affect the final integral over r as much. The structure function F_2 and reduced cross section $\sigma_{T,L}$ were computed from the obtained solutions given by the rcBK equation for various values of Q^2 and compared to data measured at HERA.

The effect of geometric scaling, which is observed in solutions to the BK equation was also studied. Since the shape of the solutions changes only in the first few units of rapidity and then solely shifts towards lower values of r as the evolution propagated

towards higher values of Y , we were able to establish a new initial condition from the intrinsic properties of the BK equation itself. This geometrical scaled initial condition would then require less parameters that need to be fitted to data than the MV initial condition and could better reflect the physical nature of the system.

The geometrically scaled initial condition was obtained by running the computation up to the rapidity of $Y = 100$ and then re-scaling it back to the initial position. The functionality of this initial condition was then tested and the dependence of the results on the re-scaling parameter was studied. Its initial value was set as $Q_{s0}^2 = 0.07$ and the variation of this parameter later span from $Q_{s0}^2 = 0.03$ to $Q_{s0}^2 = 0.13$.

We searched to obtain a new value for the parameter σ_0 since in this approach, we are using a new initial condition and its value that was obtained in previous fits might not be accurate anymore. For this reason, values of F_2^{Data}/F_2^{Theory} were studied in order to obtain a correction factor for this constant. However the ratio of F_2^{Data}/F_2^{Theory} showed a logarithmically decreasing dependence on Q^2 for all choices of the re-scaling parameter. The slope of this decrease proved to be identical for all setups ($-0.07\log(Q^2)$), just the added constant lowered as the saturation scale Q_{s0}^2 increased (from 0.7 to 0.45 GeV²). This effect has not yet been reported by other groups and its origin needs further explanation.

The quality of these fits was also tested by determining the value of χ^2 . Its dependence on Q^2 was studied for various values of the re-scaling parameter. The lower values of Q_{s0}^2 exhibited worse χ^2 behavior in the regions with lower Q^2 than the fits obtained with higher Q_{s0}^2 . Its values reached up to $\chi^2 = 3$ in the region $Q^2 \sim (1, 10)$ for $Q_{s0}^2 = 0.04$ GeV². The regions higher than $Q^2 = 30$ showed high values of χ^2 for all sets of re-scaling parameters, which might be caused by the fact that at these values of Q^2 , the ratio F_2^{Data}/F_2^{Theory} has a non-trivial dependence on rapidity and that it cannot be fitted with a constant. This can mean that in this approach, there are still some softly contributing effects that have not yet been accounted for by the theory.

For $Q_{s0}^2 = 0.04$ GeV², the value of χ^2 reached the values of 7 at the highest at $Q^2 \sim 50$ GeV². As the re-scaling parameter increases, the value of χ^2 in this region further increases up to the maximal value of 14 when Q_{s0}^2 is set as 0.14 GeV². The values of χ^2 reach high values towards higher Q^2 , even though the growing trend of the ratio with respect to rapidity is slow, partly because the errorbars of the measured values decrease towards higher values of Q^2 . In the intermediate values of Q^2 , the values of χ^2 decrease with the increase of Q_{s0}^2 at first, but as we approach higher and higher values of Q_{s0}^2 its values are also distorted, so the optimal choice of the re-scaling parameter indeed proved to be $Q_{s0}^2 = 0.07$ GeV².

We used the obtained scaled initial condition to predict the values of the structure function $F_2(Q^2, Y)$ in regions that were not yet measured and where it differs from the solutions obtained with the MV initial condition. This prediction can then be used to determine the validity of this approach to the dipole model and rcBK equation in particular when new measurements (possibly at the LHC) are carried out.

The b-dependent BK equation and its solutions were also studied. We were able to

implement this approach with the use of Runge-Kutta method (the verification of validity of this approach is shown in the appendix) for the evolution in rapidity and Simpson's rule for integration over all intervals. We were able to transform the usual quark-vector shape of the b -dependent equation into the familiar dipole distance-vector shape that we used previously in the non b -dependent section. The solution in this approach then differs dramatically from the one obtained with b -independent equation. Unlike the b -independent equation, it suppresses the scattering amplitude in the regions of high dipole distance in the first units of rapidity, which corresponds to the situation when the dipole is too large with respect to the hadron to interact with it at all. This decrease is then eventually stopped and reversed as we approach higher values of Y and more and more partons emerge. These solutions were then integrated over the impact parameter b for various values of Y and their shape was shown in previous sections.

The combined advantages of the Runge-Kutta method for the impact parameter dependent rcBK equation (summed up in appendices A and B) as well as the properties of the integral over the angle θ_{rb} and the optimal setup of the computation that was adapted from the b -independent case result in a major decrease in the running time. It was shown that we can obtain the scattering amplitude for all dipole vector and impact parameter setups in about 10 hours on a regular personal computer up to the rapidity of $Y = 10$. This scattering amplitude then gives us the information about the strong interaction processes within the collision and can be recomputed into observable values such as structure function or reduced cross section which can tell us more about the physical nature of QCD systems.

To conclude, in this thesis we managed to explain the concepts of parton saturation (Section 1.1.2), Color Glass Condensate 1.3 and Color dipole model 1.1.3. We numerically solved the rcBK evolution equation with NLO kernel (4.2 and 4.4). We found the dependence of its solution on parameters of the numerical computation and on the considered initial condition (4.1 and 4.3). A prediction of the structure function in DIS was obtained with the use of rcBK equation (4.2 and 4.3). These were then compared with the data from HERA 4.2, and the error of the predicted structure function arising from the numerical computation was analyzed 4.1. All items that were enlisted in the Diploma thesis assignment were therefore successfully fulfilled.

Appendix A

Runge-Kutta method for the impact parameter dependent rcBK equation derivation

For the derivation and verification of the validity of the numerical approach in this work, we will use the notation

$$\frac{\partial N(Y, r, \vec{b})}{\partial Y} = f(Y, \vec{r}, \vec{b}, N(Y, \vec{r}, \vec{b})). \quad (4.8)$$

Also, since $f(Y, \vec{r}, \vec{b}, N(Y, \vec{r}, \vec{b}))$ has a non-zero partial derivative only for derivative with respect to $N(Y, r, \vec{b})$, we will denote it $f(N(Y))$ and $N(Y, r, \vec{b})$ will be denoted as $N(Y)$. For brevity we substitute $\frac{\partial f(N(Y))}{\partial N(Y)}$ for \wp . In further computations, we will restrict ourselves solely to first derivatives of $f(N(Y))$.

$$N(Y+h, r, \vec{b}) = N(Y) + hf(N(Y)) + \frac{h^2}{2} \frac{df(N(Y))}{dY} + \frac{h^3}{6} \frac{d^2 f(N(Y))}{dY^2} + \frac{h^4}{24} \frac{d^3 f(N(Y))}{dY^3} \quad (4.9)$$

This then reduces to

$$N(Y) + hf(N(Y)) + \frac{h^2}{2} \wp f(N(Y)) + \frac{h^3}{6} (\wp)^2 f(N(Y)) + \frac{h^4}{24} (\wp)^3 f(N(Y)) \quad (4.10)$$

and then

$$\begin{aligned} N(Y) + \frac{hf(N(Y))}{6} + \frac{h}{3} \left(f(N(Y)) + \frac{h}{2} \wp f(N(Y)) \right) + \frac{hf(N(Y))}{2} + \frac{h^2}{3} \wp f(N(Y)) \\ + \frac{h^3}{6} (\wp)^2 f(N(Y)) + \frac{h^4}{24} (\wp)^3 f(N(Y)) \end{aligned} \quad (4.11)$$

and this we can turn into

$$\begin{aligned}
N(Y) + \frac{hf(N(Y))}{6} + \frac{h}{3}(f(N(Y)) + \frac{h}{3}\left(f(N(Y)) + \frac{h}{2}\wp\left(f(N(Y)) + \frac{h}{2}\wp f(N(Y))\right)\right)) \\
+ \frac{h}{6}\left(f(N(Y)) + h\wp\left(f(N(Y)) + \frac{h}{2}\wp\left(f(N(Y)) + \frac{h}{2}\wp f(N(Y))\right)\right)\right)
\end{aligned} \tag{4.12}$$

by substituting the terms we then get

$$N(Y) + \frac{h}{6}k_1 + \frac{h}{3}k_2 + \frac{h}{3}k_3 + \frac{h}{6}k_4 \tag{4.13}$$

where

$$\begin{aligned}
N(Y + h) &= N(Y) + \frac{1}{6}h(k_1 + 2k_2 + 2k_3 + k_4) \\
k_1 &= f(N(Y)) \\
k_2 &= f(N(Y) + \frac{1}{2}hk_1) \\
k_3 &= f(N(Y) + \frac{1}{2}hk_2) \\
k_4 &= f(N(Y) + hk_3)
\end{aligned} \tag{4.14}$$

Appendix B

Simplified Runge Kutta method for the BK equation

If we apply the Runge-Kutta method of fourth order to the Balitsky-Kochegov equation, the general expression

$$\begin{aligned}
 N(Y + h) &= N(Y) + \frac{1}{6}h(k_1 + 2k_2 + 2k_3 + k_4) \\
 k_1 &= f(N(Y)) \\
 k_2 &= f(N(Y) + \frac{1}{2}hk_1) \\
 k_3 &= f(N(Y) + \frac{1}{2}hk_2) \\
 k_4 &= f(N(Y) + hk_3)
 \end{aligned} \tag{4.15}$$

gets simplified. If we denote

$$\begin{aligned}
 Kernel &= \int d\vec{r}_1 K^{run}(r_1, r_2, r) \\
 Split &= \int d\vec{r}_1 K^{run}(r_1, r_2, r)(N(Y, r_1) + N(Y, r_2)) \\
 Recomb &= \int d\vec{r}_1 K^{run}(r_1, r_2, r)(N(Y, r_1)N(Y, r_2))
 \end{aligned} \tag{4.16}$$

and

$$f(N(Y, r)) = \int d\vec{r}_1 K^{run}(r, r_1, r_2)(N(r_1, x) + N(r_2, x) - N(r, x) - N(r_1, x)N(r_2, x)) \tag{4.17}$$

then we can express the Runge Kutta coefficients as

$$k_1 = f(N(Y)) \tag{4.18}$$

$$\begin{aligned}
k_2 &= f(N(Y) + \frac{1}{2}hk_1) = \int dr_1^{\vec{r}} K^{run}(r, r_1, r_2)(N(r_1, x) + N(r_2, x) - \\
&N(r, x) + \frac{1}{2}hk_1 - (N(r_1, x) + \frac{1}{2}hk_1)(N(r_2, x) + \frac{1}{2}hk_1)) \quad (4.19) \\
&= k_1 + \frac{1}{2}hk_1 Kernel - \frac{1}{2}hk_1 Split - \frac{1}{4}h^2k_1^2 Kernel
\end{aligned}$$

$$k_3 = f(N(Y) + \frac{1}{2}hk_2) = k_1 + \frac{1}{2}hk_2 Kernel - \frac{1}{2}hk_2 Split - \frac{1}{4}h^2k_2^2 Kernel \quad (4.20)$$

$$k_4 = f(N(Y) + hk_3) = k_1 + \frac{1}{2}hk_3 Kernel - \frac{1}{2}hk_3 Split - \frac{1}{4}h^2k_3^2 Kernel \quad (4.21)$$

Which allows us to speed up the whole method since after the initial computation of *Kernel*, *Split* and $f(N(Y))$, there is no need to integrate the whole function again for obtaining the Runge-Kutta coefficients of higher order.

Bibliography

- [1] V. S. Fadin, E. A. Kuraev, and L. N. Lipatov, “On the Pommeranchuk Singularity in Asymptotically Free Theories,” *Phys. Lett.*, vol. B60, pp. 50–52, 1975.
- [2] L. N. Lipatov, “Reggeization of the Vector Meson and the Vacuum Singularity in Nonabelian Gauge Theories,” *Sov. J. Nucl. Phys.*, vol. 23, pp. 338–345, 1976, [Yad. Fiz.23,642(1976)].
- [3] E. A. Kuraev, L. N. Lipatov, and V. S. Fadin, “Multi - Reggeon Processes in the Yang-Mills Theory,” *Sov. Phys. JETP*, vol. 44, pp. 443–450, 1976, [Zh. Eksp. Teor. Fiz.71,840(1976)].
- [4] E. Kuraev, L. Lipatov, and V. S. Fadin, “The Pommeranchuk Singularity in Non-abelian Gauge Theories,” *Sov.Phys.JETP*, vol. 45, pp. 199–204, 1977.
- [5] I. Balitsky and L. Lipatov, “The Pommeranchuk Singularity in Quantum Chromodynamics,” *Sov.J.Nucl.Phys.*, vol. 28, pp. 822–829, 1978.
- [6] I. Balitsky, “Operator expansion for high-energy scattering,” *Nucl. Phys.*, vol. B463, pp. 99–160, 1996.
- [7] —, “Factorization for high-energy scattering,” *Phys. Rev. Lett.*, vol. 81, pp. 2024–2027, 1998.
- [8] —, “Factorization and high-energy effective action,” *Phys. Rev.*, vol. D60, p. 014020, 1999.
- [9] —, “Effective field theory for the small x evolution,” *Phys. Lett.*, vol. B518, pp. 235–242, 2001.
- [10] Y. V. Kovchegov, “Small x F(2) structure function of a nucleus including multiple pomeron exchanges,” *Phys. Rev.*, vol. D60, p. 034008, 1999.
- [11] V. N. Gribov and L. N. Lipatov, “e+ e- pair annihilation and deep inelastic e p scattering in perturbation theory,” *Sov. J. Nucl. Phys.*, vol. 15, pp. 675–684, 1972, [Yad. Fiz.15,1218(1972)].
- [12] —, “Deep inelastic e p scattering in perturbation theory,” *Sov. J. Nucl. Phys.*, vol. 15, pp. 438–450, 1972, [Yad. Fiz.15,781(1972)].
- [13] L. N. Lipatov, “The parton model and perturbation theory,” *Sov. J. Nucl. Phys.*, vol. 20, pp. 94–102, 1975, [Yad. Fiz.20,181(1974)].

- [14] Y. L. Dokshitzer, “Calculation of the Structure Functions for Deep Inelastic Scattering and $e^+ e^-$ Annihilation by Perturbation Theory in Quantum Chromodynamics.” *Sov. Phys. JETP*, vol. 46, pp. 641–653, 1977, [Zh. Eksp. Teor. Fiz.73,1216(1977)].
- [15] G. Altarelli and G. Parisi, “Asymptotic Freedom in Parton Language,” *Nucl. Phys.*, vol. B126, pp. 298–318, 1977.
- [16] D. Strozik-Kotlorz, S. V. Mikhailov, and O. V. Teryaev, “Generalized DGLAP evolution,” *J. Phys. Conf. Ser.*, vol. 678, no. 1, p. 012017, 2016.
- [17] Z. Nagy and D. E. Soper, “Final state dipole showers and the DGLAP equation,” *JHEP*, vol. 05, p. 088, 2009.
- [18] D. Toton, “Gluon distributions from Oliveira-Martin-Ryskin combined BFKL+DGLAP evolution equations,” *Phys. Rev.*, vol. D91, no. 5, p. 054003, 2015.
- [19] J. L. Albacete and Y. V. Kovchegov, “Solving high energy evolution equation including running coupling corrections,” *Phys. Rev.*, vol. D75, p. 125021, 2007.
- [20] J. L. Albacete, N. Armesto, J. G. Milhano, and C. A. Salgado, “Non-linear QCD meets data: A Global analysis of lepton-proton scattering with running coupling BK evolution,” *Phys. Rev.*, vol. D80, p. 034031, 2009.
- [21] J. L. Albacete, N. Armesto, J. G. Milhano, P. Quiroga-Arias, and C. A. Salgado, “AAMQS: A non-linear QCD analysis of new HERA data at small-x including heavy quarks,” *Eur. Phys. J.*, vol. C71, p. 1705, 2011.
- [22] J. Cepila and J. G. Contreras, “Rapidity dependence of saturation in inclusive HERA data with the rcBK equation,” 2015.
- [23] M. Matas, J. Cepila, and J. G. Contreras, “Numerical precision of the solution to the running-coupling Balitsky-Kovchegov equation,” *EPJ Web of Conferences*, vol. 112, p. 02008, 2016.
- [24] A. M. Stasto, K. J. Golec-Biernat, and J. Kwiecinski, “Geometric scaling for the total $\gamma^* p$ cross-section in the low x region,” *Phys. Rev. Lett.*, vol. 86, pp. 596–599, 2001.
- [25] M. Praszalowicz and T. Stebel, “Quantitative Study of Different Forms of Geometrical Scaling in Deep Inelastic Scattering at HERA,” *JHEP*, vol. 04, p. 169, 2013.
- [26] G. Soyez, C. Marquet, and R. B. Peschanski, “Geometric scaling in high-energy QCD at nonzero momentum transfer,” in *Proceedings, 40th Rencontres de Moriond on QCD and High Energy Hadronic Interactions: La Thuile, Aosta Valley, Italy, March 12-19, 2005*, 2005, pp. 371–374. [Online]. Available: https://inspirehep.net/record/680565/files/arXiv:hep-ph_0504117.pdf

- [27] A. Kormilitzin, E. Levin, and S. Tapia, “Geometric scaling behavior of the scattering amplitude for DIS with nuclei,” *Nucl. Phys.*, vol. A872, pp. 245–264, 2011.
- [28] K. J. Golec-Biernat and A. M. Stasto, “On solutions of the Balitsky-Kovchegov equation with impact parameter,” *Nucl. Phys.*, vol. B668, pp. 345–363, 2003.
- [29] J. Berger and A. M. Stasto, “Small x nonlinear evolution with impact parameter and the structure function data,” *Phys. Rev.*, vol. D84, p. 094022, 2011.
- [30] J. Berger and A. Stasto, “Numerical solution of the nonlinear evolution equation at small x with impact parameter and beyond the LL approximation,” *Phys. Rev.*, vol. D83, p. 034015, 2011.
- [31] M. H., “Balitsky-Kovchegov equation,” *University of Jyvaskyla*, pp. 1–69, 2011.
- [32] L. McLerran, “The CGC and the Glasma: Two Lectures at the Yukawa Institute,” *Prog. Theor. Phys. Suppl.*, vol. 187, pp. 17–30, 2011.
- [33] M. Kuhlen, “QCD at HERA: The hadronic final state in deep inelastic scattering,” *Springer Tracts Mod. Phys.*, vol. 150, pp. 1–172, 1999.
- [34] V. Barone and E. Predazzi, *High-Energy Particle Diffraction*, ser. Texts and Monographs in Physics. Berlin Heidelberg: Springer-Verlag, 2002, vol. v.565. [Online]. Available: <http://www-spires.fnal.gov/spires/find/books/www?cl=QC794.6.C6B37::2002>
- [35] N. N. Nikolaev and B. Zakharov, “Color transparency and scaling properties of nuclear shadowing in deep inelastic scattering,” *Z. Phys.*, vol. C49, pp. 607–618, 1991.
- [36] ———, “Pomeron structure function and diffraction dissociation of virtual photons in perturbative QCD,” *Z. Phys.*, vol. C53, pp. 331–346, 1992.
- [37] A. H. Mueller, “Small x Behavior and Parton Saturation: A QCD Model,” *Nucl. Phys.*, vol. B335, p. 115, 1990.
- [38] E. Iancu, K. Itakura, and S. Munier, “Saturation and BFKL dynamics in the HERA data at small x,” *Phys. Lett.*, vol. B590, pp. 199–208, 2004.
- [39] E. Gotsman, E. Levin, M. Lublinsky, and U. Maor, “Towards a new global QCD analysis: Low x DIS data from nonlinear evolution,” *Eur. Phys. J.*, vol. C27, pp. 411–425, 2003.
- [40] H. Kowalski and D. Teaney, “An Impact parameter dipole saturation model,” *Phys. Rev.*, vol. D68, p. 114005, 2003.
- [41] J. L. Albacete and C. Marquet, “Gluon saturation and initial conditions for relativistic heavy ion collisions,” *Prog. Part. Nucl. Phys.*, vol. 76, pp. 1–42, 2014.

- [42] K. J. Golec-Biernat and M. Wusthoff, “Saturation effects in deep inelastic scattering at low Q^2 and its implications on diffraction,” *Phys. Rev.*, vol. D59, p. 014017, 1998.
- [43] K. Nakamura *et al.*, “Review of particle physics,” *J. Phys.*, vol. G37, p. 075021, 2010.
- [44] P. Quiroga-Arias, J. L. Albacete, N. Armesto, J. G. Milhano, and C. A. Salgado, “AAMQS: a non-linear QCD description of new HERA data at small- x ,” *J. Phys.*, vol. G38, p. 124124, 2011.
- [45] O. E.G., “Balitsky Kovchegov evolution equation,” *Universidade Federal do Rio Grande do Sul.*, pp. 1–69,[online] <http://www.if.ufrgs.br/gfpae/sem/2008/BK.pdf>, 2009.
- [46] J. Zhou, “The evolution of the small x gluon TMD,” 2016.
- [47] S. Fleming, “Glauber Gluons in SCET and the BFKL Equation,” *PoS*, vol. QCDEV2015, p. 047, 2016.
- [48] V. T. Kim, “Search for BFKL-evolution manifestations at high energies,” *Int. J. Mod. Phys. Conf. Ser.*, vol. 39, p. 1560106, 2015.
- [49] L. McLerran and V. V. Skokov, “The MV Model of the Color Glass Condensate for a Finite Number of Sources Including Coulomb Interactions,” 2016.
- [50] J. Jalilian-Marian, “High energy nuclear collisions from QCD at small Bjorken x ,” *Nucl. Part. Phys. Proc.*, vol. 270-272, pp. 46–49, 2016.
- [51] E. Gotsman, E. Levin, U. Maor, and S. Tapia, “CGC/saturation approach for high energy soft interactions: v_2 in proton-proton collisions,” *Phys. Rev.*, vol. D93, p. 074029, 2016.
- [52] E. Gotsman, E. Levin, and U. Maor, “CGC/saturation approach for soft interactions at high energy: survival probability of central exclusive production,” *Eur. Phys. J.*, vol. C76, no. 4, p. 177, 2016.
- [53] J. Jalilian-Marian, A. Kovner, A. Leonidov, and H. Weigert, “The Wilson renormalization group for low x physics: Towards the high density regime,” *Phys. Rev.*, vol. D59, p. 014014, 1998.
- [54] J. Jalilian-Marian, A. Kovner, and H. Weigert, “The Wilson renormalization group for low x physics: Gluon evolution at finite parton density,” *Phys. Rev.*, vol. D59, p. 014015, 1998.
- [55] H. Weigert, “Unitarity at small Bjorken x ,” *Nucl. Phys.*, vol. A703, pp. 823–860, 2002.
- [56] E. Iancu, A. Leonidov, and L. D. McLerran, “Nonlinear gluon evolution in the color glass condensate. 1.” *Nucl. Phys.*, vol. A692, pp. 583–645, 2001.

- [57] —, “The Renormalization group equation for the color glass condensate,” *Phys. Lett.*, vol. B510, pp. 133–144, 2001.
- [58] E. Ferreiro, E. Iancu, A. Leonidov, and L. McLerran, “Nonlinear gluon evolution in the color glass condensate. 2.” *Nucl. Phys.*, vol. A703, pp. 489–538, 2002.
- [59] H. Weigert, T. Lappi, A. Ramnath, and K. Rummukainen, “JIMWLK and beyond: From concepts to observables,” *EPJ Web Conf.*, vol. 112, p. 02016, 2016.
- [60] Y. V. Kovchegov, “Brief Review of Saturation Physics,” *Acta Phys. Polon.*, vol. B45, no. 12, pp. 2241–2256, 2014.
- [61] E. Iancu and D. N. Triantafyllopoulos, “JIMWLK evolution in the Gaussian approximation,” *JHEP*, vol. 04, p. 025, 2012.
- [62] Y. V. Kovchegov, “Unitarization of the BFKL pomeron on a nucleus,” *Phys. Rev.*, vol. D61, p. 074018, 2000.
- [63] D. Boer, A. Utermann, and E. Wessels, “Compatibility of phenomenological dipole cross sections with the Balitsky-Kovchegov equation,” *Phys. Rev.*, vol. D75, p. 094022, 2007.
- [64] I. Balitsky, “Quark contribution to the small-x evolution of color dipole,” *Phys. Rev.*, vol. D75, p. 014001, 2007.
- [65] C. Marquet and G. Soyez, “The Balitsky-Kovchegov equation in full momentum space,” *Nucl. Phys.*, vol. A760, pp. 208–222, 2005.
- [66] Y. V. Kovchegov and H. Weigert, “Triumvirate of Running Couplings in Small-x Evolution,” *Nucl. Phys.*, vol. A784, pp. 188–226, 2007.
- [67] K. A. Olive *et al.*, “Review of Particle Physics,” *Chin. Phys.*, vol. C38, p. 090001, 2014.
- [68] L. D. McLerran and R. Venugopalan, “Boost covariant gluon distributions in large nuclei,” *Phys. Lett.*, vol. B424, pp. 15–24, 1998.
- [69] E. Vitasek, “Numerické metody,” *SNTL*, vol. 428, pp. 1–257, 1987.
- [70] F. D. Aaron *et al.*, “Combined Measurement and QCD Analysis of the Inclusive e^+p Scattering Cross Sections at HERA,” *JHEP*, vol. 01, p. 109, 2010.